

Rochester Institute of Technology

RIT Digital Institutional Repository

Theses

1-2023

A Three-Dimensional CFD Analysis for the Hydrodynamics of the Direct Contact Heat Transfer in the Oxygen Production Slurry Bubble Column Reactor of the CU-CL Cycle of Hydrogen Production

Nibras Ibrahim Nassar
nin8507@rit.edu

Follow this and additional works at: <https://repository.rit.edu/theses>

Recommended Citation

Nassar, Nibras Ibrahim, "A Three-Dimensional CFD Analysis for the Hydrodynamics of the Direct Contact Heat Transfer in the Oxygen Production Slurry Bubble Column Reactor of the CU-CL Cycle of Hydrogen Production" (2023). Thesis. Rochester Institute of Technology. Accessed from

This Thesis is brought to you for free and open access by the RIT Libraries. For more information, please contact repository@rit.edu.

Rochester Institute of Technology

A THREE-DIMENSIONAL CFD ANALYSES FOR THE
HYDRODYNAMICS OF THE DIRECT CONTACT HEAT
TRANSFER IN THE OXYGEN PRODUCTION SLURRY BUBBLE
COLUMN REACTOR OF THE CU-CL CYCLE OF HYDROGEN
PRODUCTION

By

Nibras Ibrahim Nassar

A Thesis Submitted
In
Partial Fulfillment of the
Requirements for the Degree of
Master of Science
In
Mechanical Engineering
Supervised by

Dr. Mohammed W. Abdulrahman

Department of Mechanical Engineering
Kate Gleason College of Engineering
Rochester Institute of Technology
Dubai, UAE

January 2023

The thesis “A Three-Dimensional CFD Analyses for the Hydrodynamics of the Direct Contact Heat Transfer in the Oxygen Production Slurry Bubble Column Reactor of the Cu-Cl Cycle of Hydrogen Production” by Nibras Ibrahim Nassar has been examined and approved by the following Examination Committee:

Dr. Ghalib Kahwaji

Professor and Chair

(Thesis Committee Chair)

Dept. of Mechanical & Industrial Engineering

Dr. Mohamed Samaha

Associate Professor

(Committee Member)

Dept. of Mechanical Engineering

Dr. Mohammed Abdulrahman

Assistant Professor

(Committee Member)

Dept. of Mechanical Engineering

Acknowledgement

First and foremost, I give thanks to Allah for giving me the opportunity to successfully embark on this journey. I would like to express my deepest appreciation to my advisor Dr. Mohammed Abdulrahman. I am extremely grateful to Dr. Abdulrahman for all his guidance, feedback, and patience.

I would also like to thank the committee members Dr. Ghalib Kahwaji for raising some important points that needed to be addressed within the thesis and Dr. Mohamed Samaha for his support with the CFD software.

Furthermore, I would like to give thanks to my parents Dr. Mona Abu Ghazalah and Dr. Ibrahim Nassar for instilling in me the drive and ambition to reach for excellence and for their constant support. Last but not least I would like to thank my sisters for always encouraging me and supporting me.

Abstract

Hydrogen is becoming an increasingly attractive alternative fuel. As such it is important to investigate different methods of hydrogen production. This thesis examines the thermochemical process of splitting water using the three stage CuCl Cycle. In particular it examines the hydrodynamics of a direct heat contact, CuCl's oxygen reactor for a two-phase system, using a three dimensional, Eulerian-Eulerian Computational Fluid Dynamics (CFD) model. The model was first verified using experimental results and compared to a two-dimensional CFD model by examining the gas holdup (α_g) using a Helium-Water-Alumina system for different reactor heights (H) (45,55,65 cm), different superficial gas velocities (U_{gs}) (0.05-0.15 m/s), and different solid particle concentrations (C_s) (0%, 5%, 10%). The three-dimensional He-H₂O-Al₂O₃ system was able to accurately model the trends of the α_g while changing the reactor (H), U_{gs} , and C_s with a maximum percent error of 8.37%. Additionally, the model was more accurate at lower C_s . The three-dimensional model was more accurate and somewhat over predicted the α_g in comparison to the two-dimensional model. The model was then used to predict the hydrodynamic trends for the O₂- CuCl system when changing the reactor H and U_{gs} . The model under predicted the hydrodynamic trends compared to the helium-water system and was found to be less accurate with a maximum percent error of 48.6%. In both systems it was concluded that α_g increases when increasing the U_{gs} . A 95% increase in the α_g was observed in the He-H₂O-Al₂O₃ system for $C_s=0\%$ and $H=45\text{cm}$ when increasing the U_{gs} from 0.05m/s to 0.15m/s. Furthermore, the α_g increased by decreasing the H as an 11% decrease in α_g was observed for $C_s=0\%$ at a U_{gs} of 0.05m/s when increasing the H from 45cm to 65cm. Lastly, increasing the C_s decreased the α_g by 6% for a $H=45\text{cm}$ and U_{gs} of 0.05m/s when increasing the C_s from 0% to 10%.

Table of Contents

Acknowledgement.....	iii
Abstract.....	iv
Table of Contents.....	v
List of Tables.....	viii
List of Figures.....	ix
List of Symbols.....	xiv
Chapter-1	1
1.1 Oxygen Reactor	4
1.2 Slurry Bubble Column Reactors (SBCR).....	5
1.2.1. Gas holdup	6
1.2.2. Heat Transfer	7
1.2.3. CFD.....	7
1.3 Motivation	8
1.4 Objective.....	9
Chapter-2	10
2.1. The CuCl Cycle and Oxygen Reactor	10
2.2. Bubble Column Reactors.....	12
2.2.1. Hydrodynamic Investigations	14
2.2.2. Effects of Solid Particles.....	22
2.2.3. Heat Transfer	27

2.2.4. Process Intensification	31
2.3. Summary of the Literature Survey	32
Chapter-3	34
CFD Simulation Model	34
3.1 Slurry Bubble Column Reactor Geometry	34
3.1.2 Operating Conditions	37
3.2 Methods of Multiphase CFD	37
3.2.1. Euler – Lagrange Method	37
3.2.2. Euler-Euler Method	38
3.2.3. Volume of Fluid Model (VOF).....	39
3.2.4 The Mixture Model	39
3.2.5 The Eulerian Model	40
3.3. Eulerian Model Theory.....	42
3.4 Turbulence Model	46
3.5 Model Summary	49
3.6 Material Properties	49
3.6.1 Gas Phase Properties.....	50
3.6.2 Liquid Phase Properties	51
3.6.3 Solid Phase Properties.....	51
3.6.4 Slurry Phase Properties	53
3.6.5 Material Property Summary.....	54
3.7 CFD Model Validation	56

3.7.1 ANSYS Fluent Setup	56
3.7.2 Comparison of the Gas Holdup of the Helium-Water-Alumina 3D CFD Simulations with 2D CFD Simulations and Experimental Data.....	57
Results and Discussion	62
4.1. Introduction	62
4.2. Gas Holdup Results for the Helium-Water-Alumina System	62
4.2.1. Effects of Superficial Gas Velocity (U_{gs}) on Gas Holdup (α_g).....	62
4.2.2 Effects of Static Liquid Height (H) on Gas Holdup (α_g)	71
4.2.3 Effects of Solid Particle Concentration (C_s) on Gas Holdup (α_g)	79
4.3 Gas Holdup Results of the 3D-CFD Simulations of the Oxygen-Cupreous Chloride System.....	87
4.3.1 Effects of Superficial Gas Velocity on Gas Holdup	87
4.3.2. Effects of Static Liquid Height on Gas Holdup	92
4.3.3. Comparison of the 3D Water -Helium CFD system and the 3D Couperus Chloride-Oxygen CFD system.....	97
Chapter 5.....	100
Conclusion and Future Works	100
5.1 Conclusion.....	100
5.2 Recommendations for Future Research.....	102
References	104

List of Tables

Table 2. 1 Bubble Column Flow Model Summary [15].	13
Table 2. 2 Validation Studies summary used by Ertekin et al. [17].	16
Table 2. 3 Pneumatically agitated slurry reactor investigated numerically [34].	32
Table 3. 1 Comparison of the Euler-Lagrange Method and the Euler-Euler Method data collected from [35].	38
Table 3. 2 Identification of the flow type that should be used for each model [36].	40
Table 3. 3 Physical properties of gas material [38],[39],[40].	50
Table 3. 4 Physical properties of liquid material [41],[38],[39],[40].	51
Table 3. 5 Solid Alumina properties bases on Auerkari [42] formulas.	52
Table 3. 6 Material properties for the Water-Helium- Alumina systems for concentrations Cs=0%, Cs=5% and Cs=10%.	55
Table 3. 7 Material properties for the Cuprous-Chloride systems for concentrations Cs=0%.	55

List of Figures

Figure.1.1 CuCl Cycle of three stages [4]	3
Figure.1. 2 Diagram of a slurry bubble column schematic [6].	5
Figure. 2. 1 Experimental bubble column reactor used by Abdulrahman [4].	18
Figure. 2. 2 Slurry bubble columns used by Li et al. [22].	20
Figure. 2. 3 Bubble column reactors investigated by Li and Zhong [24]. 1) Gandhi et al. 2) Rampure et al. 3) Li and Zhong.	22
Figure. 2. 4 Bubble column reactor setups tested for the PBDS model [26].	23
Figure. 2. 5 Experimental bubble column reactor investigated by Chen and Brooks [27].	26
Figure. 2. 6 Bubble slurry column reactor and gas distributor used by Li et al. [15].	31
Figure. 3. 1 Abdulrahman [4] (a) SBCR design and (b) Sparger design	35
Figure. 3.2 Progression of simplifying the reactor design (a) most complex, (b) more simplified (c) most simple, final design.	36
Figure. 3.3 Final SBCR geometry used for simulations.	36
Figure. 3.4 SBCR hexahedron mesh.	57
Figure. 3.5 Comparison of Average Gas Holdup Versus Superficial Gas Velocity between 2D, 3D and Experimental Results at a Solid Particle Concentration of 0% for (a) H=45 (b) H=55 (c) H=65cm.	59
Figure. 3.6 Comparison of Average Gas Holdup Versus Superficial Gas Velocity between 2D, 3D and Experimental Results at a Solid Particle Concentration of 10% for (a) H=45 (b) H=55 (c) H=65cm.	59
Figure. 3.7 Comparison Between 3D CFD and Experimental Data for the Helium-Water-Alumina system, Gas Holdup Versus the Solid Particle Concentration at Different Static Liquid Heights (a) H=45 (b) H=55 (c) H=65cm.	60

Figure. 3. 8 Comparison Between 3D CFD and Experimental Gas Holdup Versus the Static Liquid Height at Different Superficial Velocities for (a) $C_s=0\%$, (b) $C_s=5\%$, (c) $C_s=10\%$.	61
Figure. 4. 1 Average Gas Holdup Versus Superficial Gas Velocity and Static Liquid Height of Helium-Water-Alumina at (a) $C_s=0\%$, (b) $C_s=5\%$, (c) $C_s=10\%$.	64
Fig. 4. 2 Average Gas Holdup Versus Superficial Gas Velocity and Solid Particle Concentration of Helium- Water-Alumina For (a) $H=45\text{cm}$, (b) $H=55$, (c) $H=65$.	65
Figure. 4. 3 Average Gas Holdup Versus Superficial Gas Velocity of Helium-Water-Alumina System at Different Heights for Different Solid Particle Concentrations (a) 0% , (b) 5% , (c) 10% .	66
Fig. 4. 4 Average Gas Holdup Versus Superficial Gas Velocity Helium-Water-Alumina System at Different Solid particle Concentrations for Different Static Liquid Heights (a) $H=45\text{cm}$, (b) $H=55\text{cm}$, (c) $H=65\text{cm}$.	66
Figure. 4. 5 Water- Helium-Alumina Gas Holdup Contours for $H=45\text{cm}$, $C_s=0\%$.	67
Figure. 4. 6 Water- Helium-Alumina Gas Holdup Contours for $H=65\text{cm}$, $C_s=0\%$.	68
Figure. 4. 7 Water- Helium-Alumina Gas Holdup Contours for $H=45\text{cm}$, $C_s=10\%$.	69
Figure. 4. 8 Water- Helium-Alumina Gas Holdup Contours for $H=65\text{cm}$, $C_s=10\%$.	70
Figure. 4. 9 Average Gas Holdup Versus Static Liquid Height and Superficial Gas Velocity of Helium-Water-Alumina at (a) $C_s=0\%$, (b) $C_s=5\%$, (c) $C_s=10\%$.	72
Figure. 4. 10 Average Gas Holdup Versus Static Liquid Height and Solid Particle Concentration of Helium-Water-Alumina at (a) $U_{gs}=0.05\text{m/s}$ (b) $U_{gs}=0.1\text{m/s}$ (c) $U_{gs}=0.15\text{m/s}$.	73
Figure. 4. 11 Average Gas holdup Versus Static Liquid Height of Helium-Water-Alumina system at Different Superficial Velocities for (a) $C_s =0\%$, (b) $C_s =5\%$, (c) $C_s =10\%$.	74

Figure. 4. 12 Average Gas holdup Versus Static Liquid Height of Helium-Water-Alumina system at Different Solid Particle Concentrations for (a) $U_{gs}=0.05$, (b) $U_{gs}=0.10$, (c) $U_{gs}=0.15$ m/s.	74
Figure. 4. 13 Water- Helium-Alumina Gas Holdup Contours for $U_{gs}=0.05$ m/s at $C_s=0\%$ for Different Static Liquid Heights.	75
Figure. 4. 14 Water- Helium-Alumina Gas Holdup Contours for $U_{gs}=0.15$ m/s at $C_s=0\%$ for Different Static Liquid Heights.	76
Figure. 4. 15 Water- Helium-Alumina Gas Holdup Contours for $U_{gs}=0.05$ m/s at $C_s=10\%$ for Different Static Liquid Heights.	77
Figure. 4. 16 Water- Helium-Alumina Gas Holdup Contours for $U_{gs}=0.15$ m/s at $C_s=10\%$ for Different Static Liquid Heights.	78
Figure. 4. 17 Average Gas Holdup Versus Solid Particle Concentration and Superficial Gas Velocity of Helium-Water-Alumina at (a) $H=45$ (b) $H=55$, (c) $H=65$ cm.	80
Figure. 4. 18 Average Gas Holdup Versus Solid Particle Concentration and Static Liquid Height of Helium-Water-Alumina at (a) $U_{gs}=0.05$ m/s (b) $U_{gs}=0.1$ m/s (c) $U_{gs}=0.15$ m/s.	81
Figure. 4. 19 Average Gas holdup Versus Solid Particle Concentration of Helium-Water-Alumina System at Different Superficial Velocities for (a) $H=45$ (b) $H=55$ (c) $H=65$ cm.	82
Figure. 4. 20 Average Gas holdup Versus Solid Particle Concentrations of Helium-Water-Alumina System at Different Static Liquid Heights for (a) $U_{gs}=0.05$, (b) $U_{gs} =0.10$, (c) $U_{gs} = 0.15$ m/s.	82
Figure. 4. 21 Water- Helium-Alumina Gas Holdup Contours for $U_{gs}=0.05$ m/s at $H=45$ cm for Different Solid Particle Concentrations.	83
Figure. 4. 22 Water- Helium-Alumina Gas Holdup Contours for $U_{gs}=0.15$ m/s at $H=45$ cm for Different Solid Particle Concentrations.	84

Figure. 4. 23 Water- Helium-Alumina Gas Holdup Contours for $U_{gs}=0.05\text{m/s}$ at $H=65\text{cm}$ for Different Solid Particle Concentrations.	85
Figure. 4. 24 Water- Helium-Alumina Gas Holdup Contours for $U_{gs}=0.15\text{m/s}$ at $H=65\text{cm}$ for Different Solid Particle Concentrations.	86
Figure. 4. 25 Average Gas Holdup Versus Superficial Gas Velocity Static Liquid Height of CuCl-O ₂ , $C_s=0\%$.	88
Figure. 4. 26 Average Gas Holdup Versus Superficial Gas Velocity of CuCl- O ₂ for $C_s=0\%$.	88
Figure. 4. 27 Oxygen-Cupreous Chloride Gas Holdup Contours for $H=45\text{cm}$, $C_s=0\%$.	89
Figure. 4. 28 Oxygen-Cupreous Chloride Gas Holdup Contours for $H=55\text{cm}$, $C_s=0\%$.	90
Figure. 4. 29 Oxygen-Cupreous Chloride Gas Holdup Contours for $H=65\text{cm}$, $C_s=0\%$.	91
Figure. 4. 30 Average Gas Holdup (α_g) Versus Superficial Gas Velocity Static Liquid Height of CuCl-O ₂ for $C_s=0\%$.	92
Figure. 4. 31 Average Gas Holdup Versus Static Liquid Height (H) of CuCl-O ₂ at Different Superficial Gas Velocities (U_{gs}) at $C_s=0\%$.	93
Figure. 4. 32 Oxygen-Cupreous Chloride Gas Holdup Contours for $U_{gs} =0.0283 \text{ m/s}$.	94
Figure. 4. 33 Oxygen-Cupreous Chloride Gas Holdup Contours for $U_{gs} =0.0567 \text{ m/s}$.	95
Figure. 4. 34 Oxygen-Cupreous Chloride Gas Holdup Contours for $U_{gs} =0.085 \text{ m/s}$.	96
Figure. 4. 35 Dimensionless groups of actual and experimental material percent error [4].	97
Figure. 4. 36 Comparison between the Water-Helium system and Cupreous Chloride-Oxygen superficial velocity and gas holdup with the calculated percent error.	98
Figure. 4. 37 Comparison between the effects of static liquid heights on gas holdup versus different superficial gas velocities (a) Water-Helium data, (b) Cupreous chloride-oxygen data.	99

Figure. 4. 38 Comparison of Average Gas Holdup Versus Static Liquid Height for (a) Water-Helium system $C_s=0\%$ (b) Cupreous Chloride-Oxygen system $C_s=0\%$. 99

List of Symbols

A_i	Interfacial area concentration
$C_{p,g}$	Specific heat gas
$C_{p,l}$	Specific heat, liquid
$C_{p,s}$	Specific heat of the solid phase
C_s	Volume fraction of solid particles
C_D	Drag coefficient
d_o	Inlet diameter
d_b	Bubble diameter
D_R	Reactor diameter
E	Empirical constant
g	Gravitational acceleration
H	Height
H_R	Reactor height
k	Von Karman constant
k_p	Turbulence kinetic energy at the near wall node P
k_g	Thermal conductivity, gas
k_l	Thermal conductivity, liquid
k_{sl}	Thermal conductivity, Slurry
M_i	Total interfacial forces between the phases
Nu_g	Nusselt number
P	Phase pressure
Pr	Prandtl number

$Q_{g,sl}$	Intensity of heat exchange between the gas and slurry phases
Re	Reynolds number
RNG	Renormalization group
T	Temperature
U^*	Dimensionless velocity
U_p	Mean velocity of the fluid near wall-node P
v	Velocity field
V_g	Volumes of gas
V_l	Volumes of liquid
V_s	Volumes of solid
V_t	Total volumes
U_{gs}	Superficial gas velocity
We_t	Webbers number
y^*	Dimensionless distance from the wall
y_p	Distance from point P to the wall
α_g	Gas holdup
α_l	Liquid holdup
α_s	Solid holdup
α_{sl}	Slurry holdup
μ_{eff}	Effective viscosity
μ_g	Dynamic viscosity gas
μ_l	Dynamic viscosity liquid
μ_{sl}	Dynamic viscosity, slurry

μ_r	Dimensionless relative dynamic viscosity
$\rho_{Al_2O_3}$	Density of alumina
ρ_g	Density, gas
ρ_l	Density, liquid
ρ_{sl}	Density, slurry
σ	Surface tension
$\bar{\tau} : \nabla V$	Viscous stress tensor contracted with the velocity gradient

List of Acronyms

ANL	Argonne National Laboratories
CFD	Computational Fluid Dynamics
EMMS	Energy minimization multiscale
PBM	Population balance model
PDBS	Particle dependent dual bubble size
RANS	Reynolds-averaged Navier-stokes
SBCR	Slurry bubble column reactor
VOF	Volume of fluid Model

Chapter-1

Introduction

The world heavily relies on fossil fuels to generate energy. Unfortunately, energy produced from fossil fuels leads to the release of harmful greenhouse gases which can degrade and pollute the environment. One solution which has the potential to generate energy as an alternative to fossil fuels is hydrogen. It is anticipated that hydrogen will be a major contributing component to the sustainable energy supply in the future [1] since the usage of hydrogen will minimize the pollution that contributes to climate change by lowering greenhouse gas emissions. Gasoline and diesel-fueled vehicles, for example, produce greenhouse gases that contribute to climate change, while fuel cell vehicles driven by pure hydrogen only release heat and water without the production of greenhouse gases. Hydrogen gas generation from a variety of fuel gases may create greenhouse gases, however the emissions are much lower than those typical produced by gasoline and diesel vehicles.

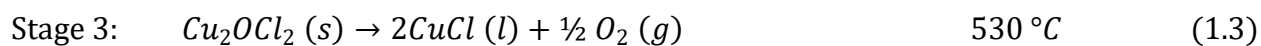
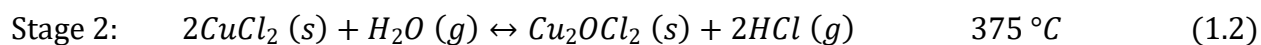
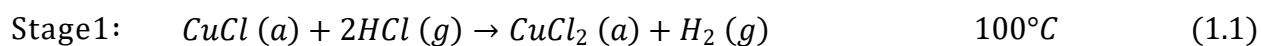
Hydrogen can be used for more than just fuel cells in the transport industry. Hydrogen is required in large amounts by a variety of industries including the petrochemical, agricultural, food processing, electronics, plastics, metallurgical, and aerospace industries. Given hydrogen's numerous uses it is anticipated that the global hydrogen consumption will increase in the near future.

Steam-methane reforming or partial oxidation of heavy hydrocarbons are the most commonly used methods to produce hydrogen on a global scale. Both of these methods release high quantities of carbon dioxide. These methods face substantial obstacles due to growing greenhouse gas emissions, dwindling gas sources, and escalating carbon capture. The hydrogen economy's primary

issue is sustainable hydrogen generation (without reliance on fossil fuels) in large volumes at lower prices than the current technologies' capabilities.

Thermochemical cycles are potential solutions that can be coupled with nuclear reactors to thermally breakdown water into oxygen and hydrogen through multistage processes. Using heat exchangers allows the transfer or recovery of heat from different endothermic and exothermic processes during the different reaction cycles. Argonne National Laboratories (ANL)

has recognized the copper-chlorine (CuCl) cycle as one of the most promising low temperature cycles [2],[3]. This CuCl cycle consists of three reactions as shown in Figure.1. 1, where two of which are thermal and one is electrochemical. This cycle requires lower temperatures which is one of the most significant benefits in comparison to many other cycles. Additionally, the cycle may be performed in a manner which requires little high-quality energy and solid exchanges. The CuCl cycle consists of three chemical stages presented below:



a, *s*, *l* and *g* stand for aqueous, solid, liquid and gas respectively [4].

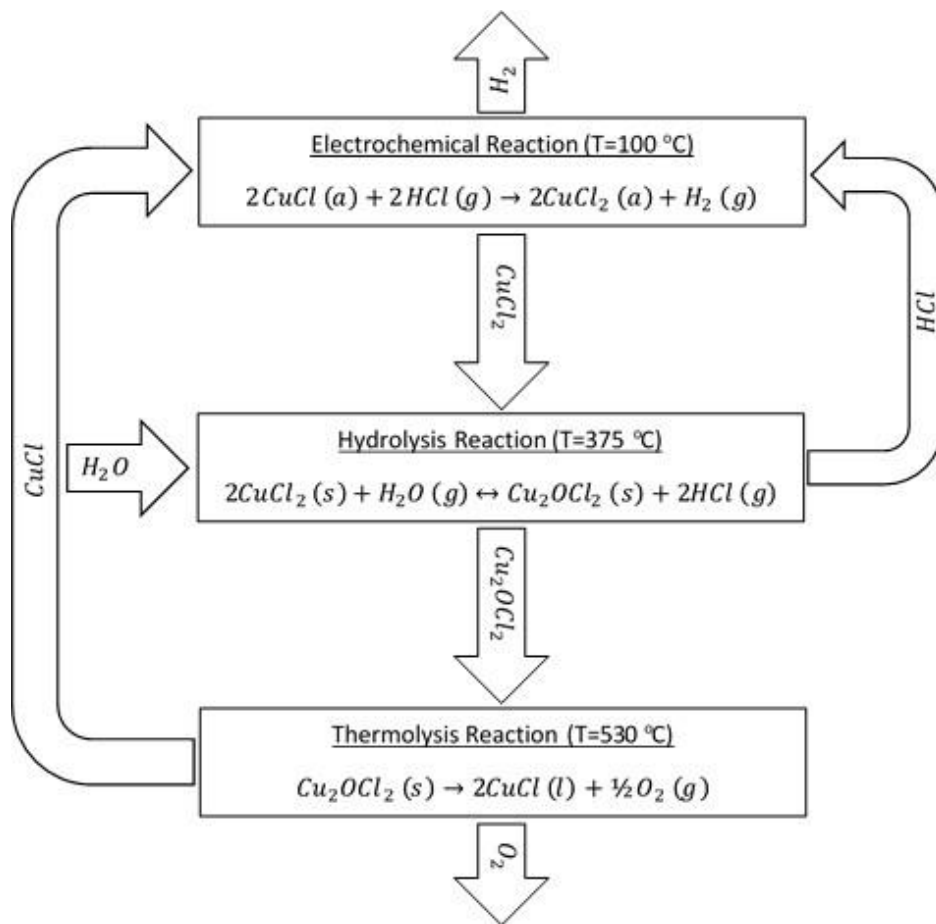


Figure.1.1 CuCl Cycle of three stages [4]

The CuCl cycle's oxygen generation stage (stage 3) involves the decomposition of an intermediate chemical, solid copper oxychloride (Cu_2OCl_2), into oxygen gas and molten cuprous chloride (CuCl). The oxygen generation reactor receives the solid input of anhydrous solid Cu_2OCl_2 from the CuCl_2 hydrolysis process (stage 2), which occurs at temperatures ranging between 350–450°C. The oxygen gas is produced in the oxygen reactor at temperatures ranging from 450 to 530°C.

The highest temperatures in the CuCl cycle occurs during the breakdown of Cu_2OCl_2 into oxygen and molten CuCl in the oxygen reactor. This reaction is an endothermic process that requires a reaction heat of 129.2 kJ/mol and a temperature of 530°C [5]. As a result, heat must be provided to increase and maintain the temperature of the reactor's mass. The total heat needed is the summation of the reaction heat and the heat necessary to elevate the reactant temperature from 375°C (the solid particle temperature after the hydrolysis reaction) to 530°C.

1.1 Oxygen Reactor

The oxygen reaction is a high temperature reaction that requires a source of high temperature heat. This heat may be generated using nuclear reactors or solar thermal energy which are non-polluting source of high-temperature heat. It has been found that the more practical and effective method of heating oxygen reactor is to heat the molten salt inside the oxygen reactor, which will transmit heat from the molten CuCl (l) to the solid Cu_2OCl_2 (reactant) particles within the reactor. Different methods of heat transfer have been investigated for the oxygen reactor [6-10]. It has been found that the best method of heat transfer that can be used for the oxygen reactor is the direct contact heat transfer from the oxygen gas to the molten CuCl [4,10]. In this method, some of the oxygen gas that is produced from the decomposition process in the oxygen reactor is heated to

530°C and reinjected to the oxygen reactor to transfer heat directly to the molten salt.

Direct heating means that there is a direct contact between the heating fluid and the heated medium. Heating the fluid directly has the benefit of being approximately 100% efficient. This is because there is no thermal lag in the process and all the heat can be transferred from the heating fluid to the heated medium. A Slurry Bubble Column Reactor (SBCR) may be used for direct heating, allowing the heating gas to be fed into the reactor from the base of the column by using a sparger.

1.2 Slurry Bubble Column Reactors (SBCR)

Slurry Bubble column reactors (Figure.1. 2) are multiphase vertical reactors that contain gas and slurry of liquid and fine particles where the gas is fed into the reactor by a sparger and bubbles are formed inside the slurry. The type of the reactor that can be used for the oxygen production process in the CuCl cycle is the slurry bubble column reactor.

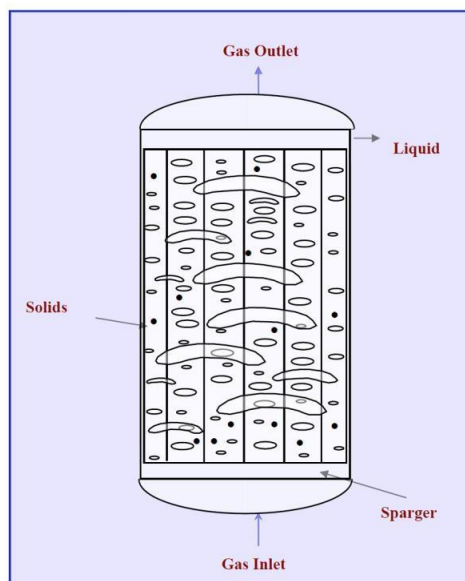


Figure.1. 2 Diagram of a slurry bubble column schematic [11].

Slurry bubble columns are advantageous as they can be used in a variety of industrial applications. Furthermore, the liquid in the three-phase reaction is beneficial as it allows for a more precise temperature control due to the liquid's high heat capacity [12]. Scaling up, modeling, and designing slurry bubble column reactors is a complex process as it requires detailed knowledge in relation to kinetics, hydrodynamics, heat and mass transfer, chemical reaction rates, phase holdup, flow regimes, pressure change, and solid distribution.

1.2.1. Gas holdup

One of the most important characteristics to describe a slurry bubble columns' performance is the gas holdup [13]. Gas holdup is a dimensionless parameter that represents the volume fraction of the gas in the SBCR. Similarly, the liquid and solid holdups represent the volume fractions of liquid and solid respectively. The total volume (V_t) of the three-phase system in the slurry bubble column reactors is presented below:

$$V_t = V_g + V_l + V_s, \quad (1.4)$$

where V_g , V_l , and V_s are the volumes of gas, liquid and solid respectively. The holdup of any phase (i) is defined as the volume fraction of the reactor occupied by this phase;

$$\alpha_i = \frac{V_i}{V_g + V_l + V_s} \quad (1.5)$$

The summation of all the phase holdups is 1 as seen below

$$\alpha_g + \alpha_l + \alpha_s = 1, \quad (1.6)$$

Where α_g , α_l , and α_s denote the gas, liquid, and solid phase holdups, respectively.

1.2.2. Heat Transfer

Thermal management is critical in the oxygen reactor because the decomposition reactions are often linked with endothermic operations. Due to their high heat transfer rates, bubble columns have been extensively employed in a broad variety of industrial products and activities [14]. Numerous hydrodynamic studies examine the heat transfer between heating elements and the system flow in order to further understand the impact of hydrodynamic structures on heat transfer with the aim of enhancing the bubble column reactor's design and operation [15]. In this thesis, direct contact heat transfer between the oxygen gas and the slurry of molten CuCl and solid Cu₂OCl₂ particles inside a SBCR will be examined using 3D CFD simulations.

1.2.3. CFD

Computational fluid dynamics (CFD) is the study of forecasting fluid flow, heat transfer, mass transfer, chemical reactions, and other related phenomena by the use of numerical methods to solve the mathematical equations governing these processes. CFD analysis produces meaningful engineering data that may be utilized in conceptual studies of novel designs, thorough product development, troubleshooting, and redesign, and so CFD is becoming increasingly popular in general process applications.

There are a variety of software available for engineers to work with for CFD analysis such as ANSYS fluent, CFX, Open Foam, and AVL Fire to name a few. CFD software is an extremely valuable tool as mentioned earlier. However, it is the engineers' responsibility to be able to create the model, analyze the data, and interpret the findings to be able to properly predict a designed systems performance [16].

1.3 Motivation

Climate change has become a growing concern. This has led to an increased focus on renewable energy, clean energy, and alternative fuels. One alternative fuel which has been gaining attention is hydrogen. The benefit of using hydrogen as an alternative fuel is that it does not produce any harmful byproducts when being converted into energy. Hydrogen can be converted into energy by using hydrogen fuel cells. Hydrogen can be produced using several methods which include gas reforming and electrolysis. The main challenge of hydrogen production is that the process is very energy intensive and can generate large amounts of pollutants and greenhouse gases. One method that can be used to reduce the amount of energy required to produce hydrogen and minimize pollutants is the implementation of a CuCl hydrogen production cycle.

In the UAE, the CuCl hydrogen production cycle can be coupled with Barakah Nuclear Power Plants to produce hydrogen as an additional clean source of energy. Another method of implementing the CuCl cycle in the UAE is to use solar thermal energy as a source of heat. The hydrogen could be used to store solar thermal energy and be used to generate clean energy as required. Coupling the CuCl cycle with these two industries which are available in the UAE could help produce additional clean energy which would aid in providing a more sustainable source of energy.

1.4 Objective

The objective of this thesis is to investigate the multiphase hydrodynamics of a direct contact heat transfer reactor between the O₂ gas bubbles and the molten salt slurry in the oxygen reactor for the CuCl cycle. This study will be a numerical study using 3D CFD simulations by implementing ANSYS Fluent software. The CFD models will be verified using previous experimental results from the literature

Chapter-2

Literature Review

2.1. The CuCl Cycle and Oxygen Reactor

There have been many patents and designs used to implement the CuCl cycle [17]. The CuCl cycle may have different number of steps to generate hydrogen from water. However, the end result is the generation of hydrogen and oxygen from water while all other chemicals in the cycle are regenerated. One of the most critical aspects of the cycle is the source of energy. If the energy sources which supplies the heat is renewable or clean it will aid in the preservation of the environment and valuable resources. Two sources can be used to supply heat to the CuCl cycle: solar thermal energy and nuclear heat.

Litwin and Pienkowski [18] patented an invention that utilizes both a thermochemical and a thermo-heating system to generate hydrogen. The invention aims to utilize solar power as a renewable energy source to power the hydrogen producing device. Litwin and Pienkowski's device uses a low temperature copper chloride thermochemical process with four chemical reactions. The net result of the entire cycle is the production of hydrogen and oxygen. All other reactants and products can be reused. Therefore, only a steady supply of water will be required for the continuous production of hydrogen and oxygen. The maximum temperature required in the cycle is approximately 530°C. The heat is generated through the solar heating system which collects solar energy. The energy is then transferred to a heating medium which is pumped from the hot thermal storage tank and circulated through the thermochemical system when the thermal energy is required. This drops the temperature of the heat transfer medium which is then returned

to the cold storage reservoir. The heating medium is kept in a closed loop solar heating system until is necessary to be used. The heating medium suggested in this patent is molten salt with a composition of roughly 40%-60% of sodium nitrate (NaNO_3) and roughly 40%-60 % of potassium nitrate (KNO_3) by weight [18]. However, the molten salt may be replaced with any medium with the ability to transfer and maintain heat of at least 590°C such as liquid metal. The proposed design claims to eliminate the need to operate at high temperatures, use of high temperature refractory materials, and use highly concentrated designs of solar thermal plants. Furthermore, the design claims to provide thermal and electrical energy to the system for up to 24 hours a day. The combination of the solar heating system and the thermochemical system results in improved overall efficiency, use of solar-powered hydrogen production systems, and improves operating costs.

Marin et al. [19] investigated the chemical streams that flow over the limits of the CuCl cycle's thermal reactions, as well as the process integration. Additionally, they investigated the effects of incomplete hydrolysis reactions on the kinetics and thermodynamics of the oxygen reactor in the CuCl cycle, focusing on the spontaneity of CuCl breakdown and the parameters (such as pressure and temperature) that limit chlorine emission.

Marin [20] produced a novel experimental and theoretical basis for scaling up a CuO/CuCl_2 decomposition reactor while taking into account the effect on the yield of the thermochemical CuCl cycle for hydrogen production. He applied a Stefan boundary condition in conjunction with a novel particle model to monitor the location of the moving solid-liquid interface as the solid particle decomposes due to surface heat transfer. Thermo gravimetric Analysis microbalance and laboratory size batch reactor studies were used to investigate the conversion of CuO/CuCl_2 and estimate the rate of endothermic reaction. At high temperatures and low Reynolds numbers, a

second particle model finds characteristics that affect the transient chemical breakdown of solid particles embedded in a bulk fluid composed of molten and gaseous phases. For a particle immediately submerged in a viscous continuum, the mass, energy, momentum, and chemical reaction equations were solved. The generated numerical solutions were evaluated using experimental data on the chemical breakdown of CuO/CuCl_2 .

2.2. Bubble Column Reactors

Over the years research has been conducted in relation to slurry bubble column reactors both experimentally and by means of CFD software's. Research conducted has investigated the effects of gas holdup, coalescence, reactor dimension, operational pressure, and heat transfer on the reactions. The research conducted will aid in future development and design of SBCRs.

Some of the numerical bubble column flow models that have been investigated are presented in the table below [21].

Table 2. 1 Bubble Column Flow Model Summary [21].

Multiphase models	Turbulence models	Interfacial force models	Ref.
Euler-Euler approach	$k - \epsilon$	Drag	Sanyal et al. (2005)
Euler-Euler approach Population balance approach	$k - \epsilon$	Drag	Olmos et al. (2001)
Euler-Euler approach Population balance approach	$k - \epsilon$	Drag, Lift	Bhole et al. (2008)
Euler-Euler approach Population balance approach	$k - \epsilon$	Drag, Lift	Díaz et al. (2008)
Euler-Euler approach Population balance approach	Standard $k - \epsilon$, RNG $k - \epsilon$, Realizable $k - \epsilon$	Drag	Laborde-Boutet et al. (2009)
Euler-Euler approach	RNG $k - \epsilon$	Drag	Li and Zhong (2015)
Euler-Euler approach Population balance approach	RNG $k - \epsilon$	Modified Drag	Liang et al. (2016)
Euler-Euler approach	RNG $k - \epsilon$	Drag	Troshko and Zdravistch (2009)
Euler-Euler approach Population balance approach	RNG $k - \epsilon$	Drag	Xu et al. (2014)
Euler-Euler approach Population balance approach	$k - \epsilon$	Drag	Chen et al. (2005)
Euler-Euler approach	$k - \epsilon$, RSM LES	Drag, Lift, Turbulent Dispersion, Added Mass	Wang et al. (2005)
Euler-Euler approach Population balance approach	$k - \epsilon$, RSM	Drag, Lift, Turbulent Dispersion	Silva et al. (2012)
Euler-Euler approach Population balance approach	Standard $k - \epsilon$, RNG $k - \epsilon$, Laminar and RSM	Drag, Lift, Virtual Mass	Gupta and Roy (2013)
Euler-Euler approach	Standard $k - \epsilon$, LES	Drag, Lift, Turbulent Dispersion, Added Mass	Dhotre et al. (2008)

2.2.1. Hydrodynamic Investigations

Matiazzo [22] conducted a 3D CFD investigation of a gas-liquid flow in a churn turbulent regime in order to compare the effectiveness of several models in relation to predicting the drag closures, breakup, and coalescence. Twelve combinations of the breakup and coalescence models were created and simulated. The combinations included a mixture of the breakage closures and coalescence closures. The Breakage closures used were Luo and Svendsen(1996), Lehr et al. (2002), Laakkonen et al. (2006), and Laakkonen et al. (2006) with Generalized PDF distribution. The coalescence closures used were Prince and Blanch (1990), Lu(1993), and Das (2015). Once simulated the CFD models were compared to the experimental data of Manjrekar and Dudukovic (2015). The Manjrekar and Dudukovic bubble column reactor have a cylindrical diameter of 20.32 cm and a height of 2m. Experiments were carried out on the combination of 12 models with air-water flows at superficial gas velocities of 20 cm/s and 40 cm/s.

The results highlighted the importance of selecting the appropriate breakage and coalescence closure model. In particular the breakup model, as the breakup model had a larger impact on the flow prediction than the coalescence model. The key findings of this report indicated that the Luo and the Prince and Blanch models for coalescence were similar in results and were both able to best predict the experimental data points at 6.2% and 7.2% relative error at a superficial gas velocity of 20 cm/s. When considering the breakup closure a combination of the Laakkonen et al. (2006) model with the generalized PDIF distribution coupled with the breakage generating three daughter bubbles resulted in an acceptable prediction of the experimental results. Additionally, this combination was the least computationally expensive for the break up closure simulations. The Schiller and Naumann (1935) model was found to be the best model to predict the drag closure in comparison to experimental data. Overall, the simulated results were able to predict the experimental data

with low relative errors for the gas axial velocity (7.7% at 20 cm/s and 14.0% at 40 cm/s) and for the gas holdup (14% at 20 cm/s and 21.9% at 40 cm/s). The computational predicted data for the gas axial velocity in the center of the bubble column showed better agreement with the results than the predictions near the wall. The simulated results near the wall were over predicted in comparison to the experimental data.

Ertekin et al. [23] validated the hydrodynamic CFD models presented by Fletcher et al. (2016) while varying conditions such as column diameter from 0.19 m to 3m and the superficial gas velocities which varied from 0.03 m/s to 0.25 m/s based on the experimental data of Raimundo et al. (2019) and Mclure et al. (2014). Furthermore, Ertekin et al. validated the experimental model using the effects of different phase materials on the gas holdup versus superficial gas velocity as well as the oxygen transfer rates versus the superficial gas velocity. The experimental variations are presented in the table below. The Fletcher et al. [24] model used in this validation was a two-phase Euler- Euler model using a fixed single bubble size. A standard k- ϵ turbulence model was used for the liquid phase, while the gas phase was modeled using a dispersed phase zero equation. Bubble induced turbulence was accounted for using the Yao and Morel model. Ertekin et al. verified the models used by Fletcher, finding that there was a minimal percent difference when studying the holdup. It was observed that there was a percent difference of 3%- 10% between experimental and simulated data for the water, air phases. Simulated results were under predicted near the center of the column when the height to diameter ratio was 3.75. This was the largest discrepancy. When using organic liquid phases and phases which included surfactants, the proposed model showed good agreement in the gas holdup to superficial velocity data points. Some phase results were more agreeable than others. Furthermore, good agreement of the simulation with the experimental data was observed for results pertaining to the oxygen transfer rate vs the superficial velocity. The results obtained from

this test however may vary depending on the surfactant concentration and type of surfactant presented in the experiment.

Table 2. 2 Validation Studies summary used by Ertekin et al. [23].

Experimental data taken from	Column diameter (m)	Column height (m)	Liquid height (m)	U_G (m s ⁻¹)	d_b (mm)	Phases
Maximiano Raimundo et al. (2019)	1	6.5	4	0.03	5	Air/water
Maximiano Raimundo et al. (2019)	1	6.5	4	0.16	5	Air/water
Maximiano Raimundo et al. (2019)	1	6.5	4	0.25	6	Air/water
Maximiano Raimundo et al. (2019)	3	12	6.6	0.15	5	Air/water
Maximiano Raimundo et al. (2019)	3	12	6.6	0.2	4	Air/water
Wilkinson et al. (1992)	0.23	1.8	1.2	0.037, 0.097, 0.13 and 0.17	6	N ₂ /water
Wilkinson et al. (1992)	0.23	1.8	1.2	0.041, 0.081, 0.11 and 0.18	6	N ₂ /n-heptane
Wilkinson et al. (1992)	0.23	1.8	1.2	0.03, 0.0875, 0.116 and 0.157	6	N ₂ /monoethylene glycol
McClure et al. (2014a)	0.19	1	0.5	0.028, 0.06 and 0.108	6	Air/water
McClure et al. (2014a)	0.19	1	0.5	0.028, 0.06 and 0.108	4	Air/water + 0.02 M 2-propanol
McClure et al. (2014a)	0.19	1	0.5	0.028, 0.06 and 0.108	15	Air/water + 0.01% (v/v) Antifoam A
McClure et al. (2015a)	0.19	1	0.5	0.028, 0.044, 0.082 and 0.108	5	Air/water + 0.5 M sodium sulphite
McClure et al. (2015a)	0.19	1	0.5	0.028, 0.044, 0.082 and 0.108	5	Air/water + 0.5 M sodium sulphite and 0.01% (v/v) Antifoam Y-30

Yan et al. [25] used three different optimized drag models to simulate the hydrodynamics of a high pressure, air-water bubble column. The effects of changing the superficial gas velocities (0.121, 0.174, 0.233 and 0.296 m/s) and the effects of changing the reactors pressure (0.5, 1.0, 1.5 and 2.0 MPa) on the radial gas holdup were investigated. The bubble column reactor had a diameter of 0.3m and a height of 6.6m. The gas sparger has 128 opening at a size of 5mm each located 0.2m from the base of the reactor. The data was investigated using 2D and 3D CFD simulations and compared to experimental calculated data using the electrical resistance tomography method. The first optimized drag model was based on Roghair's drag model in which correction were made by introducing the gas holdup of large and small bubbles to aid in density correction. The second model neglected the gas holdup effects of small bubbles with diameters smaller than 0.08m and combined their effects with the liquid phase. The third model was modified using an energy minimization multiscale (EMMS) approach based on the double bubble size model and a link between the drag coefficient and bubble diameter was implemented in the model. After

completing the analysis several conclusions were drawn. It was noticed that as the superficial gas velocity increased so did the radial gas holdup in the bubble column in the cold-water air model. Additionally, increasing pressure within the reactor increases the radial gas holdup. Although all three models tested in this report were different, they were all capable of depicting the trends of the drag coefficient in relation to the changes with superficial gas velocity and pressure differences. It was noted that bubble size has a key impact on the mass and heat transfer and that using a PBM (Population Balance Model) model should be investigated. Lastly, it was noted that the middle of the bubble column is most likely to have the greatest gas holdup. This was observed in both the 2D and 3D simulations as well as in the experimental bubble column.

Sarhan et al. [26] investigated the effects of the physico-chemical properties of the liquid and gas phases on bubble formation and hydrodynamics of a bubble column reactor using the population balance equation combined with a 3D CFD model. The bubble column reactor was designed after the experimental reactor constructed by Abdulrahman [4,27-30] with a diameter of 0.216m, a column height of 0.915m and a liquid height of 0.65m (Figure 2.1). The experimental data conducted by Abdulrahman [4,27,30] were used to validate the CFD model predictions. The 2-phase flows were conducted with different materials for gas and liquid. The gases used were helium, air and argon. The liquids used were water and paraffin oil. The CFD model was then used to predict the gas holdup, Sauter mean bubble size distribution and local time average bubble velocity within the column reactor using the different phase flows at different velocities (0.01, 0.05, 0.09 and 0.13 m/s). Sarhan et al. were able to create an Euler-Euler CFD model to predict experimental results of the gas holdup in a bubble column reactor using different phase flows within the range of $\pm 7\%$. Additional conclusions which were drawn from the experiment include, the observation that the gas holdup will increase slightly as the gas phase density increases. If the liquid

phase has a lower density such as paraffin oil the average gas holdup will increase significantly. If water is used as the liquid phase the bubble rise velocity will increase significantly. However, the bubble rise velocity will decrease if there is an increase in the gas phase density. Lastly, Sarhan et al. concluded that if the liquid phase density increases so will the Sauter mean bubble diameter. The Sauter mean bubble diameter will decrease as the gas phase density increases.

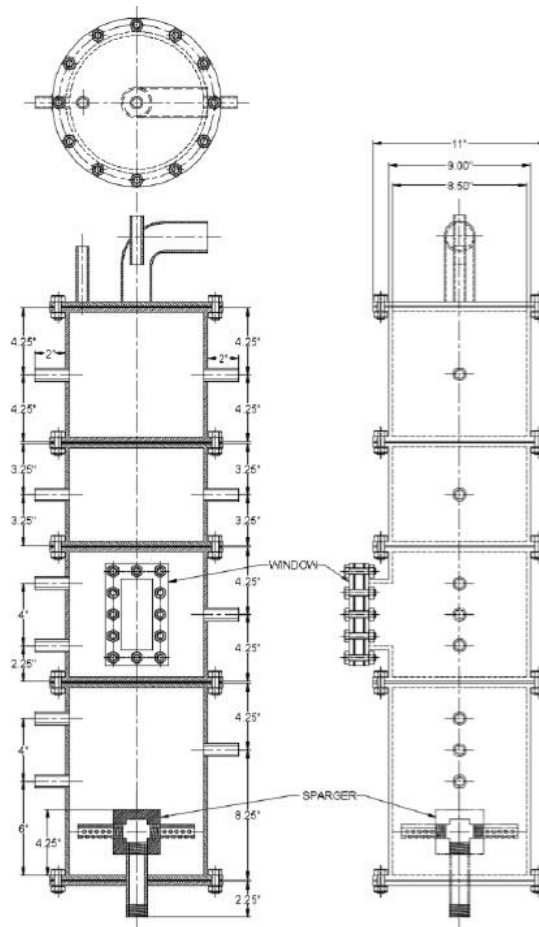


Figure. 2. 1 Experimental bubble column reactor used by Abdulrahman [4].

Adam and Tuwaechi [31] generated a 2 phase, gas - liquid, Eulerian- Eulerian, k- ϵ mixture turbulence CFD model, to study the effects of gas holdup and superficial gas velocity on the hydrodynamics using a course and fine mesh. The bubble column reactor simulated had a height of 0.96 m and a diameter of 0.19m. From the CFD model it was observed that as the time step increased so did the volume fraction. The finer mesh with a

grid resolution of 0.005 lead to a clearer observation. The last observation made by Adam and Tuwaechi was that the highest pressure was observed near the gas inlet and gradually decreases when moving away from the inlet.

Li et al. [32] conducted both experimental and CFD hydrodynamic analysis of an air-water-glass beads slurry bubble column (Figure.2. 2). The experiments conducted investigating the effects of changing the reactor diameters (0.2, 0.5 and 0.8m). The reactions occurred at high superficial gas velocities ranging from 0.12 to 0.62 m/s with varying solid concentrations from 0% to 30%. The effects of the changing parameters on the gas holdup, time average liquid flow and kinetic energy were recorded. The slurry bubble column reactor was modeled using a 2D axisymmetric two fluid Euler k- ϵ model. The research conducted lead to several conclusions. It was observed that as the superficial gas velocity increases so the does the average gas holdup. Additionally, it was noted that as the average gas holdup increases so does the averaged liquid velocity and turbulent kinetic energy. Bubble breakage was hindered by the presence of solid particle which led to an increase in bubble rise velocity and a reduction in gas holdup. The solidconcentration led to a small change in time average axial liquid velocities. Furthermore, it was noted that the change of hydrodynamic characteristics with column diameters is the major cause of bubble column scale-up rules. Bubble columns with wider reactor diameters result in the axial liquid velocity rising dramatically within the column core, while the gas holdup is very minimally influenced. Lastly, it was noted that with increasing column scales, turbulent kinetic energy rises.

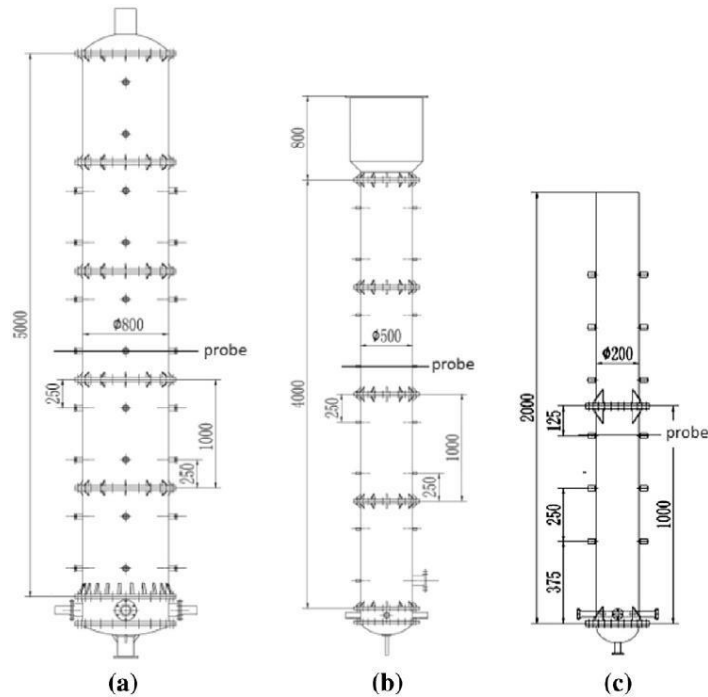


Figure. 2. 2 Slurry bubble columns used by Li et al. [32].

Pourtousi et al. [33] investigated the bubble column regime and the effects of changing superficial gas velocity (0.0025 – 0.015 m/s) and varying bubble diameters (3, 4, 5 and 5.5mm) on the Euler-Euler simulation flow pattern predictions. A 3D air water CFD simulation was created with a slurry bubble column with a height of 2.6m and diameter of 0.288m. The simulated ring sparger had 20 holes and a diameter of 0.14m. The simulated data was then compared to experimental data to ascertain the effectiveness. It was noted that it is crucial to observe the size and shape of the bubbles formed near the sparger in the experiment to accurately predict the bubble's simulated hydrodynamics. A 3mm bubble diameter for superficial gas velocities ranging from 0.0025-0.015 m/s led to acceptable simulated predictions near the bulk region. However, when considering data near the sparger, a bubble diameter of 5 or 5.5 resulted in a better predicted simulated result. Considering a single bubble diameter can result in an acceptable prediction in the homogeneous regime as it is less computationally expensive. The same cannot be assumed for a heterogeneous regime as it would lead to inaccurate results. In order to achieve more

accurate simulated results for a heterogeneous regime a range of bubble diameters should be included as well as the implementation of a drag model in the simulation.

Heterogeneous flows have bubbles with different shapes and sizes which range from 0.05mm to 50mm. Conversely, homogeneous flows have consistent bubble shapes and sizes that have minimal interaction with each other within the bubble column reactor.

Li and Zhong [34] conducted a 3D, Eulerian-Eulerian-Eulerian, three phase (air-water-glass powder), time dependent, CFD analysis of three different bubble column reactors to study the hydrodynamics in relation to time step, momentum discretization schemes and wall boundary conditions as well as a sensitivity analysis using different drag models. The three different models used were the Gandhi et al. (height: 2500mm, Static height: 1500mm diameter: 150mm), the Rapure et al. model (height: 2000mm static height: 1000mm diameter: 200mm) and the Li and Zhong model (height: 800mm width: 100mm depth: 10mm) (Figure 2.3). The turbulence model used for their simulations was the RNG k- ϵ model. Li and Zhong concluded that the conditions that best reflected experimental results were the use of a no slip condition, momentum discretization using the second order upwind, and a time step of 0.001s. While considering the drag forces it was found that modeling the gas-liquid drag model was best using the Zhang- Vanderheyden model. While considering liquid-solid drag models the Schiller -Naumann model was best. Furthermore, it was noted that the bed gas holdup was heavily influenced by the superficial gas velocity. It was observed that as the superficial gas velocity increased so did the time average gas holdup and the liquid axial velocity however, the local solid holdup dropped. On the distributions of solid holdup and liquid axial velocity, the impacts of solid volume fraction ($V_s=0.03-0.30$) and particle size ($d_p=75\ \mu\text{m}-270\ \mu\text{m}$) were stronger than those of particle density ($\rho_p=2500\ \text{kg/m}^3-4800\ \text{kg/m}^3$). When the particle size d_p was less than 150 μm and the solid volume fraction V_s was less than 0.09, the effects of solid volume fraction and

particle size were more noticeable. The bed solid volume fraction distributions can be effectively described by the axial distributions of solid holdup. The axial solid concentration gradient was higher the larger the solid volume fraction, particle size, and particle density values were. Solid volume fraction had a bigger influence on radial gas holdup than the other two particle attributes, while both solid volume fraction and particle size had a greater effect on liquid axial velocity. When the solid volume fraction and particle size rose, the liquid axial velocity in the bed center portion dropped.

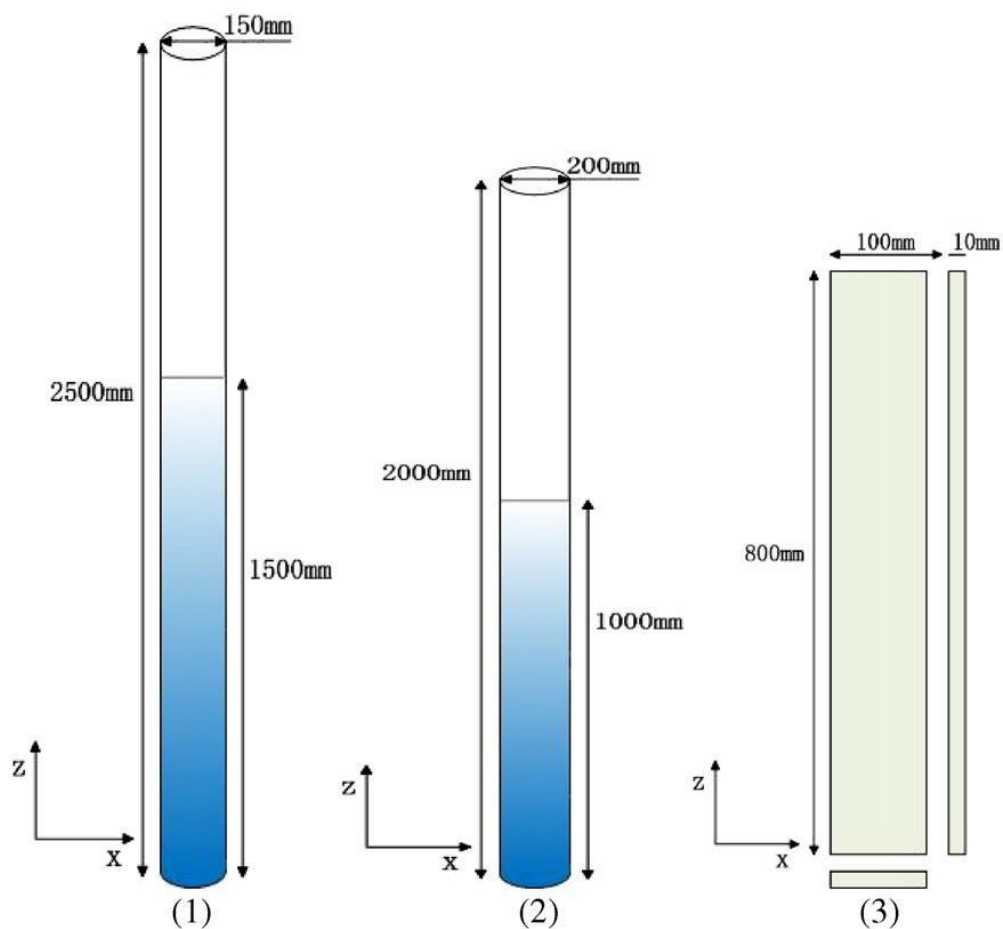


Figure. 2. 3 Bubble column reactors investigated by Li and Zhong [34]. 1) Gandhi et al. 2) Rampure et al. 3) Li and Zhong.

2.2.2. Effects of Solid Particles

Abdulrahman [35] investigated the effects of varying the solid concentrations from 0%, 5% and 10% on the gas holdup with reactor diameter of 21.6 cm and heights of 45 cm and 65cm. The study was conducted using a 2D CFD software assuming a 2-phase slurry

of water and helium. The system was modeled using a multiphase Eulerian model with a viscous-standard k- ϵ turbulence model. The results indicated that as the concentration of solid particle increases the gas holdup decreases. This relationship remains true at any static liquid height and any specific superficial gas velocity.

Zhou et al. [36] analyzed the effects of particles on a gas liquid flows in a slurry bubble column using a conceptual model. The particle dependent dual bubble size (PDBS) model was created to investigate the effects of viscosity and density changes due to the addition of particles, as well as the change to the bubble drag co-efficient due to presence of particles. The model was a three-phase model composing of air, water, and glass beads. The PDBS was tested using CFD simulations using three different reactor designs. The three different bubble column reactor setups that were used to test the PDBS was the 3D square Ojima et al. reactor, the 3D cylindrical Gandhi et al. and the 2D Tyagi and Buwa reactor as depicted in Figure.2. 4.

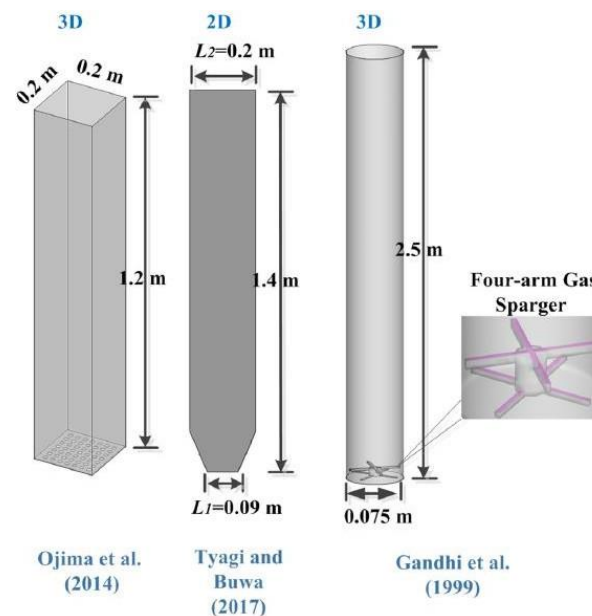


Figure. 2. 4 Bubble column reactor setups tested for the PBDS model [36].

Zhou et al. [36] came to several conclusions while testing the PDBS model. When considering the effects of viscosity and density it was observed that there was a higher level

of stability with increased slurry viscosity and density. This was apparent as there was a delay in the flow regime transition to a higher flow rate. In regards to the changes with the bubble's drag coefficient using the PDBS model it was concluded that bubble coalescence is encouraged in the presence of wettable particles. This conclusion is agreeable with experimental data as the overall gas holdup and energy consumption of bubble breakage decreases using the PDBS model. The PDBS model can predict results for the gas holdup and bubble breakage with changes in solid concentration. Overall, it was concluded that the increase in solid concentration will result in a decrease of the gas holdup.

Abdulrahman [4,37] developed a CFD simulation to predict the effects of changing static liquid heights (45cm, 55cm, and 65mm) and superficial gas velocities (0.05 m/s, 0.1 m/s and 0.15 m/s) on gas holdup and compared the results to experimental results. A 2D CFD simulation of a 2-phase slurry consisting of water and helium to analyze the hydrodynamics in steady state was developed. The reactor diameter was fixed at 21.6 cm. The study concluded that at any superficial gas velocity the overall gas holdup would increase if the superficial gas velocity increased. However, at any superficial gas velocity the gas holdup would decrease if the static liquid height was increased. It was noticed that the gas holdup was unevenly distributed along the cross section of the column, where higher gas holdups were found in the center and lower gas holdups were found near the wall. When comparing the CFD results to experimental data it was found that the gas holdup in the simulations were under-predicted. While, CFD results of the reactor's height effects on the gas holdup was correctly predicted.

Chen and Brooks [38] conducted both experimental and 3D analysis of a cylindrical bubble column to study the mass transfer and hydrodynamics. The cylindrical reactor had a diameter of 5 inches, a high of 6.55 inches, and a gas inlet at the center of the reactor with a diameter of 0.12 inches (Figure.2. 5). The experiment was conducted with 2 phase flows

of deionized water and air. Scenarios in this experiment were limited to small void fraction cases in which the bubbles may be easily observed. Flow visualization was then used to create a new approach for obtaining a 2D void fraction profile when the void fraction was low. The approach of image processing is used in the Particle Image Velocimetry tests to reduce reflection disturbance. Concentration distribution was not measured in relation to the dissolved oxygen experiment as the mixing occurred rapidly in the small reactor. Under the same conditions, comparisons are done between experiments and the simulations for gas holdup, void fraction profile, liquid velocity field, and volumetric mass transfer coefficient. Conclusions reached in this paper suggest that validation should be conducted with time averaged data, if bubble induced turbulence and turbulent dispersion forces are taken into consideration. Volume average void fractions using the CFD model were predicted within an acceptable limit. It was observed that monitoring the void fraction and velocity profile could be predicted a few centimeters away from the inlet, however predictions directly above the inlet was limited. CFD is a valuable tool when simulating low void fractions as it shows good agreement with experimental data. However, for higher gas flow rates the results obtained from visualization and Particle Image Velocimetry methods stray from the CFD data leading to higher levels of uncertainty which may result in an unreliable CFD model. When considering complex conditions and higher void fractions to study heat and mass transfer it is important to include turbulence for two phase flows as it will lead to more agreement between the experimental and simulated results.

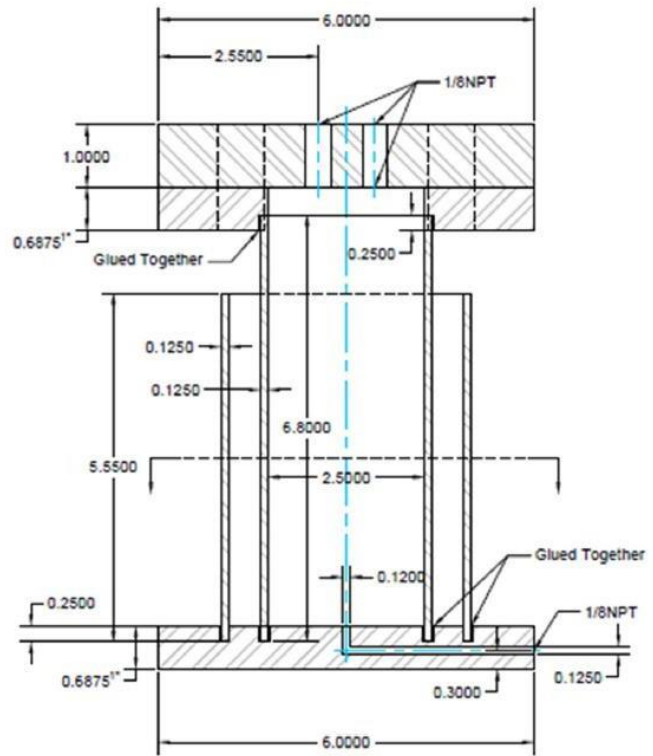


Figure. 2. 5 Experimental bubble column reactor investigated by Chen and Brooks [38].

Sarhan et al. [39] used the experimental data of Bhunia, Kundu and Mukherjee to create a 3-dimensional flow simulation of a flotation column reactor. The simulation was used to predict the bubble surface area flux while varying the superficial gas velocity (0.64 cm/s to 2.76 cm/s), and the solid particle concentration (5% and 10%) and type (sphalerite and coal). The model used to conduct the simulation was an Eulerian- Eulerian with a k- ϵ dispersed turbulence model. The reactor simulated had a height of 1.66m with a diameter of 0.1m. Conclusions drawn by Sarhan et al. include that increasing superficial gas velocity increases the bubble surface area flux. Increasing the solid concentration and/or the hydrophobicity will decrease the bubble surface area flux at any given superficial gas velocity. Additionally, it was noted that as the coal concentration was increased from 0% to 10% the surface area flux reduced by 28%. However, if sphalerite was present the bubble surface area flux increased by 7%. Lastly, it was observed that the addition of hydrophobic particles leads to a decrease in bubble concentration by approximately 23% assuming the same operating

parameters.

Wodolazski [40], generated a 3D CFD simulation of a slurry bubble column reactor to analyze the flow of syngas in a 3-phase flow (syngas, paraffin oil, solid particles). An Eulerian- Eulerian approach was used with a k- ϵ turbulence model. The reactor modeled had a height of 1.4 and a diameter of 0.4. The distributor was located 0.14m away from the center of the columnbase with a diameter of 0.027m. Parameters analyzed in this study included the superficial gas velocity (0.05, 0.1, 0.2 and 0.3m/s), initial solid particle concentration (10%, 30% and 50%), gasholdup, and bubble size distribution. The report concluded that increasing the inlet gas velocity led to the improvement of the axial gas holdup. Increasing the slurry concentration leads to a decrease in axial gas holdup. Additionally, the increase of the slurry concentration leads to a decrease in the bubble breakup rate. An approximate parabolic relationship was observed between the effects of the gas velocity and the axial solids holdup profile.

2.2.3. Heat Transfer

Abdulrahman [41-42] studied the direct contact heat transfer of a helium – water – alumina slurry bubble column reactor using a 2D CFD simulation to ascertain the average temperature of the surly when the superficial gas velocity, static liquid height, and solid particle concentration are varied. The inlet gas (helium) in this simulation would enter the reactor at a high temperature (90°C) and interact with the water alumina slurry (22°C). The model used was a 2D, 2 phase Eulerian-Eulerian model with an Eulerian sub model with a standard k- ϵ turbulence model. The simulated reactor was designed with a diameter of 21.6cm. The column heights for this simulated experiment were varied between 45, 55, and 65 cm. The superficial gas velocities ranged from 0.03 to 0.15 m/s. While the solid concentration examined were 0%, 5% and 10%. Abdulrahman [41-42] was able to conclude that increasing the superficial gas velocity will increase the average slurry temperature. The

average slurry temperature can also be increased by decreasing the column height. Furthermore, it was observed that changing the concentration of the solid particles in the slurry has a minimal effect on the average slurry temperature. While comparing the CFD data to experimental data it was observed that the average slurry temperature was under predicted with a maximum relative error of 0.4% which shows good agreement. Overall, the CFD data was able to predict the trends that were affected by the changing the reactor height and slurry particle concentration on the average slurry temperature.

In another study, Abdulrahman [43] investigated the volumetric heat transfer coefficient. A simulation was created with similar parameters as mentioned above. The simulated results showed good agreement with experimental data. Conclusions derived from this simulation reveal that when the superficial gas velocity increases so does the volumetric heat transfer. However, when the column height or the solid concentration decreases the volumetric heat transfer coefficient increases. Additionally, it was observed that approximately the same decrease in solid concentration was also observed in the volumetric heat transfer coefficient at different superficial gas velocities.

Pu et al. [44] conducted a 2D CFD simulation of a molten salt bubble column, to investigate the hydrodynamics and direct heat transfer characteristics of a two-phase flow model (air – molten salt). The simulated bubble column has a diameter of 0.15m and height of 1.2m. An Euler- Euler multiphase model with a k- ϵ turbulence model was used. Factors investigated during the simulation include changing the superficial gas velocity (0.05, 0.1, 0.15, 0.2 and 0.3 m/s), varying the static liquid heights (0.55, 0.61, 0.65 and 0.7m), and using different operational pressure (1, 2, 3 and 5 bar) and inlet gas temperature (650K, 700K and 800K). Pu et al. made several observations. It was observed that as the superficial gas velocity or the operational pressure increases so does the molten salt temperature and rising rate of the molten salt temperature over time. However, when the static liquid height

rises, the rate of increase in average molten salt temperature falls. Increases in superficial gas velocity or operating pressure enhance the volumetric heat transfer coefficient, whereas increases in static liquid height lower the volumetric heat transfer coefficient.

Zhang and Luo [45] generated a 2 phase (air-water) CFD model to investigate a bubble column's local gas-liquid slip velocity distribution in relation to heat transfer in a heterogeneous regime. The study also investigated the simulated time average of the local 2 phase slip velocities when varying superficial gas velocities, axial locations and scale of the bubble column. The model used was a CFD –PBM (population balance model) simulation with a RNG k- ϵ turbulence. The reactor size investigated follows the experimental data of Al-Dahhan and coworkers with a diameter of 0.44m and varying heights of 2.4, 3.2, 3.66 and 3.65m. The superficial gas velocities simulated include 0.05, 0.2 and 0.35 m/s. It was observed that raising the superficial gas velocities raised the local gas-liquid slip velocities in the region of developed flow. While raising the r/R leads to a decrease in the local gas-liquid slip velocities in the region of developed flow. At larger superficial gas velocities, it was noticed that the slip velocities were more affected by the radial position. The slip velocities near the center of the column were lower than that of the fully developed region. The slip velocities were minimally affected by the axial heights for the fully developed flow regions. The radial profiles of gas–liquid slip velocities in the sparger and fully developed flow areas, on the other hand, show clear discrepancies.

Furthermore, the radial profiles of gas–liquid slip velocities, gas velocities, and liquid velocities differ significantly. The variations between gas holdup profiles and slip velocity profiles are minor in comparison. The local heat transfer coefficient in the pilot scale bubble column raised as the local gas liquid slip velocities rose in the fully developed flow region. At superficial gas velocities of 0.05m/s and 0.35m/s the local heat transfer coefficient and local gas-liquid slip velocities demonstrated a linear relationship. The findings imply that

in the fully developed region of bubble columns, there is a strong relationship between local gas–liquid slip velocities and local heat transfer coefficients.

Li et al [21] investigated the effects of a circular heat exchanger using a 2D CFDPBM model on the hydrodynamics of a pilot scale slurry bubble column reactor (Figure.2. 6). An Euler –Euler multiphase model with an RNG k- ϵ turbulence model was used. The reactor investigated had a diameter of 30cm, height of 200cm and the circular heat exchanger had a height of 108cm. Paraffin oil and catalyst particles were the assumed materials in the simulation. Variables changed in the simulation to investigate the hydrodynamics included the variation of the gas distributor's axial position from 0.025-0.06m, the superficial gas velocity was changed within the range of 0.017-0.085 m/s, and the amount of slurry that was initially loading from (0.845 -0.900m. Several conclusions were drawn from this experiment. It was observed that the gas phase was notably distributed, local circular vortices were generated, and the slurry was strongly circulated due to the implementation of the circular heat exchanger tube. This aids in mass and interphase momentum transfer. The bimodal profile of the gas holdup profile in the radial direction is caused by the circular gas distributor's particular layout. Furthermore, the circular heat exchanger tube increases this distribution, resulting in a larger gas holdup, which facilitates momentum transfer. Moreover, it was noted that variations in the operational parameters did not affect the gas holdup profile's bimodal structure. The local and whole time average gas holdup is enhanced by raising the superficial gas velocity. Too much slurry loading causes the reactor to be evacuated at increased gas velocity. While an excessive increase in the initial slurry loading volume has little influence on momentum transmission in the area around the heat exchanger tube. Lastly it was concluded that the ideal gas distributor axial height is 0.03m for this experiment. By placing the gas distributor at this height, the momentum and mass transfer was improved.

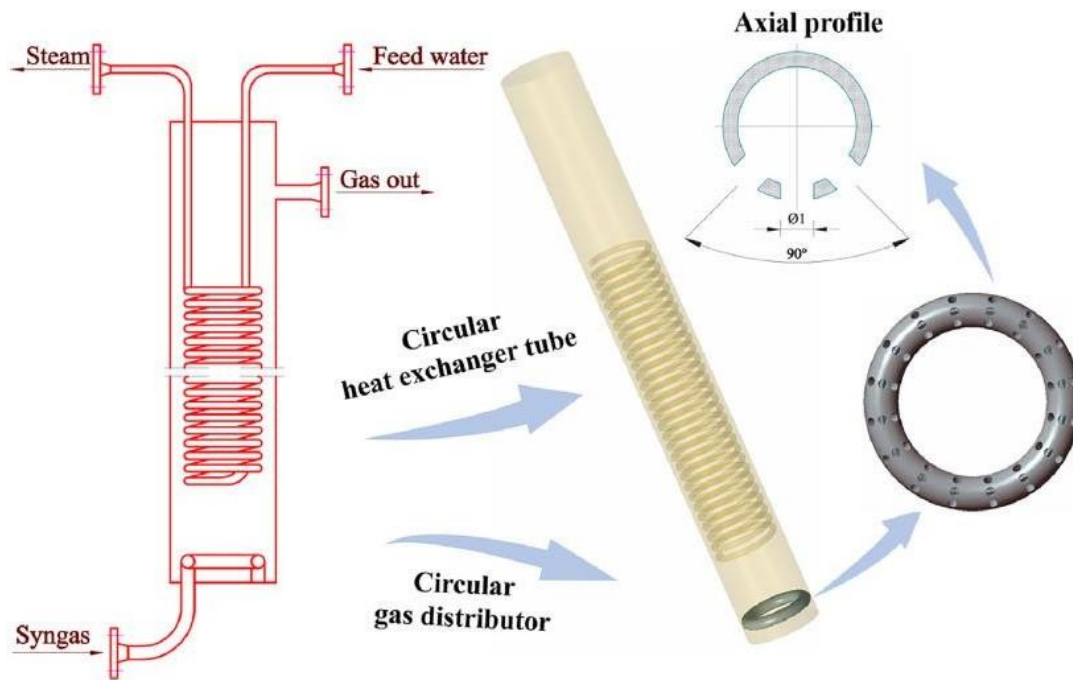


Figure. 2. 6 Bubble slurry column reactor and gas distributor used by Li et al. [21].

2.2.4. Process Intensification

Geng et al. [46] conducted a review of process intensification for slurry reactors agitated by pneumatics. The review focuses on bubble column reactors and airlift loop reactors. It highlighted the recent intensification advancements for mixing and mass/ heat transfer, intensification processes for mixing and separation, challenges and considerations related to different aspects of the reactor, and introduced the possibility of using CFD to design slurry reactors and potential obstacles. The review concluded with several vital remarks. The remarks pertaining to bubble column reactors in order to intensify the mixing or mass/ heat transfer reactions typically implement vibrating excitement or the use of internals such as tubes, perforates plates, static mixers, and structuring or a combination. The enhancement properties on the hydrodynamics and mass/heat transfer are reliant on the reactor's design and operational parameters. It is preferred to operate at high superficial gas velocities and high solid loading while in a churn turbulent flow regime to promote a high space time yield. Geng et al. [46] also notes that the developed CFD models need to be

validated with experimental data as they can be a useful tool while simulating hydrodynamics and transfer reactions. CFD-PBM models are very promising however, they have limitations as they cannot predict heterogeneous regime's bimodal bubble size distribution as well as different bubble coalescence and breakup models may result in different bubble size distributions. The table below identifies some of the CFD studies conducted on pneumatically agitated slurry reactors. It can be noticed that the investigations related to bubble column are CFD-PBM models with a main focus on the bubble coalescence and bubble breakup.

Table 2. 3 Pneumatically agitated slurry reactor investigated numerically [46].

Refs.	System	Model	Validated parameters	Key points
Huang et al. [191,192]	Gas-liquid IALR	2D steady-two-fluid model	$\epsilon_g, k_1 a$	Boundary condition: relative velocity between gas and liquid equals to the bubble terminal velocity
Oey et al. [193]	Gas-liquid-solid IALR	2D pseudo two-fluid model	ϵ_g, u_i , solid distribution	Solid velocity is the combination of liquid velocity, gravity, and turbulent dispersion
Wang et al. [194]	Gas-liquid-solid EALR	2D pseudo two-fluid model	ϵ_g, u_i , bubble rise velocity	Modeling the riser section, solid was considered by the liquid-solid physical properties
Chen et al. [195,196]	Gas-liquid bubble column	2D & 3D CFD-PBM	ϵ_g, u_i , bubble size distribution	Comparison of bubble breakup and coalescence models; increased ten times breakup rate predicted by models
Frank et al. [197]	Gas-liquid	CFD-PBM inhomogeneous MUSIG	ϵ_g, u_g	Gas phase is divided into N inhomogeneous velocity groups with M bubble size classes for each group
Yang and Xiao [198]	Gas-liquid bubble column	CFD-PBM	Bubble size distribution	New approach to calculate the coalescence rate through energy-minimization multi-scale concept
Lehr et al. [199]	Gas-liquid bubble column	CFD-PBM	ϵ_g, u_g, u_i , bubble size distribution	New model for bubble breakup was developed; simplified population balance by utilizing average volume fraction
Ni et al. [200]	Gas-liquid oscillatory baffled column	2D & 3D two-fluid model	Flow pattern	3D simulation of the flow pattern in oscillatory baffled column was first performed
Lestinsky et al. [201]	Gas-liquid IALR	2D two-fluid model	ϵ_g, u_i	Influence of draft tube geometry and equipping location on hydrodynamics were studied
Moraveji et al. [112]	Gas-liquid packed bed IALR	2D two-fluid model	$\epsilon_g, u_i, k_1 a$	Turbulence influences, gas holdup, liquid velocity, and mass transfer were investigated

All the symbols in this table are defined in the Nomenclatures list at the end of this paper.
2D: two-dimensional; 3D: three-dimensional; PBM: population balance model.

2.3. Summary of the Literature Survey

As a result of the above examination of the literatures, it can be concluded that 3D CFD simulations of the thermal hydraulics for the oxygen slurry bubble column reactor with direct contact heat transfer in the CuCl cycle have not been investigated before. Additionally, it is found that prior CFD studies on slurry bubble column reactors explored the hydrodynamics of the reactors using PBM models and the heat transmission of the reactors through indirect heat transfer from inside objects. This thesis will address the aforementioned gaps by performing 3DCFD simulations of the slurry bubble column

reactor's hydrodynamics with direct contact heat transfer at the operating conditions of the oxygen reactor in the CuCl cycle.

Chapter-3

CFD Simulation Model

In this chapter, the CFD reactor design, operating conditions, mathematical model, material properties for both the Water-Helium-Alumina and the Cuprous Chloride-Oxygen systems are investigated thoroughly. Additionally, the Water-Helium-Alumina model was validated against experimental data.

3.1 Slurry Bubble Column Reactor Geometry

The simulations of this thesis are validated against the experimental data provided by Abdulrahman [4]. As such the simulated reactor is designed to be a simplified version of the physical reactor to reduce computational costs. The experimental reactor was constructed of stainless steel with a diameter of 21.6 cm. A stainless-steel distributor is inserted 10.8cm above the base of the SBCR. The gas was fed into the SBCR using a six-arm sparger type gas distributor. Each arm of the sparger had 12 orifices with 0.3cm diameters (72 holes in total). The orifices on the sparger were 4.4 cm, 5.5, 6, and 6.8cm from the center of the reactor [4] as seen in Figure. 3.1.

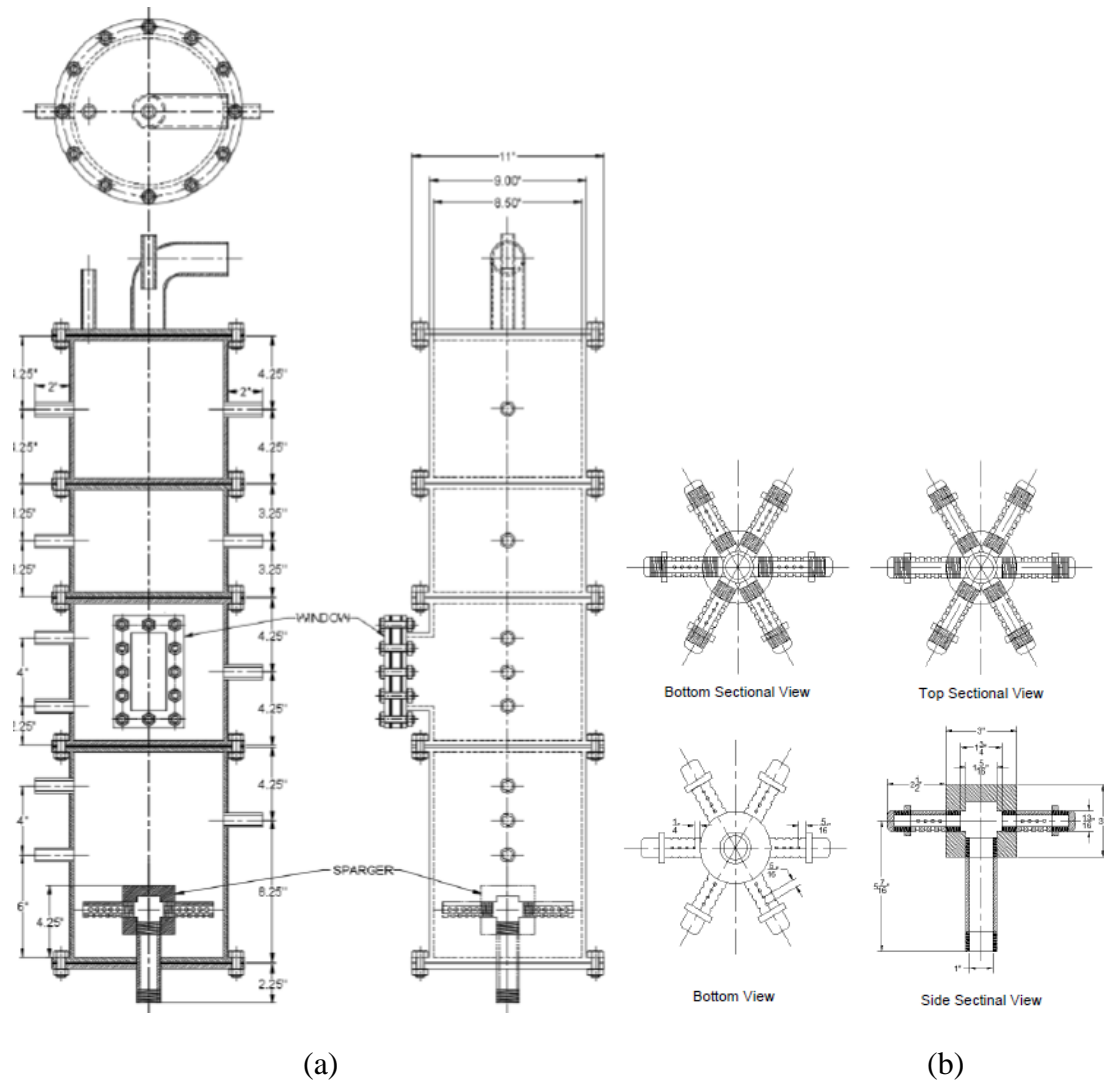


Figure. 3. 1 Abdulrahman [4] (a) SBCR design and (b) Sparger design

Initially the reactor and sparger designs were recreated using Inventor Professional.

However, in order to reduce computational costs, the designs were simplified. First the sparger head was lowered by 10 cm so that the gas would be released at the base of the reactor. This would mean that the simulated heights (H) would be comparable to the experimental results that are 10cm higher. For example, the reactor heights in the simulations are 35, 45 and 55cm which were compared to the experimental results when the static liquid heights were 45, 55, and 65cm. The model could be further simplified to reduce computational costs. As such the sparger was simplified to a single inlet at the base of the reactor opposed to 72 inlets. The inlet has a diameter of 18cm and is extruded 0.3cm downward. The diameter for the gas inlet was selected to represent the bubble distribution

at the base of the experimental reactor. The progression of the design simplification can be viewed in Figure.3.2. The final reactor design can be seen in Figure.3.3 with overall diameter 21.6 cm, gas inlet diameter 18cm extruded 0.3cm downward with varying heights depending on the experiment.

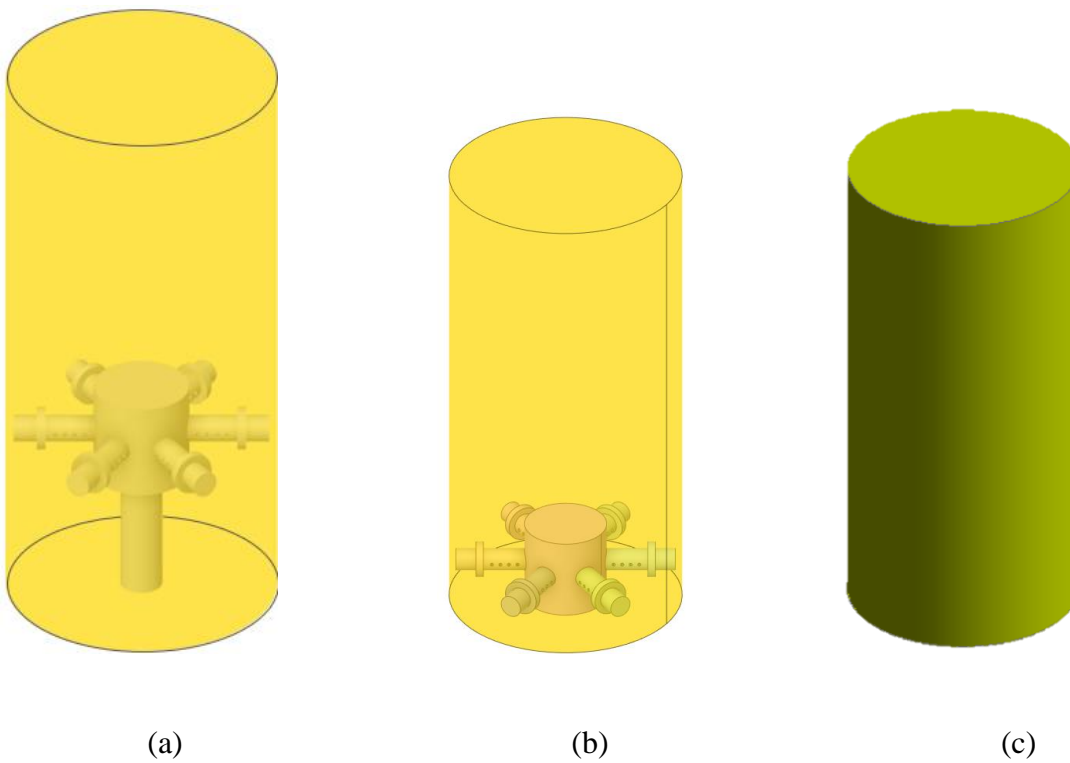


Figure. 3.2 Progression of simplifying the reactor design (a) most complex, (b) more simplified (c) most simple, final design.

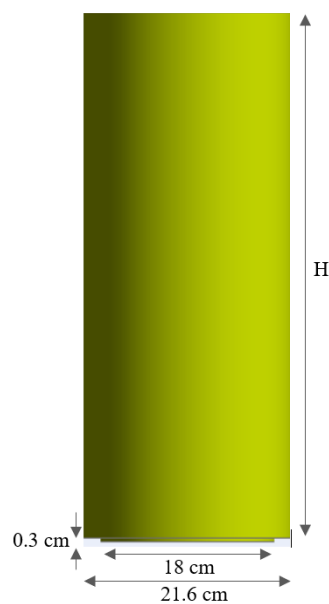


Figure. 3.3 Final SBCR geometry used for simulations.

3.1.2 Operating Conditions

There are three boundaries in the simulated SBCR, the inlet, outlet and the wall conditions. The single inlet boundary condition is set with a specified superficial gas velocity and assumed to have a gas holdup of 1. The gas is incompressible as such there is no specified pressure at the inlet. The outlet pressure is set to atmospheric pressure. A no slip condition is applied to the walls of the reactor for both the liquid and gas phases. The turbulent kinetic energy and dissipation rate at the inlet and outlet were specified using 5,000 iterations as they are difficult to estimate for turbulent models.

3.2 Methods of Multiphase CFD

Multiphase flows can be modeled using two methods, the Euler-Lagrange method and the Euler-Euler method.

3.2.1. Euler – Lagrange Method

In Euler - Lagrange method, the bubbles are considered to be point volume discrete particles which interact with the liquid phase carrying substance. The forces of each particle are considered while calculating the bubble flow by solving the equations of motion. The Eulerian frame of reference is used to solve the equations of motion for the continuous phase (the liquid phase). The continuous phase is solved using the Navier-Stokes equations. While the Lagrangian frame of reference is coupled with Newton's equations of motion and is used to solve for each particle while explicitly tracking the dispersed phase (the gas phase). This results in the Euler- Lagrange model being computationally expensive. Momentum, mass, and energy can be transferred between the dispersed phase and the continuous phase. Better results can be achieved using the Euler-Lagrange method with respect to the Euler-Euler method while simulating dispersed multiphase flows [47] If the volume fraction of the gas phase is significant, this method would be deemed unsuitable.

This is due to the fact that bubble-bubble interactions cannot be ignored in this case. If the gas volume fraction is insignificant, bubble- bubble interactions can be neglected and the simulations will be simpler despite high mass loading being viable ie: ($\dot{m}_{\text{bubbles}} \geq \dot{m}_{\text{slurry}}$).

3.2.2. Euler-Euler Method

In the Euler-Euler method, a new concept is introduced known as the phasic volume fraction. This concept states that the volume of one phase cannot be occupied by another phase and that the summation of all the volume fractions is one. In the Euler-Euler model, gas bubbles are considered to be the dispersed phase [47]. The Eulerian frame of reference is used to solve both the continuous phase and the dispersed phase. The Euler-Euler approach has less computational cost and can produce promising results. The Euler-Euler approach is more favorable in CFD and will be used in this thesis. Table 3.1 shows the comparison between Euler-Lagrange method and Euler-Euler method.

Table 3. 1 Comparison of the Euler-Lagrange Method and the Euler-Euler Method data collected from [47].

Comparison Between the Euler - Lagrange Method and the Euler-Euler Method		
	Euler-Lagrange	Euler-Euler
Bubble analysis	Bubbles are viewed as point volume discrete particles.	Bubbles are classified by the distribution of bubble size in each computational field cell.
Continuous Phase frame of Reference	Eulerian	Eulerian
Dispersed Phase frame of Reference	Lagrangian	Eulerian
Accuracy	More accurate results	Less accurate results
Computational cost	Computationally costly	Less computationally costly

The Euler-Euler method includes three models:

1. The Volume of Fluid (VOF) Model
2. The Mixture Model
3. The Eulerian Model.

3.2.3. Volume of Fluid Model (VOF)

VOF model is a technique used to conduct surface-tracking over a fixed Eulerian mesh. It can be used to study the position of the boundary between two immiscible fluids. The fluids in the VOF method share a single set of momentum equations. Furthermore, the volume fraction for each fluid is tracked in each computational cell domain. There are some limitations associated with the VOF model. VOF models can only be used with a pressure-based solver. The VOF can be used to model a variety of applications which include free-surface flows, filling applications, motion of large bubbles in a liquid, and steady or transient tracking for a liquid-gas interfaces [48].

3.2.4 The Mixture Model

Mixture model can be used for at least two phases. Similar to the Eulerian model the Mixture model does not allow phases to occupy another phase's volume which is also referred to as interpenetrating continua. The dispersed phases are described by solving the momentum, continuity, energy equations for the mixture, the volume fraction, and expressions for the relative velocities. If the model has a homogeneous multiphase flow, then the system can be modeled without the relative velocities. The Mixture model has some limitations, such as; the pressure-based solver must be used, inviscid flow cannot be modeled with the mixture model, and the Discrete Phase Model cannot be used when tracking particles in parallel. The Mixture Model can be used to model applications such as

bubbly flows, cyclone separators, and sedimentation [48].

3.2.5 The Eulerian Model

In Eulerian model, the momentum and continuity equations are solved for each phase. The Eulerian model has some limitations, such as; it is not possible to study a particular phase, in regards to the Reynolds Stress turbulence, the system cannot model inviscid flow, only the particles in the primary phase can be tracked, and the Discrete Phase Model cannot be used when tracking particles in parallel. The Eulerian Model can be used to model applications such as bubble columns, risers, particle suspension and fluidized beds.

Table 3. 2 Identification of the flow type that should be used for each model [48].

Recommended Model for the Varying Flow Types		
Volume of Fluid Model (VOF)	Mixture Model	Eulerian Model
<ul style="list-style-type: none"> • Slug Flow • Stratified/ Free surface Flow 	<ul style="list-style-type: none"> • Bubbly flow (if the dispersed phase volume fraction is above 10%) 	<ul style="list-style-type: none"> • Bubbly flow (if the dispersed phase volume fraction is above 10%)
	<ul style="list-style-type: none"> • Droplet flow (if the dispersed phase volume fraction is above 10%) • Pneumatic transport flow if homogenous flow • Slurry Flow • Hydrotransport 	<ul style="list-style-type: none"> • Droplet flow (if the dispersed phase volume fraction is above 10%) • Pneumatic Transport Flow if granular flow • Fluidized Beds for granular flow • Slurry flow

		<ul style="list-style-type: none"> • Hydrotransport • Sedimentation
--	--	---

Table 3.2 identifies which models should be applied when considering different types of flows. It is important to note that when considering multiple flow regimes in a system, the model selected should reflect the regime that the user is most interested in studying. The different flow regimes will add complexity to the problem and will lower the accuracy in comparison to a system with only one flow regime. As seen in the table above many of the regime flows that can be modeled used in the Mixture model can also be modeled in the Eulerian model. The Mixture Model should be used if [48]:

- The particles have different sizes and larger particles do not dissociate from the main flow.
 - The drag laws are unidentified or do not apply to the system.
 - The problem is simple and does not require a high level of accuracy.
 - Computational costs are more significant than accuracy
- The Eulerian Model should be used if [48]:

- The dispersed phase is clustered in particular regions in the model.
- The accuracy and effect of the drag laws apply to the system. The Schiller-Neumann law can be used when considering spherical particles.
- High accuracy is required which can lead to higher computational costs and potential stability complications.

- Accuracy is more significant than computational costs.

From the above comparison between the Mixture model and the Eulerian model, the Eulerian multiphase model will be used in the CFD simulations of the oxygen bubble column of this thesis. The liquid in this study will be a slurry and will be assumed to be a homogenous slurry due to the small particle size of the solids.

3.3. Eulerian Model Theory

Volume Fraction Equations

The phases in this study will be the slurry liquid phase (continuous phase) and the gas phase (dispersed phase). The Phasic volume fraction previously described can be expressed in terms of the following formulas:

The phase volumes of the gas and slurry are represented by V_g and V_{sl} respectively:

$$V_g = \int_V \alpha_g dV \text{ and } V_{sl} = \int_V \alpha_{sl} dV \quad (3.1)$$

Where α represents the phase holdup and the subscript g and sl represent the gas and slurry phase. The summation of the phase holdup must be equal to 1.

$$\alpha_g + \alpha_{sl} = 1 \quad (3.2)$$

Conservation Equations

Conservation of Mass

The conservation equations assumed for this study are for incompressible Newtonian fluids due to the nature of the flow within the Oxygen SBCR. The conservation of mass equations written in cylindrical coordinates (r, θ, y) are where v is the velocity field [4]:

$$\text{Gas phase: } \nabla \cdot V_g = \frac{\partial v_{r,g}}{\partial r} + \frac{v_{r,g}}{r} + \frac{1}{r} \frac{\partial v_{\theta,g}}{\partial \theta} + \frac{\partial v_{y,g}}{\partial y} = 0 \quad (3.3)$$

$$\text{Slurry phase: } \nabla \cdot V_{sl} = \frac{\partial v_{r,sl}}{\partial r} + \frac{v_{r,sl}}{r} + \frac{1}{r} \frac{\partial v_{\theta,sl}}{\partial \theta} + \frac{\partial v_{y,sl}}{\partial y} = 0 \quad (3.4)$$

Conservation of Momentum

The equations for conservation in cylindrical form is as follows [4]:

r- Direction:

$$\begin{aligned} \rho_g \alpha_g \left(\frac{\partial v_r}{\partial t} + v_r \frac{\partial v_r}{\partial r} + \frac{v_\theta}{r} \frac{\partial v_r}{\partial \theta} + v_y \frac{\partial v_r}{\partial y} - \frac{v_\theta^2}{r} \right) &= -\alpha_g \frac{\partial P}{\partial r} + \alpha_g \frac{\mu_{g,eff}}{3} \frac{\partial(\nabla \cdot V)}{\partial r} + \\ \mu_{g,eff} \alpha_g \left[\frac{1}{r} \frac{\partial}{\partial r} \left(r \frac{\partial v_r}{\partial r} \right) + \frac{1}{r^2} \frac{\partial^2 v_r}{\partial \theta^2} + \frac{\partial^2 v_r}{\partial y^2} - \frac{v_r}{r^2} - \frac{2}{r^2} \frac{\partial v_\theta}{\partial \theta} \right] &+ \rho_g \alpha_g g_r + M_{i,g,r} \end{aligned} \quad (3.5)$$

θ -direction:

$$\begin{aligned} \rho_g \alpha_g \left(\frac{\partial v_\theta}{\partial t} + v_r \frac{\partial v_\theta}{\partial r} + \frac{v_\theta}{r} \frac{\partial v_\theta}{\partial \theta} + v_y \frac{\partial v_\theta}{\partial y} + \frac{v_r v_\theta}{r} \right) &= -\alpha_g \frac{1}{r} \frac{\partial P}{\partial \theta} + \alpha_g \frac{\mu_{g,eff}}{3r} \frac{\partial(\nabla \cdot V)}{\partial \theta} + \\ \alpha_g \mu_{g,eff} \left[\frac{1}{r} \frac{\partial}{\partial r} \left(r \frac{\partial v_\theta}{\partial r} \right) + \frac{1}{r^2} \frac{\partial^2 v_\theta}{\partial \theta^2} + \frac{\partial^2 v_\theta}{\partial y^2} + \frac{2}{r^2} \frac{\partial v_r}{\partial \theta} - \frac{v_\theta}{r^2} \right] &+ \rho_g \alpha_g g_\theta + M_{i,g,\theta} \end{aligned} \quad (3.6)$$

y-direction:

$$\begin{aligned} \rho_g \alpha_g \left(\frac{\partial v_y}{\partial t} + v_r \frac{\partial v_y}{\partial r} + \frac{v_\theta}{r} \frac{\partial v_y}{\partial \theta} + v_y \frac{\partial v_y}{\partial y} \right) &= -\alpha_g \frac{\partial P}{\partial y} + \alpha_g \mu_{g,eff} \left[\frac{1}{r} \frac{\partial}{\partial r} \left(r \frac{\partial v_y}{\partial r} \right) + \frac{1}{r^2} \frac{\partial^2 v_y}{\partial \theta^2} + \right. \\ \left. \frac{\partial^2 v_y}{\partial y^2} \right] &+ \rho_g \alpha_g g_y + M_{i,g,y} \end{aligned} \quad (3.7)$$

Where P is the shared phase pressure, μ_{eff} is the effective viscosity, g is the gravitational acceleration and Mi is the total interfacial forces between the phases.

Conservation of energy

The equations for conservation of energy in cylindrical form is [4]:

$$\alpha_g \rho_g C \left(\frac{\partial T_g}{\partial t} + v_{r,g} \frac{\partial T_g}{\partial r} + \frac{v_{\theta,g}}{r} \frac{\partial T_g}{\partial \theta} + v_{y,g} \frac{\partial T_g}{\partial y} \right) = \bar{\tau}_g : \nabla V_g + k_g \left(\frac{1}{r} \frac{\partial}{\partial r} \left(r \frac{\partial T_g}{\partial r} \right) + \frac{1}{r^2} \frac{\partial^2 T_g}{\partial \theta^2} + \frac{\partial^2 T_g}{\partial y^2} \right) + S_g + Q_{g,sl} \quad (3.8)$$

$$\alpha_{sl} \rho_{sl} C \left(\frac{\partial T_{sl}}{\partial t} + v_{r,sl} \frac{\partial T_{sl}}{\partial r} + \frac{v_{\theta,sl}}{r} \frac{\partial T_{sl}}{\partial \theta} + v_{y,sl} \frac{\partial T_{sl}}{\partial y} \right) = \bar{\tau}_{sl} : \nabla V_{sl} + k_{sl} \left(\frac{1}{r} \frac{\partial}{\partial r} \left(r \frac{\partial T_{sl}}{\partial r} \right) + \frac{1}{r^2} \frac{\partial^2 T_{sl}}{\partial \theta^2} + \frac{\partial^2 T_{sl}}{\partial y^2} \right) + S_{sl} + Q_{sl,g} \quad (3.9)$$

Where $\bar{\tau} : \nabla V$ is the viscous stress tensor contracted with the velocity gradient, $Q_{g,sl}$ is the intensity of heat exchange between the gas and slurry phases, k is thermal conductivity, C is the specific heat.

Drag coefficient (C_D)

The drag coefficient is a critical element in a SBCR when discussing the hydrodynamics. However, deriving an empirical, reliable drag coefficient is challenging as it requires certain conditions. These conditions include measuring the force on a single bubble moving the terminal rise velocity in a stagnant liquid without impurities. Although there are numerous drag correlations the most accepted model is the Schiller Naumann drag model for fluid-fluid systems which will be used for this thesis [48]

$$C_D = \frac{24(1+0.15 Re_b^{0.687})}{Re_b} \text{ for } Re_b \leq 1000$$

or

$$C_D = 0.44 \text{ for } Re_b > 1000 \quad (3.10)$$

Where Re is the relative Reynolds number.

Reynolds number

$$Re_l = \frac{\rho_l U_{gs} D_R}{\mu_l} \quad (3.11)$$

Where ρ_l is the density of the liquid, U_{gs} is the gas velocity, D_R is the diameter of the SBCR and μ_l is the fluid viscosity. In this study the lowest Reynolds number was calculated to be 1.1×10^4 and the highest Reynolds number was 3.1×10^4 .

The lift force is an important element of SBCR. However, the lift force was neglected in this study. Sokolichin et al. [49] stated that good comparison can be made without the lift force if the experimental lift force direction and magnitude are unknown.

Interfacial area concentration

The interfacial area concentration is a key parameter when studying the interfaces between the phases as it is used to estimate the mass, momentum and energy transfer. The interfacial area concentration is the interfacial area between two phases per unit mixture volume. In an Eulerian multiphase model the interfacial area can be calculated using the symmetric model. The interfacial area of concentration in the symmetric model will approach 0 as the gas holdup (α_g) gets closer to 1.

$$A_i = \frac{6\alpha_g(1-\alpha_g)}{d_b} \quad (3.12)$$

Where d_b is the bubble diameter. The Sauter-mean bubble diameter was used to allow for the mass, momentum and heat transfer across the phases to be considered. The Sauter-mean diameter is the diameter of a sphere that has the same volume/surface area ratio as a particle of interest. The Hibiki-Ishii Model was used for the coalescence and the breakage models. This model takes into account coalescence due to entering wakes, and random collisions, as well as, breakage caused by the impact of turbulent eddies [48].

Ranz marshal

The heat transfer correlation used to determine the Nusselt number (Nu_g) in this study's simulations was the Ranz Marshal model. The following formula is used to calculate the Nusselt number:

$$Nu_g = 2 + 0.6 Re_b^{1/2} Pr^{1/2} \quad (3.13)$$

Where Re_b is the relative Reynolds number dependent on the gas bubble diameter and relative velocity of the gas to the slurry phase $|v_g - v_{sl}|$. Pr is the Prandtl number of the slurry and can be calculated by:

$$Pr = \frac{c_{p,sl} \mu_{sl}}{k_{sl}} \quad (3.14)$$

3.4 Turbulence Model

Turbulence is a random, unsteady motion that occurs in fluids with Reynolds numbers varying from mild to high. The Reynolds-Averaged Navier-Stokes (RANS) models, such as k- ϵ and k- ω , are the least computationally expensive approaches for estimating complex turbulent flows. They are capable of simulating a broad variety of turbulent flows and heat transfer processes with an acceptable accuracy. They solve two distinct transport equations to determine the turbulence's velocity and length scales. The standard k- ϵ model is only applicable for a completely turbulent flow because this model was established on the assumption that the flow is entirely turbulent (based on the calculated Reynolds number) and that molecular viscosity has an insignificant influence [48]. The RNG k- ϵ is similar to the standard k- ϵ model however, for a larger range of flows the RNG k- ϵ it is more accurate and reliable. There are several reasons that the RNG k- ϵ model is more accurate which include the fact that [48]

- The ϵ equation has additional terms to improve the rapidly strained flows accuracy.
- The RNG model includes the effects of swirl which improves the accuracy.
- The RNG model's Prandtl numbers are provided using an analytical formula, opposed to the standard k- ϵ model, which has constant user specified values.

The k- ω model works better for low Reynolds number flows, although the solution is very sensitive to the values of k and ω outside the shear layer. Therefore, it is not recommended to use the conventional k- ω model [48]. The RNG k- ϵ model was selected for this study as the flow regime will be a churn turbulent flow, which is best simulated with the RNG k- ϵ model.

K- ϵ Sub Models

The k- ϵ model includes three sub models [48]:

1. The mixture turbulence model
2. The dispersed turbulence model
3. The per-phase turbulence model

The mixture turbulence model is used in a stratified multiphase flow with separable phases and equivalent densities of the phases. In many cases, it is sufficient to utilize the mixture's properties and velocities to capture significant elements of the turbulent flow [48].

The dispersed turbulence model is best used when secondary phase concentrations are low or the granular model is used. It may be used when there is a distinct primary phase and a number of dispersed secondary phases [48].

The per-phase disperse model is the most generic model where the transport equations

are solved for each phase in a multiphase turbulence model. When the transfer of turbulence across phases is of significance, this turbulence model should be used. The per-phase turbulence model is computationally more costly than the dispersed turbulence model because of solving two extra transport equations for each secondary phase [48].

In this study the dispersed turbulence model is used as it is less computationally expensive than the per-phase turbulence model. Additionally, the mixture turbulence model could not be used due to the significant difference in the phase densities.

Wall function

There are three selections for the k-ε turbulence model, the standard wall function, non-equilibrium wall functions and the enhanced wall functions. For industrial flows the standard wall function is prominently used. The standard wall function provides reasonable results for a variety of wall bounded flows [48]. The standard wall functions were used in this study.

The law of the wall for the mean velocity yields for the standard wall function are:

$$U^* = \frac{1}{k} \ln(Ey^*) \quad (3.15)$$

Where U^* is the dimensionless velocity which is calculated using:

$$U^* = \frac{U_P C_\mu^{1/4} k_P^{1/2}}{\tau_w / \rho} \quad (3.16)$$

Where y^* is the dimensionless distance from the wall:

$$y^* = \frac{\rho C_\mu^{1/4} k_P^{1/2} y_P}{\mu} \quad (3.17)$$

Where k is the Von Karman constant (0.4187), E is the empirical constant (9.793), U_P

is the mean velocity of the fluid near wall-node P, k_p is the turbulence kinetic energy at the near wall node P, y_p is the distance from point P to the wall and μ is the dynamic viscosity of the fluid.

3.5 Model Summary

The model selected to simulate the SBCR was the Euler-Euler method, with an Eulerian model and the dispersed, RNG k- ϵ turbulence model. The model included the interfacial area concentration which took into account the Hibiki-Ishii model for bubble breakage and coalescence using the saunter mean diameter. The drag coefficient was also considered, the heat transfer correction was incorporated by using the Ranz Marshal model and a standard wall function was considered. These models were selected for their accuracy and ability to reduce computational expenses.

3.6 Material Properties

The experiment carried out by Abdulrahman [4] was conducted on a Water-Helium-Alumina system due to challenges associated with the Cuprous Chloride (CuCl) and Oxygen (O₂) materials. The challenges include: the difficulties in viewing O₂ bubbles in melted CuCl due to its dark colors, the corrosiveness of the CuCl molten salt, and the O₂ gas ability to oxidize many materials to accelerate its combustion [4,50-51]. Based on Buckingham pi theorem a dimensional analysis was conducted which identified liquid water at 22°C and Helium gas at 90°C to be suitable alternatives to molten CuCl at 530°C and oxygen gas at 600°C [4,50-51].

A critical step of the study is identifying key independent parameters that will affect the gas holdup (α_g). Key independent parameters related to the material include density,

viscosity, and surface tension. Key parameters related to the reactor geometry include, reactor height, reactor diameter, sparger geometry, and superficial gas velocity.

$$\alpha_g = f(\rho_l, \rho_g, \mu_l, \mu_g, \sigma, U_{gs}, D_R, H_R, d_o), \quad (3.18)$$

Where α_g is the gas holdup, ρ is the density, μ_l is the dynamic viscosity, σ is the surface tension, U_{gs} is the superficial gas velocity, D_R is the reactor diameter, H_R is the reactor height, and d_o is the inlet diameter. The subscript l denotes liquid and the subscript g denotes gas.

3.6.1 Gas Phase Properties

The gas physical properties for O₂ and He were taken from Lemmon and Jaconsen [52], Borgnakke and Sonntag [53] and Petersen [54] and are summarized in Table 3.3 below.

Table 3. 3 Physical properties of gas material [52-54].

Gas Physical Property	Unit	Oxygen (O₂)	Helium (He)
Temperature (T)	°C	600	90
Temperature (T)	K	873	363
Density (ρ)	kg/m ³	0.4467	0.1344
Specific Heat (C_p)	J/kg K	1071.9	5193
Thermal Conductivity (k)	W/m K	0.0645	0.1687
Dynamic Viscosity (μ)	kg/m s	4.45E-05	2.267E-05
Molecular Weight	kg/ kmol	31.9988	4.0026

3.6.2 Liquid Phase Properties

The liquid properties for molten CuCl and H₂O were taken from Zamfirescu et al. [55], Lemmon and Jaconbsen [52], Borgnakke and Sonntag [53] and Petersen [54] and are summarized in Table 3.4 below.

Table 3. 4 Physical properties of liquid material [52-55].

Liquid Physical Property	Unit	Cuprous Chloride (CuCl)	Water (H₂O)
Temperature (T)	°C	530	22
Temperature (T)	K	803	295
Density (ρ)	kg/m ³	3692	998.2
Specific Heat (C_p)	J/kg K	650.85	4182
Thermal Conductivity (k)	W/m K	0.2	0.6
Dynamic Viscosity (μ)	kg/m s	0.002045	0.000975
Molecular Weight	kg/ kmol	98.99	18.0152
Standard State Enthalpy	J/ kg mol	-1.372E+8	-2.858e+8
Surface Tension (σ)	N/m	0.0867	0.0724

3.6.3 Solid Phase Properties

Since the material simulations studies carried out by Abdulrahman [4] included only the liquid and gas phases, the only solid phase properties that are calculated in this thesis are for Alumina (Al₂O₃).

Density

The density of solid alumina (Al_2O_3) varies with absolute temperature according to Auerkari [56] is:

$$\rho_{\text{Al}_2\text{O}_3} = 4136 e^{4.153 \times 10^{-4} - 3.107 \times 10^{-5} T + 1.082 \times 10^{-7} T^2} \quad (3.19)$$

Where T is in Kelvin.

Specific Heat

The specific heat of solid alumina varies with absolute temperature within the range of 25-1500 °C according to [56]:

$$C_p = 1.045 + 1.742 \times 10^{-4} T - \frac{2.796 \times 10^{-4}}{T^2} \quad (3.20)$$

Where C_p is in kJ/kg.K and T is in Kelvin.

Thermal Conductivity

The thermal conductivity of solid alumina varies with temperature in the range of 25-1300 °C according to [56] is:

$$k = 5.5 + 34.5 e^{-0.003 T} \quad (3.21)$$

Where k is in W/m.K and T is in °C.

Table 3.5 below summarizes the solid particle properties of Alumina calculated from the formulas 3.2-3.4.

Table 3. 5 Solid Alumina properties bases on Auerkari [56] formulas.

Solid Physical Property	Unit	Alumina (Al_2O_3)
Temperature (T)	°C	22

Temperature (T)	K	295
Density (ρ)	kg/m ³	4138.75
Specific Heat (C_p)	J/kg K	0.7751
Thermal Conductivity (k)	W/m K	37.7965
Molecular Weight	kg/ kmol	101.96

3.6.4 Slurry Phase Properties

The slurry is assumed to be a homogeneous mixture of the solid particles and the liquid phase material. The solid particle concentrations (C_s) that are studied in this thesis are $C_s = 0\%$, $C_s = 5\%$ and $C_s = 10\%$. Each slurry concentration will have different densities, specific heat, thermal conductivity, dynamic viscosity and molecular weight. The properties are calculated based on the following.

Density

The slurry's average density (ρ_{sl}) can be calculated by:

$$\rho_{sl} = \rho_s C_s + \rho_l (1 - C_s) \quad (3.22)$$

Where ρ_s is the density of the solid particles and ρ_l is the density of the liquid phase and C_s is the volume fraction of the solid particles.

$$C_s = \frac{V_s}{V_{sl}} \quad (3.23)$$

Where V_s is the volume of the solid particles and V_{sl} is the volume of the slurry.

Specific Heat

The slurry's average specific heat can be calculated by

$$C_{p,sl} = \rho_s C_{p,s} C_s + \rho_l C_{p,l} (1 - C_s) \rho_{sl} \quad (3.24)$$

Where $C_{p,s}$ is the specific heat of the solid phase and $C_{p,l}$ is the specific heat of the liquid phase.

Thermal Conductivity

According to Boomsma and Poulikakaos [57] the effective thermal conductivity (k_{sl}) can be calculated by the following formula

$$k_{sl} = k_s C_s + k_l (1 - C_s) \quad (3.25)$$

Where k_s is the thermal conductivity of the solid phase and k_l is the thermal conductivity of the liquid phase.

Dynamic Viscosity

The Slurry's dynamic viscosity (μ_{sl}) can be related to the viscosity of the liquid phase

$$\mu_{sl} = \mu_r \mu_l \quad (3.26)$$

Where μ_l is the dynamic viscosity of the liquid. μ_r is the dimensionless relative dynamic viscosity which varies based on the size of the particles and solid particle concentration. μ_r for higher solid particle concentrations (such as in the case of this study) can be calculated using the proposed modification by Guth and Simba [58]. This equation incorporates the solid particle interactions with each other.

$$\mu_r = 1 + 2.5 C_s + 14.1 C_s^2 \quad (3.27)$$

Where C_s is the volume fraction of the solid particles.

3.6.5 Material Property Summary

Based on the calculations and formulas presented above (Eqs. (3.22-3.27)), Tables 3.6 and 3.7 summarize the properties of the Water-Helium-Alumina System (Table 3.6) and the Cupreous Chloride-Oxygen System (Table 3.7).

Table 3. 6 Material properties for the Water-Helium- Alumina systems for concentrations $C_s=0\%$, $C_s=5\%$ and $C_s=10\%$.

Physical Property	Unit	Gas Phase (He)	Solid Phase (Al₂O₃)	Liquid Phase (H₂O) C_s=0%	Slurry C_s=5%	Slurry C_s=10%
Temperature (T)	°C	90	22	22	22	22
Temperature (T)	K	363	295	295	295	295
Density (ρ)	kg/m ³	0.1344	4138.75	998.2	1155.23	1312.26
Specific Heat (C_p)	J/kg K	5193	0.7751	4182	3433.01	2863.27
Thermal Conductivity (k)	W/m K	0.1687	37.7965	0.6	2.4598	4.3197
Dynamic Viscosity (μ)	kg/m s	2.267E-5	-	0.000975	0.001131	0.001356
Molecular Weight	kg/ kmol	4.0026	101.96	18.0152	22.2124	26.4097
Standard State Enthalpy	J/ kg mol	-	-	-2.858e+8	-2.858E+08	-2.858E+08
Surface Tension (σ)	N/m	-	-	0.0724	0.0724	0.0724

Table 3. 7 Material properties for the Cuprous-Chloride systems for concentrations $C_s=0\%$.

Physical Property	Unit	Gas Phase (O₂)	Liquid Phase (CuCl) C_s=0%
Temperature (T)	°C	600	530

Temperature (T)	K	873	803
Density (ρ)	kg/m ³	0.4467	3692
Specific Heat (C_p)	J/kg K	1071.9	650.85
Thermal Conductivity (k)	W/m K	0.0645	0.2
Dynamic Viscosity (μ)	kg/m s	4.45E-05	0.002045
Molecular Weight	kg/ kmol	31.9988	98.99
Standard State Enthalpy	J/ kg mol	-	-1.372E+8
Surface Tension (σ)	N/m	-	0.0867

3.7 CFD Model Validation

3.7.1 ANSYS Fluent Setup

The software used to simulate the 3D SBCR was ANSYS 2021 R1. The student version has some limitations which may affect the study. The student software limits the Fluid Physics to 512,000 cells/ nodes [48]. The largest oxygen reactor geometry simulated has a diameter of 21.6 cm and a height of 55cm. A hexahedron mesh was used for the SBCR. The Mesh independence was conducted to ensure the largest mesh size to minimize the computational expenses while achieving acceptable results was selected. The final mesh was composed of 26,825 nodes and 24,396 elements. This led to a 3% difference in the gas holdup which is acceptable as it was as far less computationally expensive.

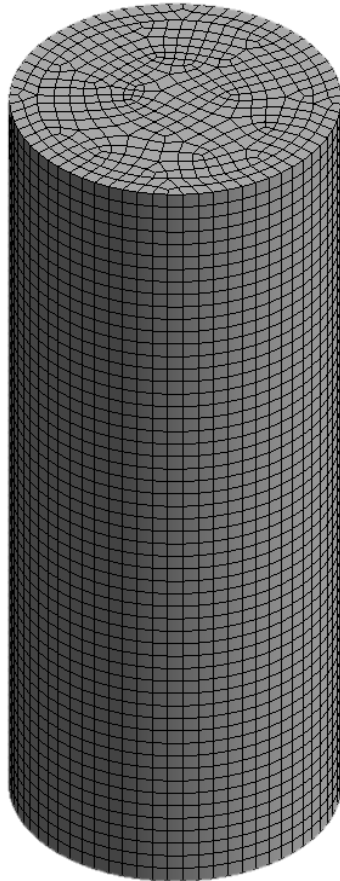


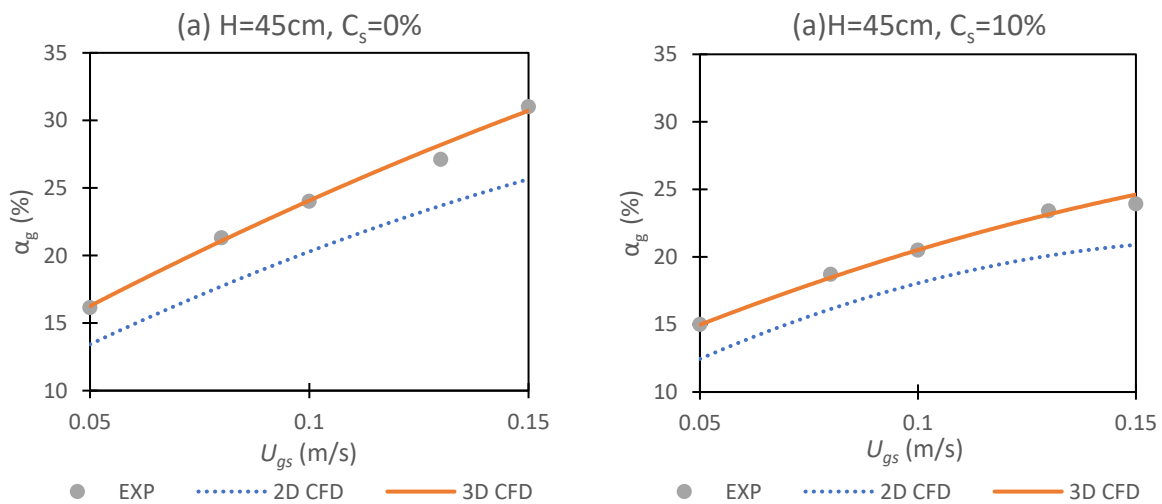
Figure. 3.4 SBCR hexahedron mesh.

3.7.2 Comparison of the Gas Holdup of the Helium-Water-Alumina 3D CFD Simulations with 2D CFD Simulations and Experimental Data

The gas holdup data of the 3D-CFD Helium-Water-Alumina SBC simulations were validated against experimental data conducted by Abdulrahman [4] and compared to 2D simulations conducted by Abdulrahman [4]. The effects of static liquid height, solid concentration, and superficial gas velocity on the gas holdup were compared. It can be noted that the majority of the gas holdup results from the simulations were overpredicted. The 3D simulations for the Helium-Water-Alumina had a maximum relative error less than 8.4%. This is a significant improvement over the 2D-CFD simulations which had at most a maximum relative error of less than 28.5% and the majority of the gas holdup results were underpredicted [4]. Potential methods to reduce the relative error is to decrease the mesh size. Decreasing the mesh size will allow the software to take into consideration small

vortical structures in the flow such as eddies [59]. The mesh size that is used in this study is selected to reduce the computational cost.

Figures. 3.5- 3.6 demonstrate the 3D-CFD models' ability to predict the gas holdup (α_g) at different superficial gas velocities (U_{gs}), different static liquid heights (H) and solid particle concentrations (C_s). The theoretical 3D-CFD models are able to predict the experimental data fairly well. It is noticed that the CFD simulations are better at predicting the simulation with lower solid particle concentrations. The maximum relative percent error is found to be at $C_s = 10\%$ with an error of 8.37%, followed by $C_s = 5\%$ with a maximum error of 6.35%, and lastly $C_s = 0\%$ with a maximum percent error of 5.36%.



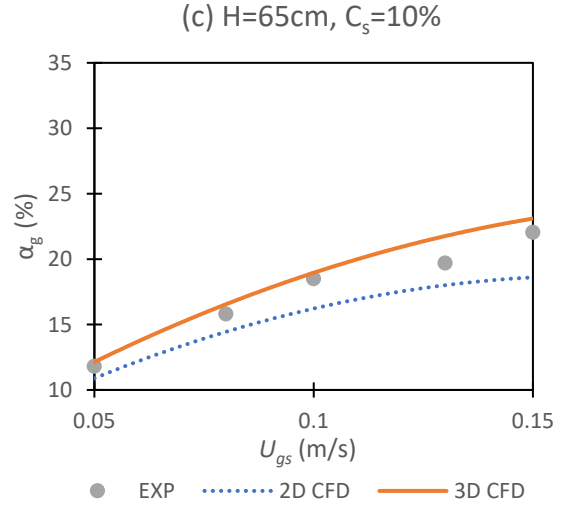
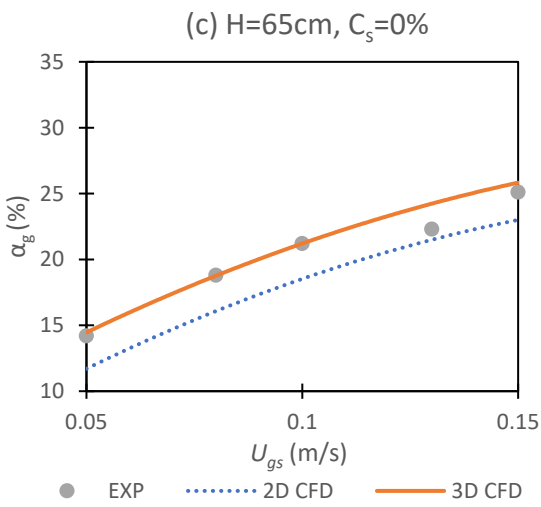
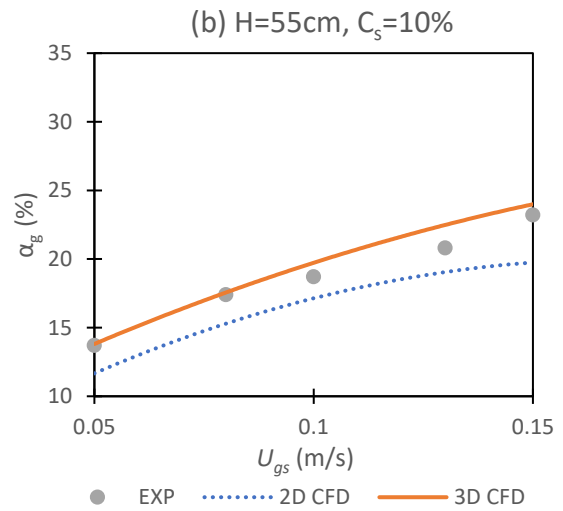
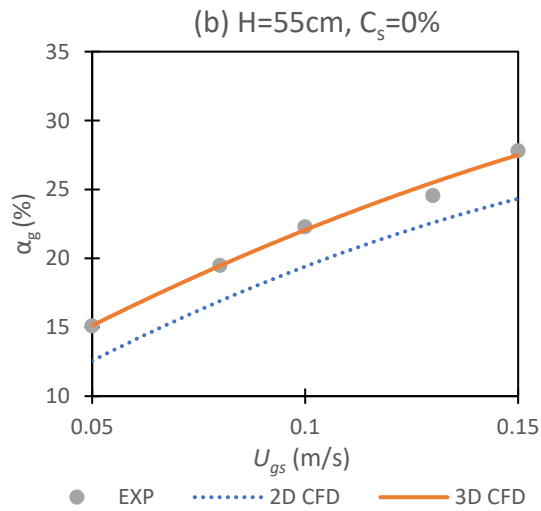
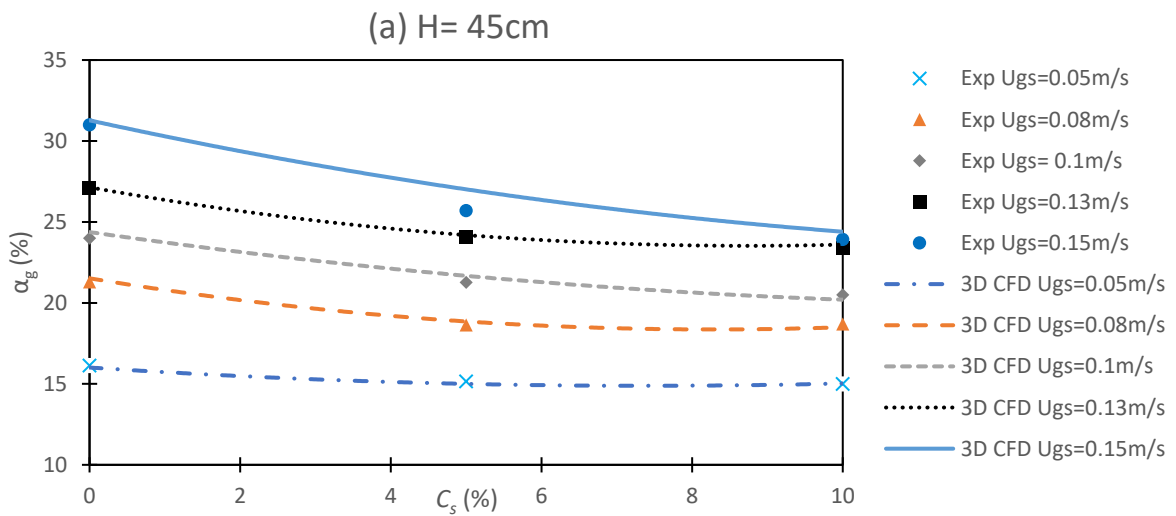


Figure 3.5 Comparison of Average Gas Holdup Versus Superficial Gas Velocity between 2D, 3D and Experimental Results at a Solid Particle Concentration of 0% for (a) $H=45$ (b) $H=55$ (c) $H=65\text{cm}$.

Figure 3.6 Comparison of Average Gas Holdup Versus Superficial Gas Velocity between 2D, 3D and Experimental Results at a Solid Particle Concentration of 10% for (a) $H=45$ (b) $H=55$ (c) $H=65\text{cm}$.



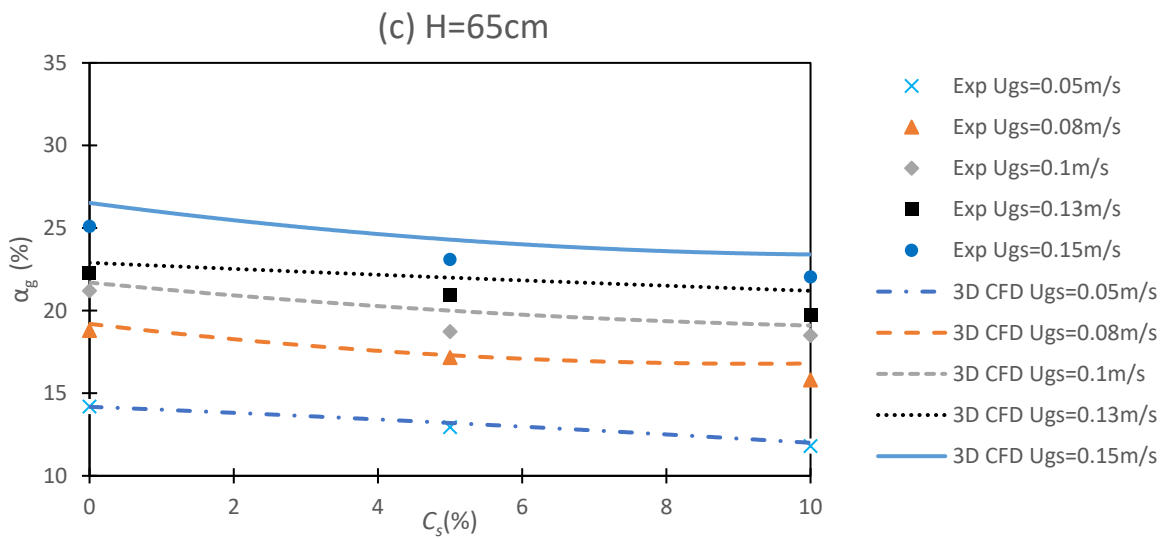
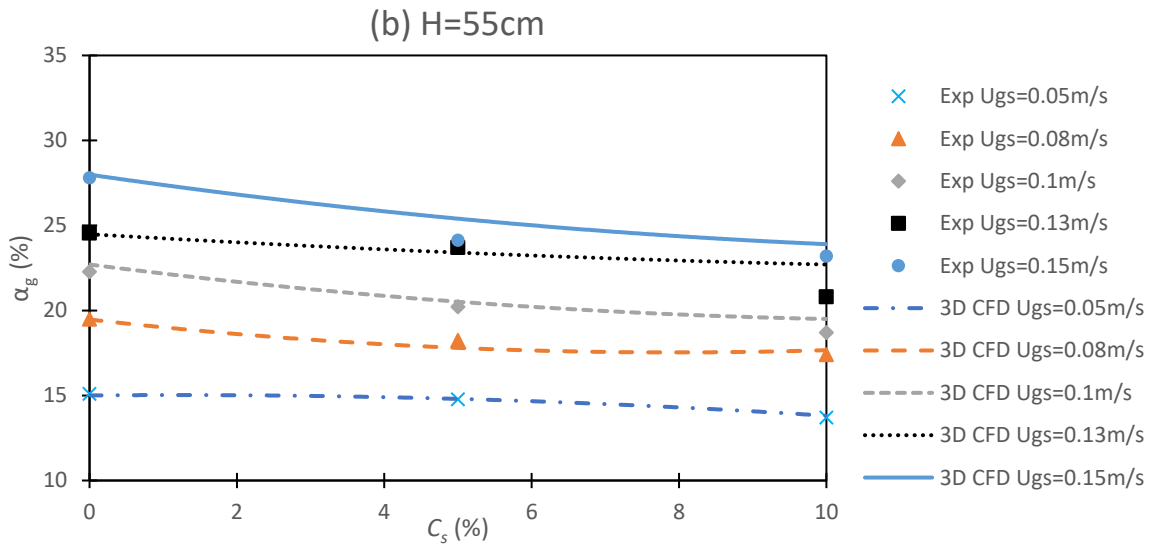
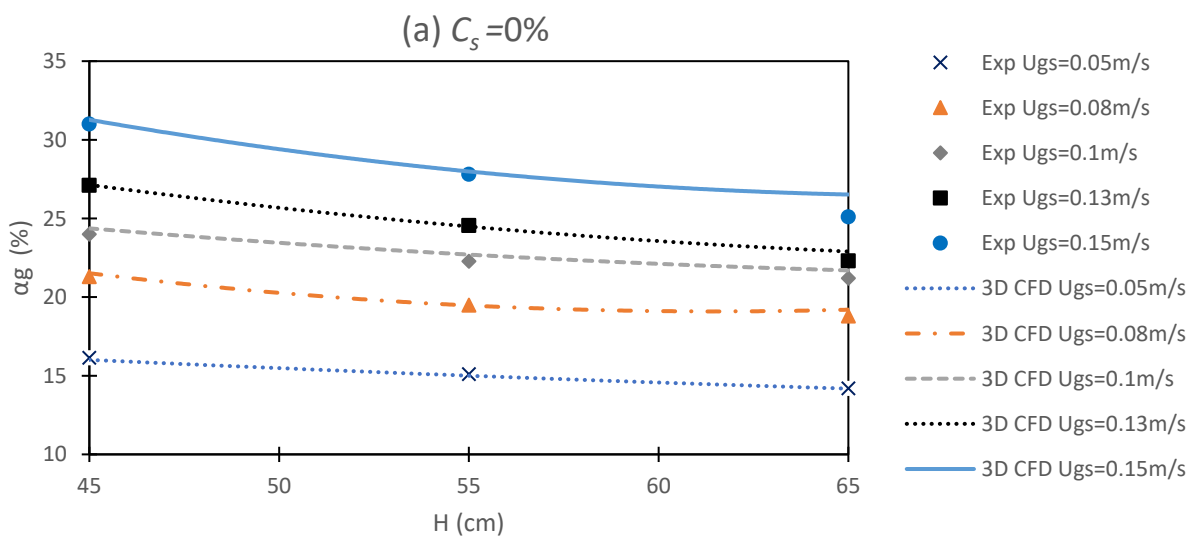


Figure. 3.7 Comparison Between 3D CFD and Experimental Data for the Helium-Water- Alumina system, Gas Holdup Versus the Solid Particle Concentration at Different Static Liquid Heights (a) H=45 (b) H=55 (c) H=65cm.



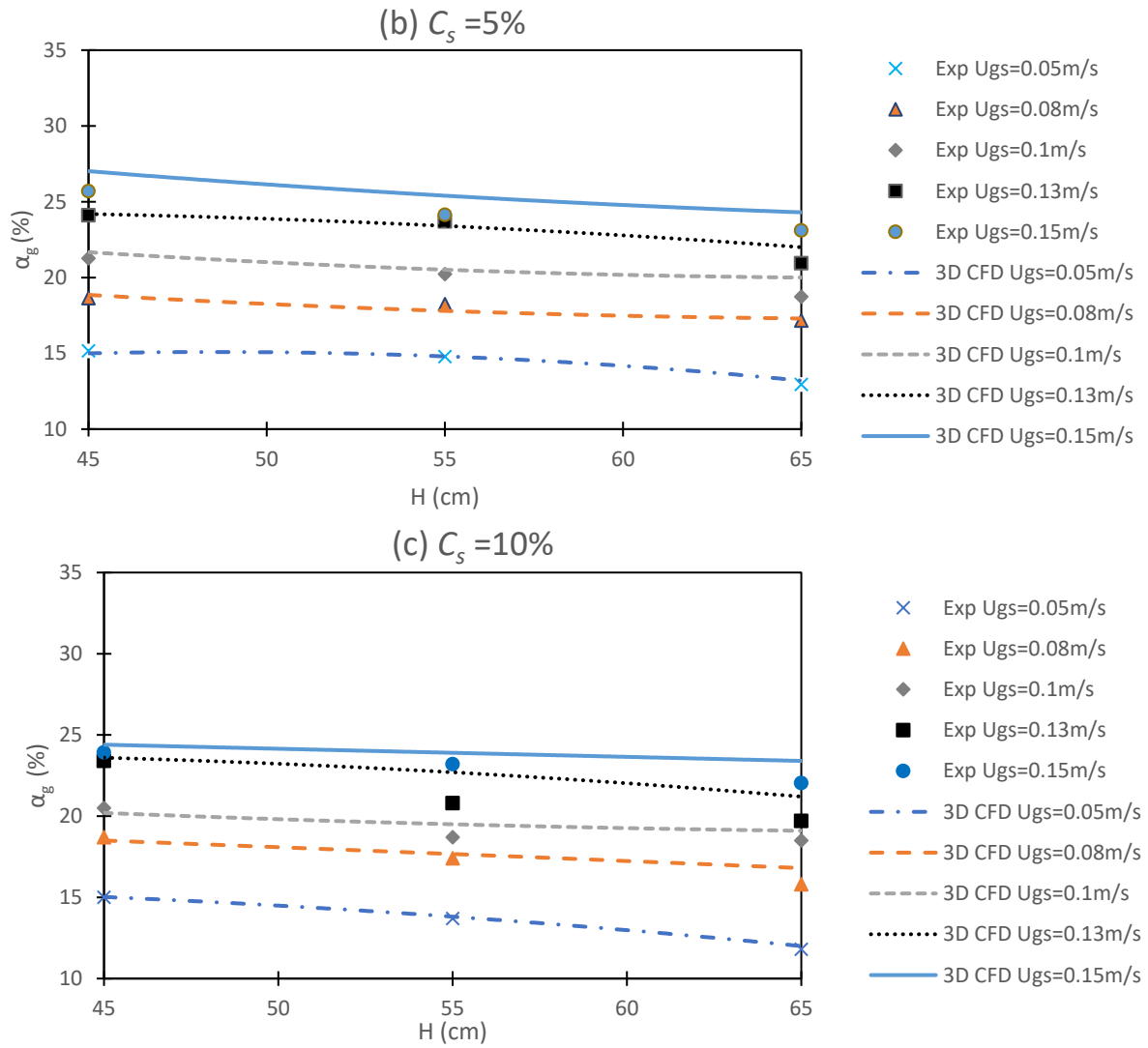


Figure 3. 8 Comparison Between 3D CFD and Experimental Gas Holdup Versus the Static Liquid Height at Different Superficial Velocities for (a) $C_s=0\%$, (b) $C_s=5\%$, (c) $C_s=10\%$.

Chapter 4

Results and Discussion

4.1. Introduction

In this chapter, the results obtained by the 3D CFD simulations for the SBCR are presented. The 3D CFD simulations were conducted for the Helium-Water-Alumina System and for an Oxygen-Cuprous Chloride System. Both systems were investigated to ascertain the effect of varying the superficial gas velocity (U_{gs}), static liquid height (H), and the solid particle concentration (C_s) on the Gas holdup (α_g) of the system. Additionally, the Helium-Water-Alumina System results were compared to previous experimental data and 2D CFD simulated data.

4.2. Gas Holdup Results for the Helium-Water-Alumina System

4.2.1. Effects of Superficial Gas Velocity (U_{gs}) on Gas Holdup (α_g)

Figure. 4.1 shows the three-dimensional curves of the gas holdup versus U_{gs} and H for different C_s . Figure. 4.2 shows the three-dimensional curves of the gas holdup versus U_{gs} and C_s for different H . Figure. 4.3 and 4.4 depict the effects of varying the superficial gas velocity (U_{gs}) on the average gas holdup (α_g) while varying the static liquid height (H) and the solid particle concentration (C_s) for a helium-water-alumina system. From the figures, it can be observed that increasing U_{gs} leads to a higher α_g for different H and C_s . Figure. 4.5-4.8 show the contours of the cut sections of the SBCR taken in the center of the XY, and ZY planes. Additional cut sections are taken at various heights on the ZX plane within the reactor at heights 10, 20 and 30 cm from the base of the reactor to allow for a more detailed contours of α_g . It is clear from the contours that the gas holdup is not symmetrical on the XY, ZY and the ZX planes demonstrating that the behavior of the gas holdup is strongly three dimensional. It is observed that α_g increases when U_{gs} increases. For $C_s=0\%$ and H of 45cm a 95% increase in the gas

holdup was noticed when increasing the velocity from 0.05m/s to 0.15m/s. This is because a larger number of bubbles are formed with the increased gas velocity. Larger bubbles can then be formed due to coalescence which results in an increase in gas holdup. Additionally, a pressure drop in the bed of the reactor occurs due to a decrease in the hydrostatic pressure. The higher the gas flow rate the lower the hydrostatic pressure which further decrease the bed pressure and increases α_g [4].

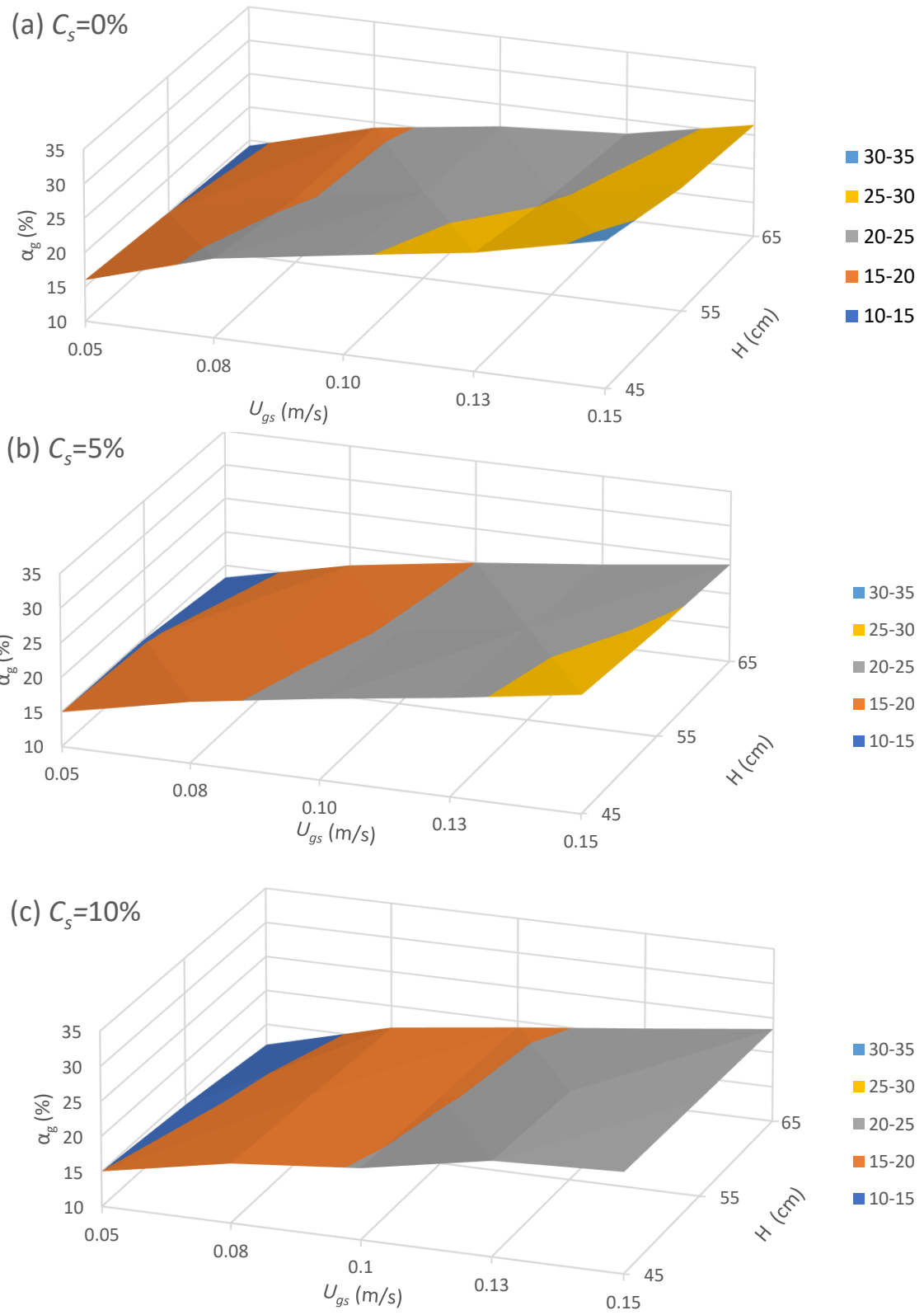


Figure. 4. 1 Average Gas Holdup Versus Superficial Gas Velocity and Static Liquid Height of Helium-Water-Alumina at (a) $C_s=0\%$, (b) $C_s=5\%$, (c) $C_s=10\%$.

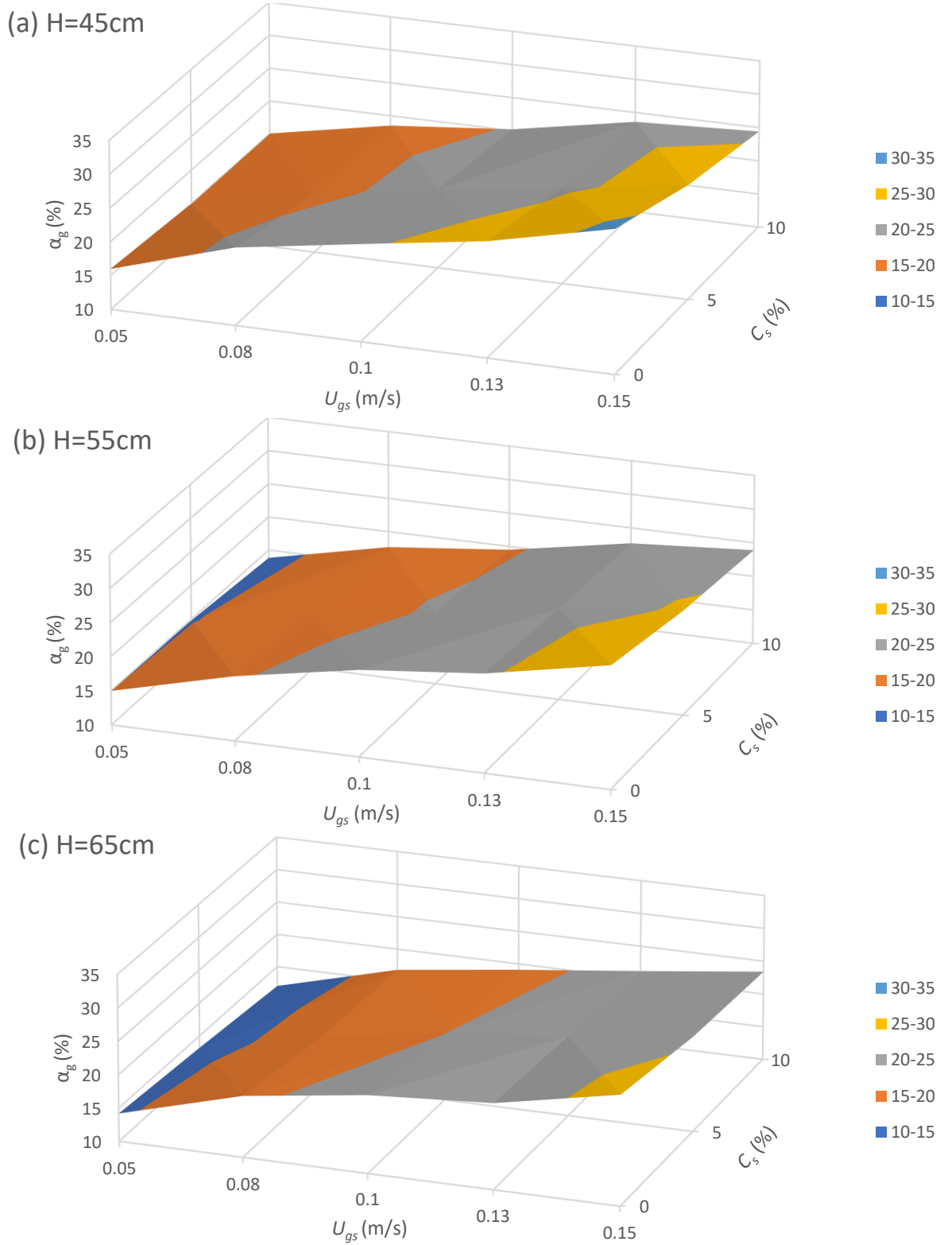


Fig. 4. 2 Average Gas Holdup Versus Superficial Gas Velocity and Solid Particle Concentration of Helium- Water-Alumina For (a) H=45cm, (b) H=55, (c) H=65.

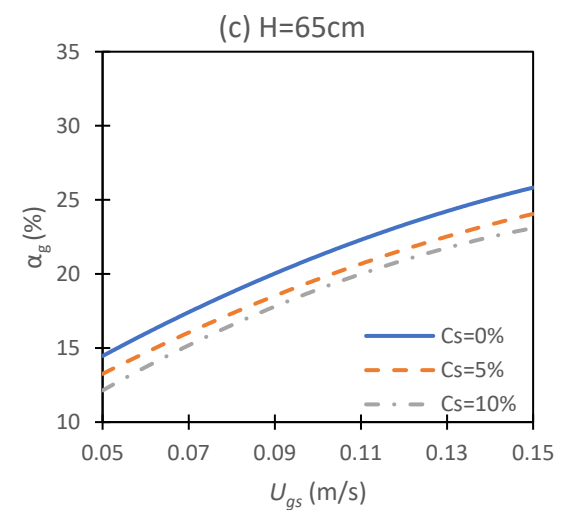
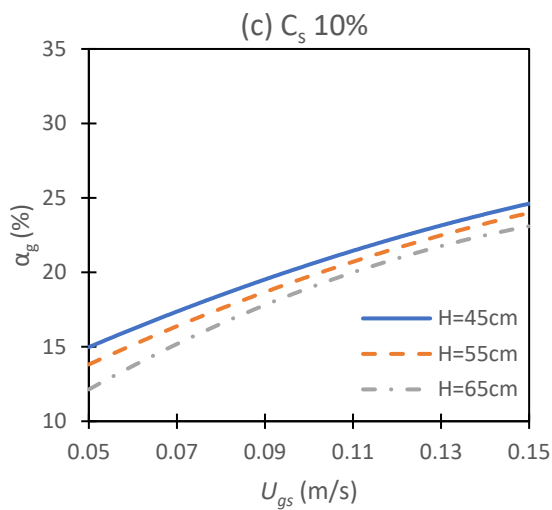
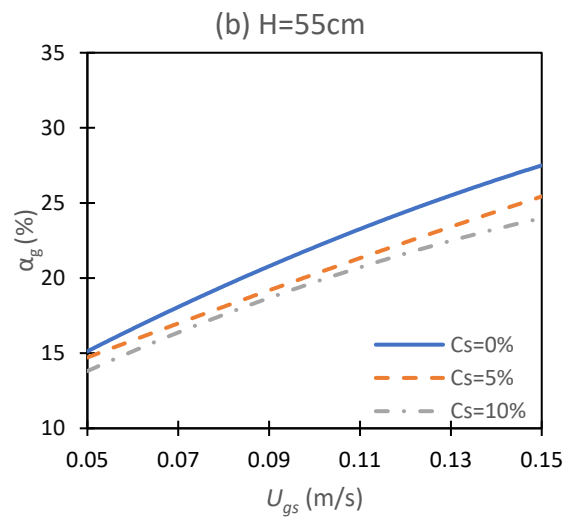
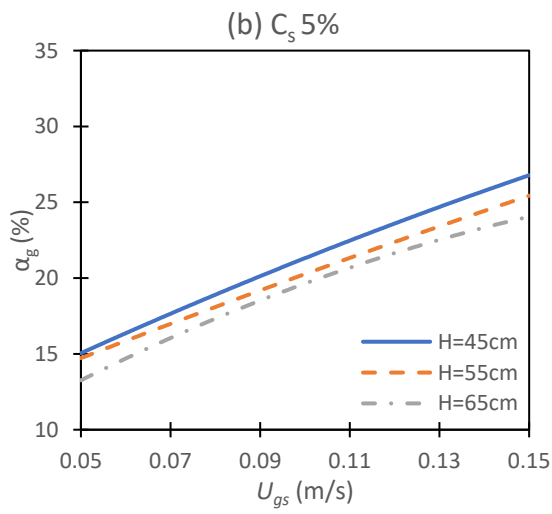
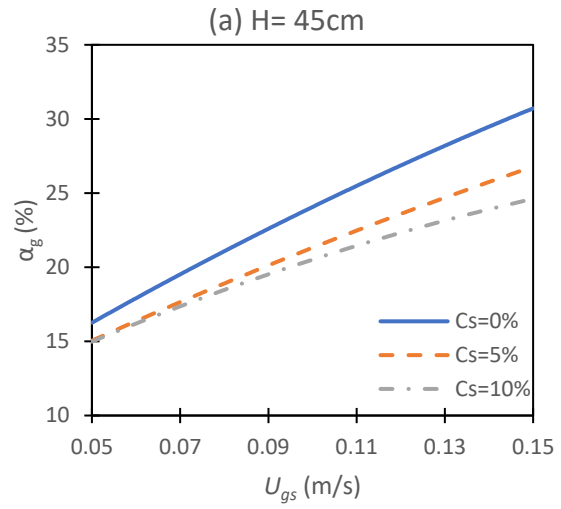
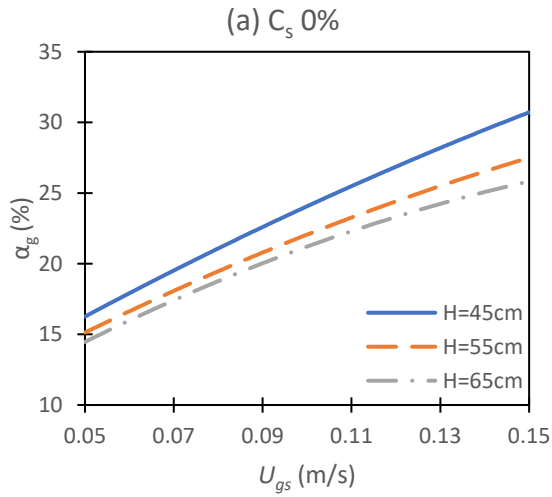


Figure 4.3 Average Gas Holdup Versus Superficial Gas Velocity of Helium-Water-Alumina System at Different Heights for Different Solid Particle Concentrations (a) 0%, (b) 5%, (c) 10%.

Fig. 4.4 Average Gas Holdup Versus Superficial Gas Velocity Helium-Water-Alumina System at Different Solid particle Concentrations for Different Static Liquid Heights (a) H=45cm, (b) H=55cm, (c) H=65cm.

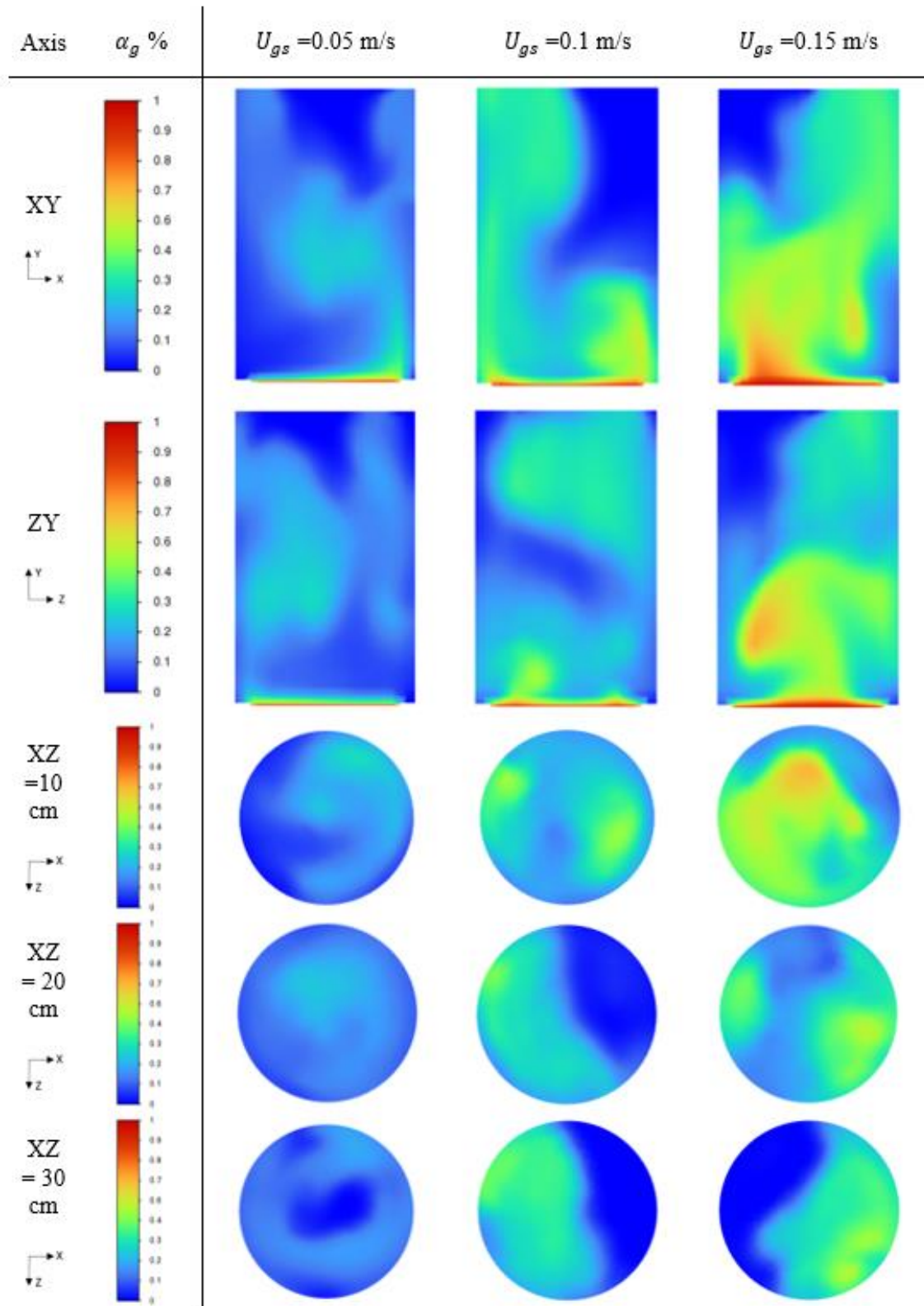


Figure. 4. 5 Water- Helium-Alumina Gas Holdup Contours for H=45cm, Cs=0%.

Axis	α_g %	$U_{gs} = 0.05$ m/s	$U_{gs} = 0.1$ m/s	$U_{gs} = 0.15$ m/s
------	--------------	---------------------	--------------------	---------------------

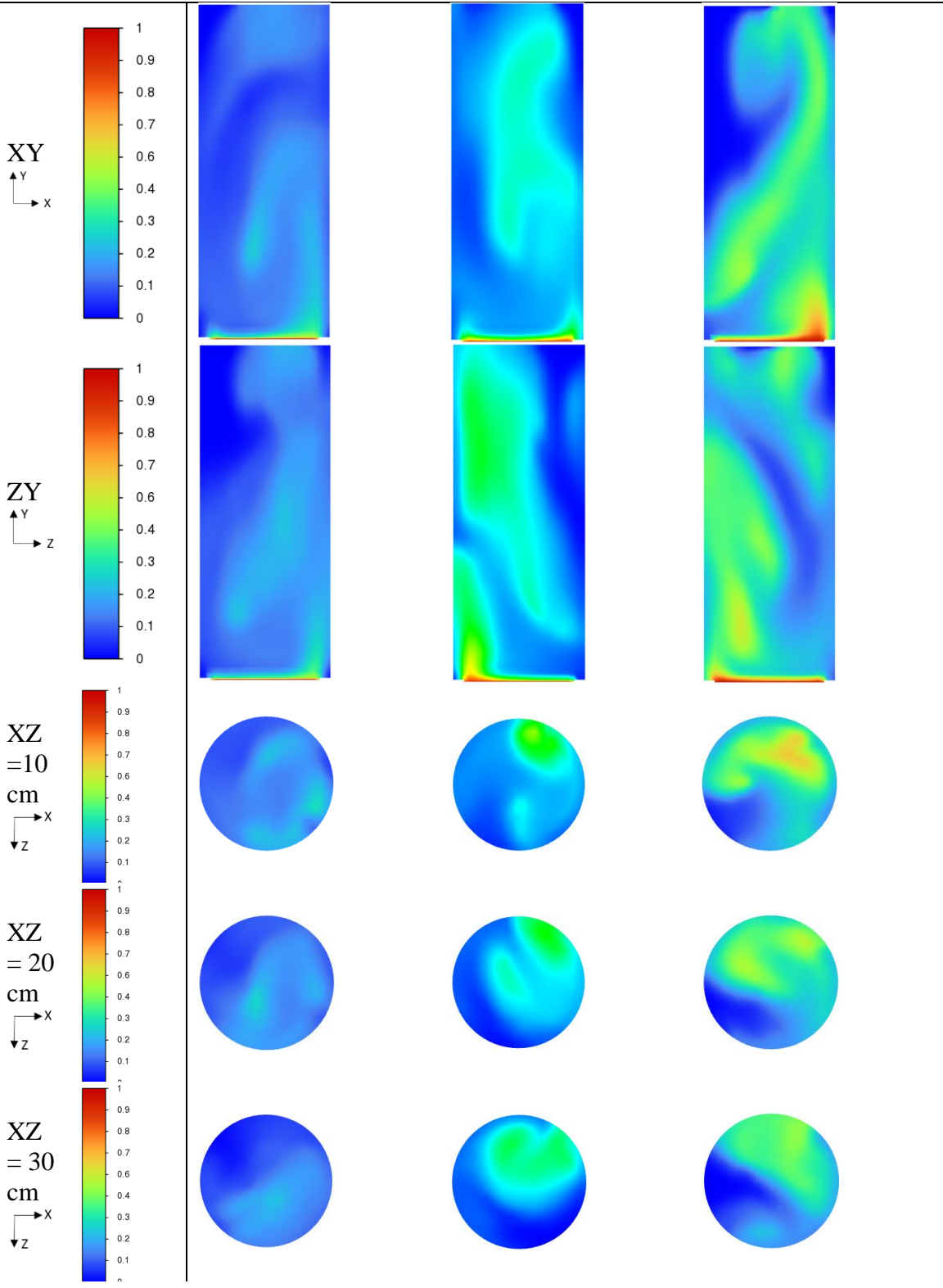


Figure. 4. 6 Water- Helium-Alumina Gas Holdup Contours for H=65cm, Cs=0%.

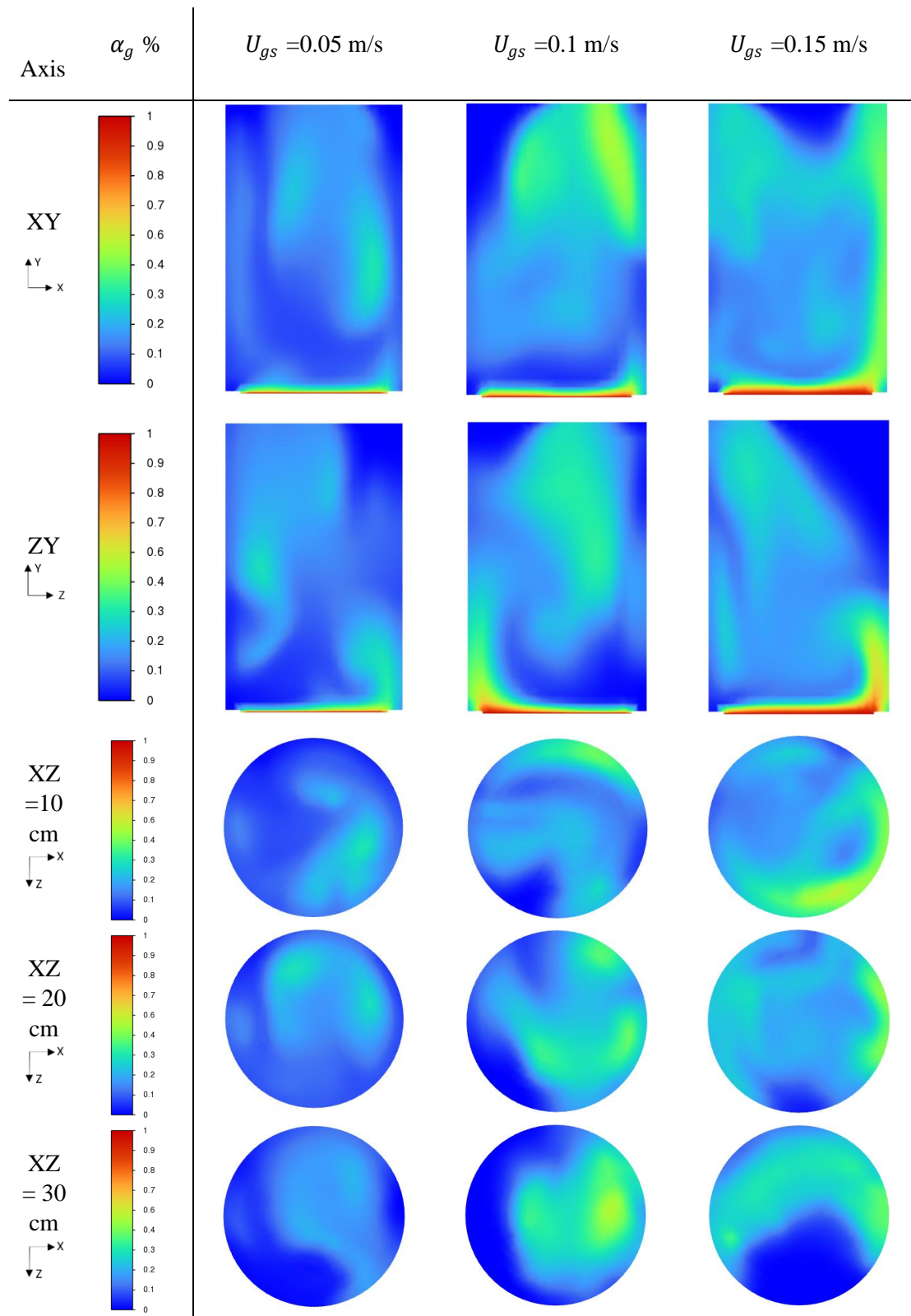


Figure. 4. 7 Water- Helium-Alumina Gas Holdup Contours for H=45cm, Cs=10%.

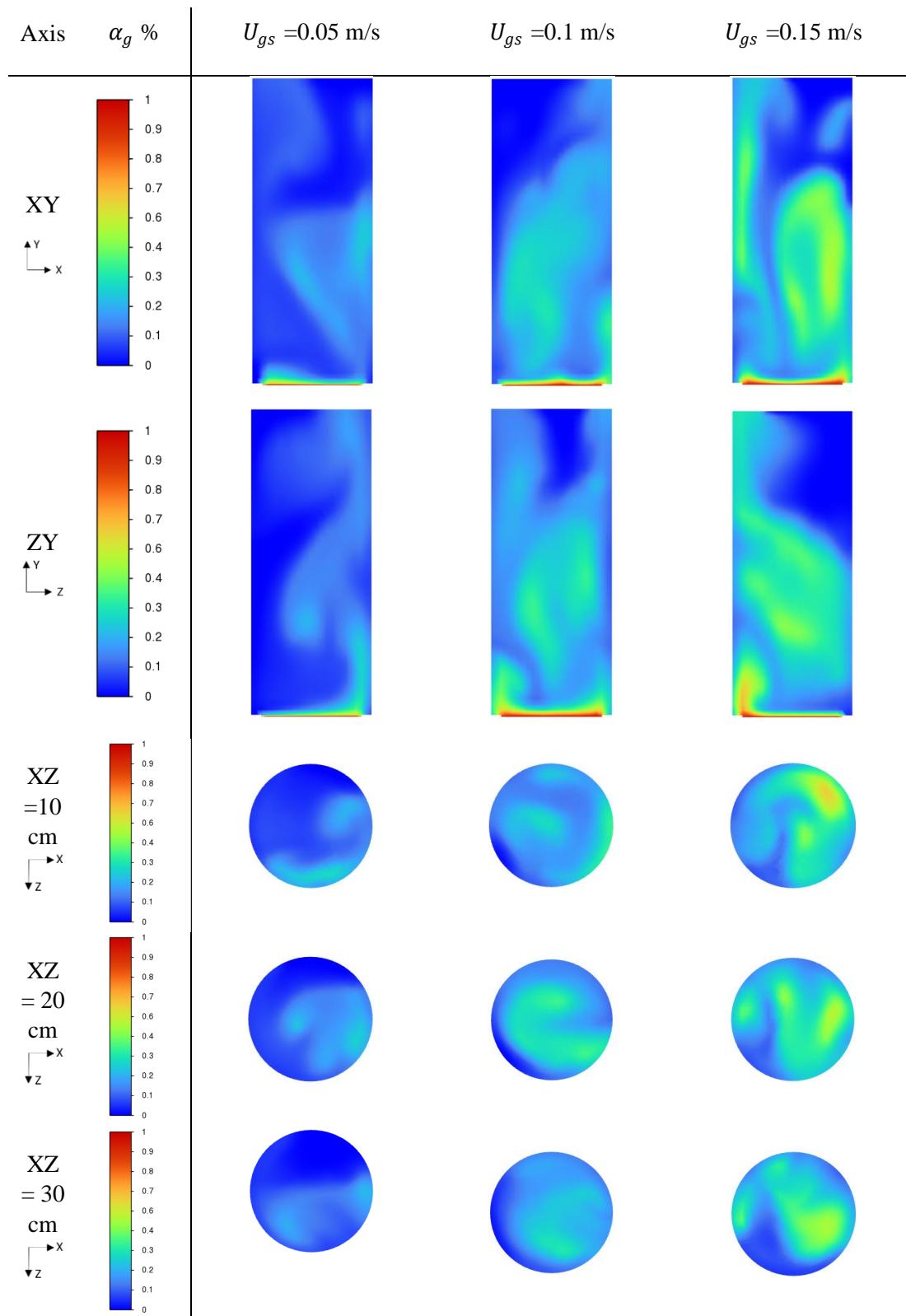
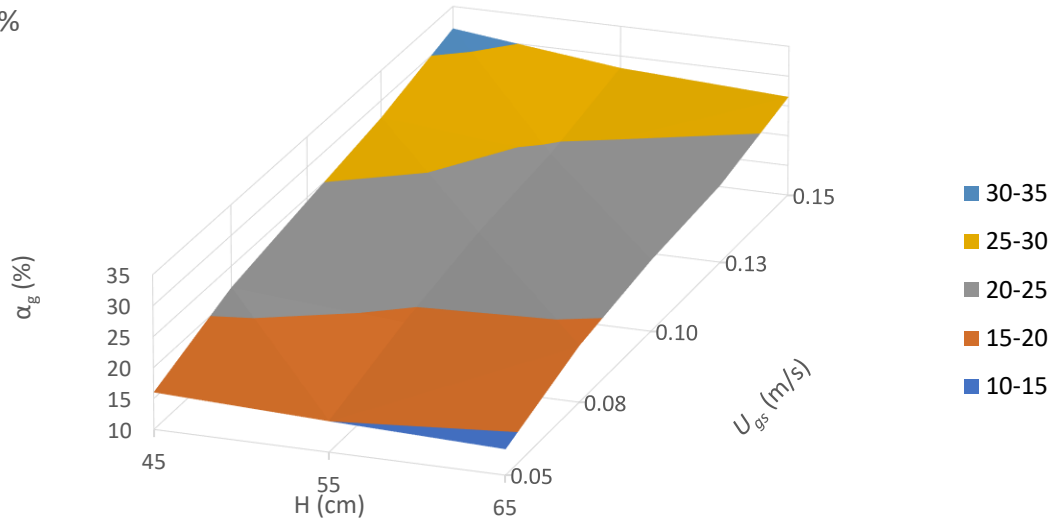


Figure. 4. 8 Water- Helium-Alumina Gas Holdup Contours for H=65cm, Cs=10%.

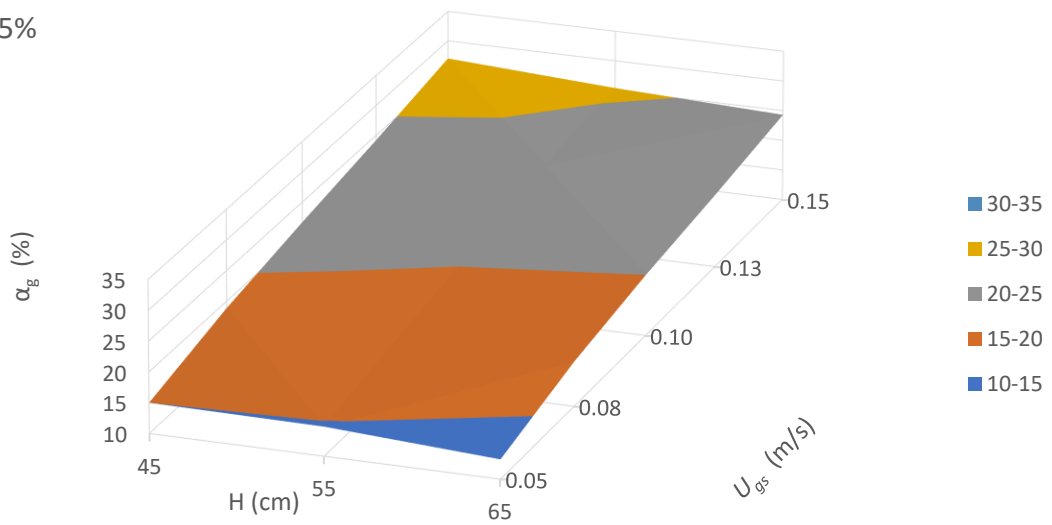
4.2.2 Effects of Static Liquid Height (H) on Gas Holdup (α_g)

Figure. 4.9 shows the three-dimensional curves of the gas holdup (α_g) versus static liquid height (H) and superficial gas velocity (U_{gs}) for different solid particle concentration (C_s). Figure. 4.10 shows the three-dimensional curves of the gas holdup versus H and C_s for different U_{gs} . Figures. 4.11 and 4.12 depict the effects of varying H on α_g while varying the U_{gs} and the C_s for a helium-water-alumina system. From the figures it can be observed that increasing H leads to a lower α_g for different C_s . Figures. 4.13-4.16 show the contours of the cut section of the SBCR taken in the center of the XY, and ZY planes. Additional cut sections are taken at various heights on the ZX plane within the reactor at heights 10, 20 and 30 cm from the base of the reactor to allow for more detailed contours of α_g . It is clear from the contours that the gas holdup is not symmetrical on the XY, ZY and the ZX planes demonstrating that the behavior of the gas holdup is strongly three dimensional. It is observed that as the H increases the α_g decreases. For $C_s=0\%$ increasing the H from 45cm to 65cm at a superficial gas velocity of 0.05m/s leads to a decrease in the gas holdup by approximately 11%. A decrease in the gas holdup of approximately 15% was observed for a superficial gas velocity of 0.15m/s was observed when increasing the H from 45cm to 65cm. This is due to the increase in hydrostatic pressure and pressure drop when the H increases for certain U_{gs} . Additionally, having shorter SBCR ($H_R/D_R < 3$) can prevent the liquid circulation patters from fully developing which tends to decrease α_g [60].

(a) $C_s = 0\%$



(b) $C_s = 5\%$



(c) $C_s = 10\%$

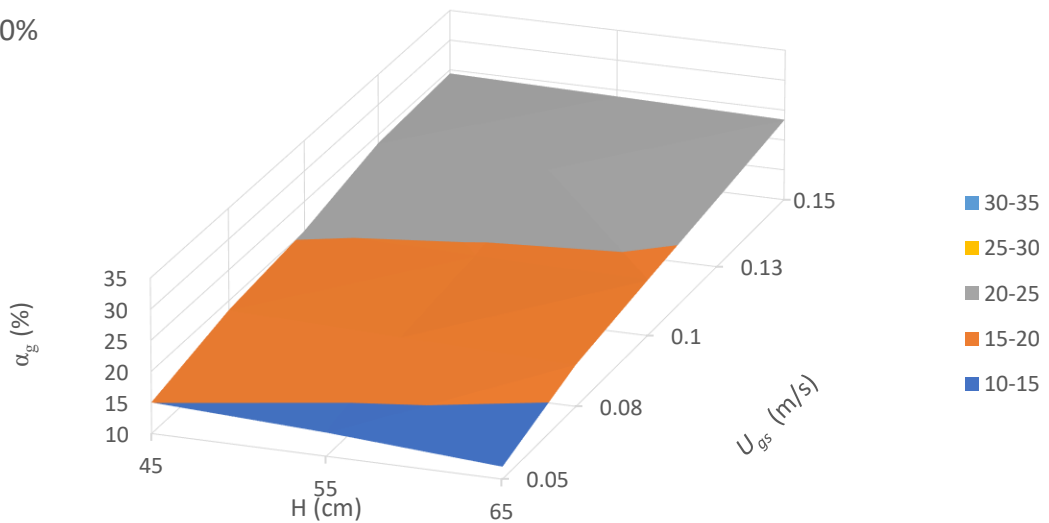
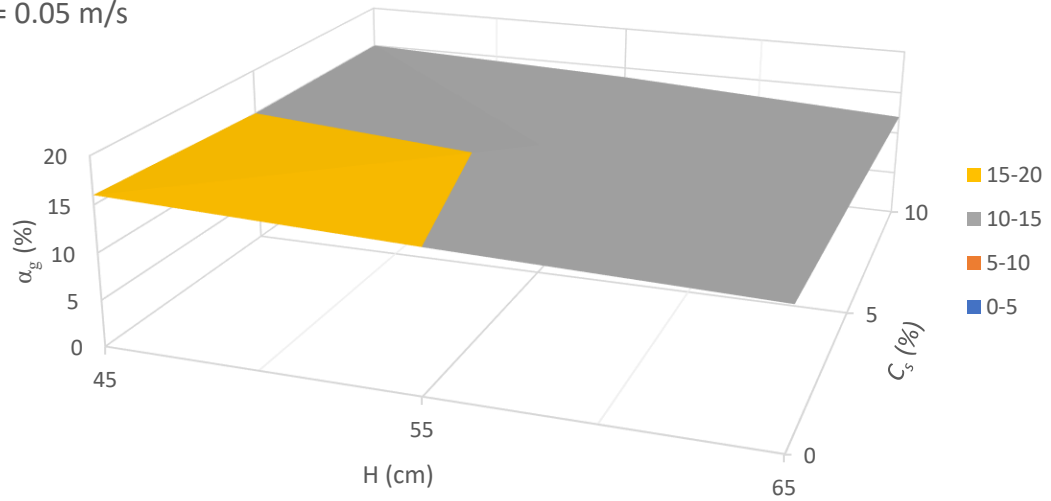
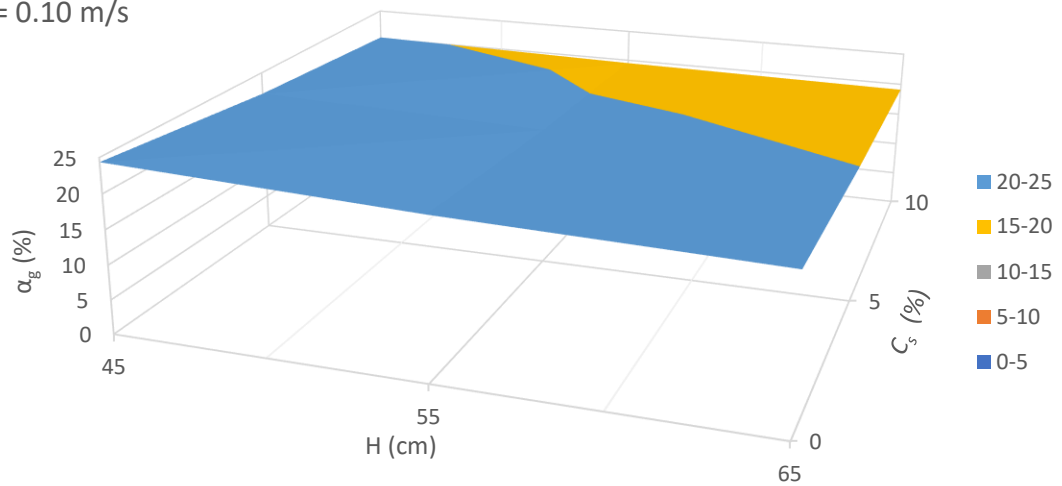


Figure. 4. 9 Average Gas Holdup Versus Static Liquid Height and Superficial Gas Velocity of Helium-Water-Alumina at (a) $C_s=0\%$, (b) $C_s=5\%$, (c) $C_s=10\%$.

(a) $U_{gs} = 0.05 \text{ m/s}$



(b) $U_{gs} = 0.10 \text{ m/s}$



(c) $U_{gs} = 0.15 \text{ m/s}$

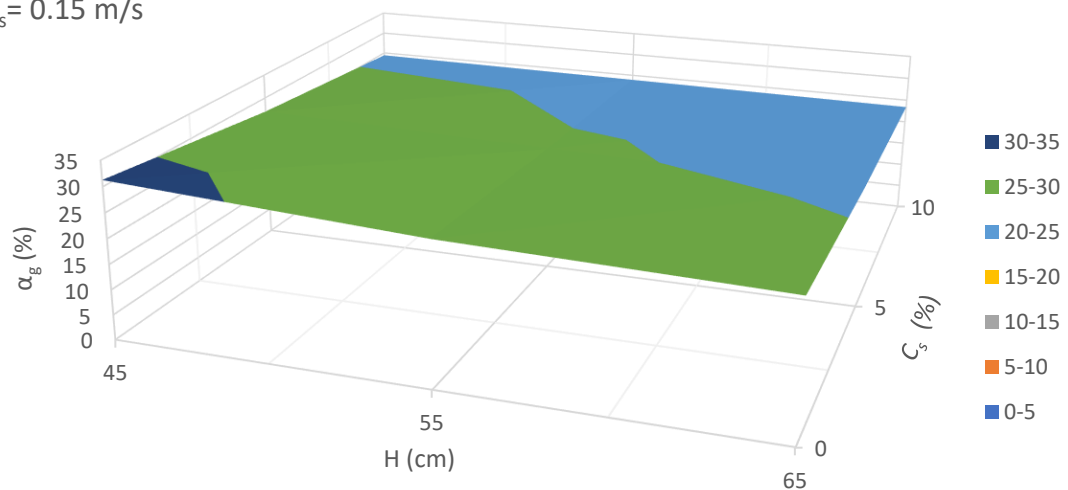


Figure. 4. 10 Average Gas Holdup Versus Static Liquid Height and Solid Particle Concentration of Helium-Water-Alumina at (a) $U_{gs}=0.05\text{m/s}$ (b) $U_{gs}=0.1\text{m/s}$ (c) $U_{gs}=0.15\text{m/s}$.

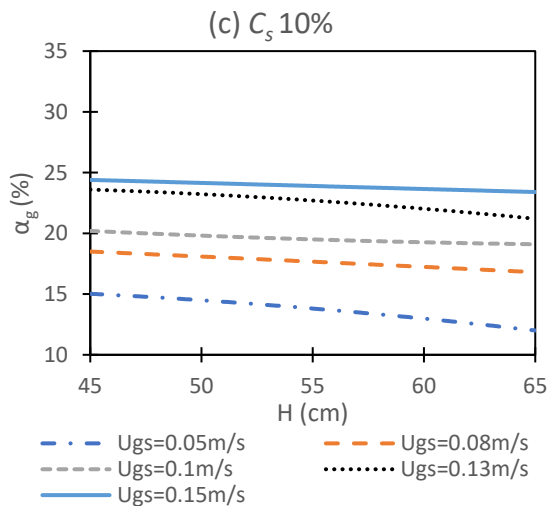
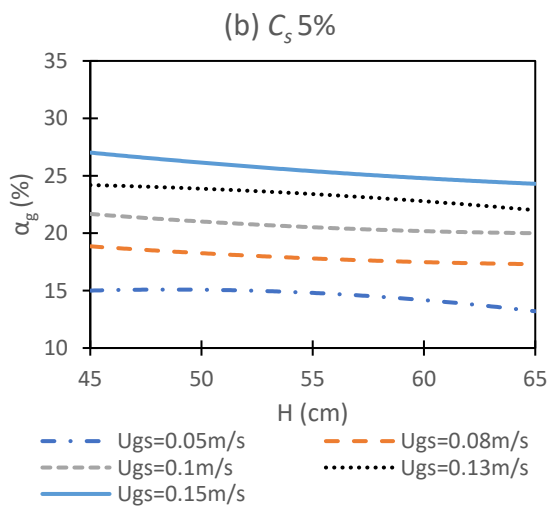
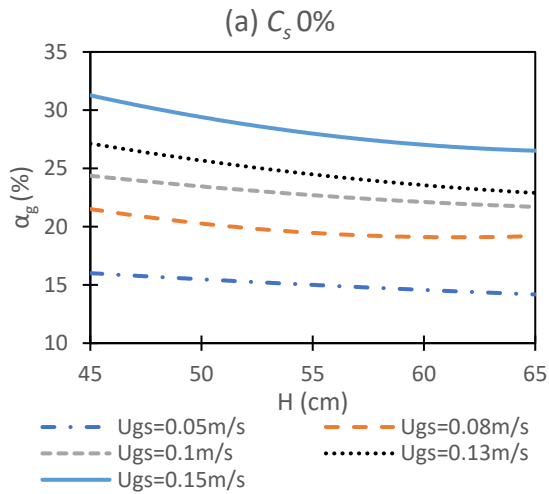


Figure 4. 11 Average Gas holdup Versus Static Liquid Height of Helium-Water-Alumina system at Different Superficial Velocities for (a) $C_s = 0\%$, (b) $C_s = 5\%$, (c) $C_s = 10\%$.

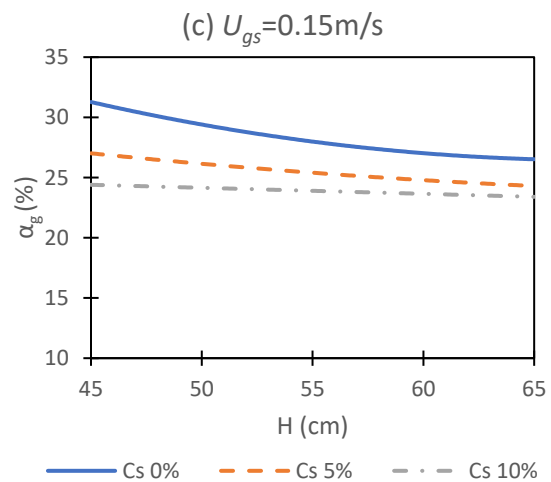
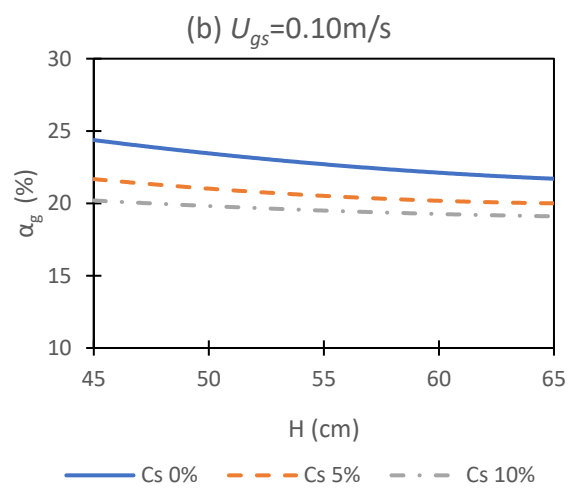
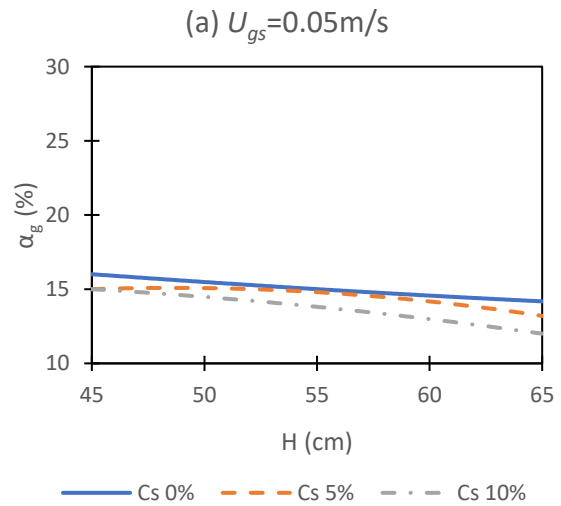


Figure 4. 12 Average Gas holdup Versus Static Liquid Height of Helium-Water-Alumina system at Different Solid Particle Concentrations for (a) $U_{gs} = 0.05$, (b) $U_{gs} = 0.10$, (c) $U_{gs} = 0.15$ m/s.

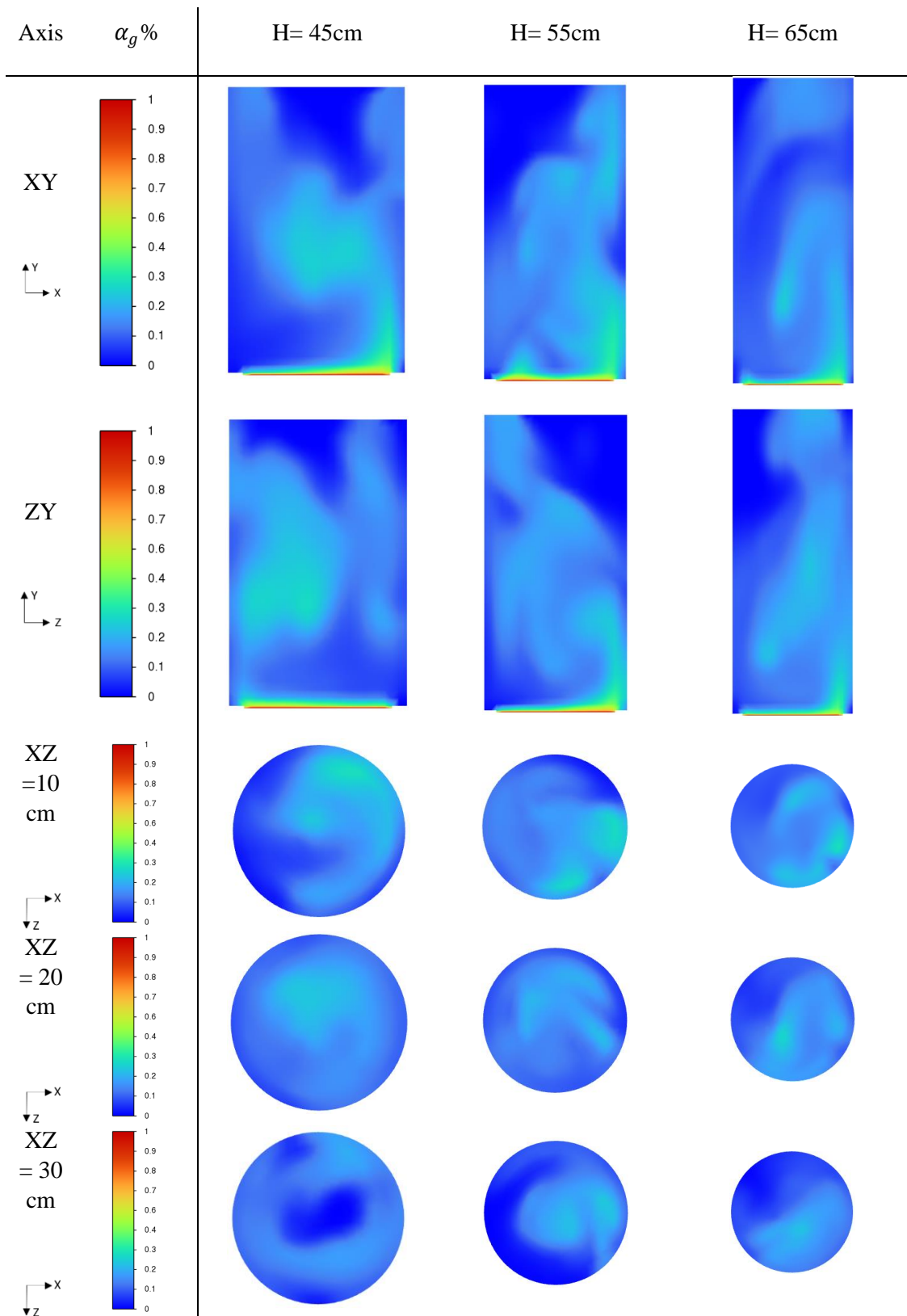


Figure. 4. 13 Water- Helium-Alumina Gas Holdup Contours for $U_{gs}=0.05\text{m/s}$ at $C_s=0\%$ for Different Static Liquid Heights.

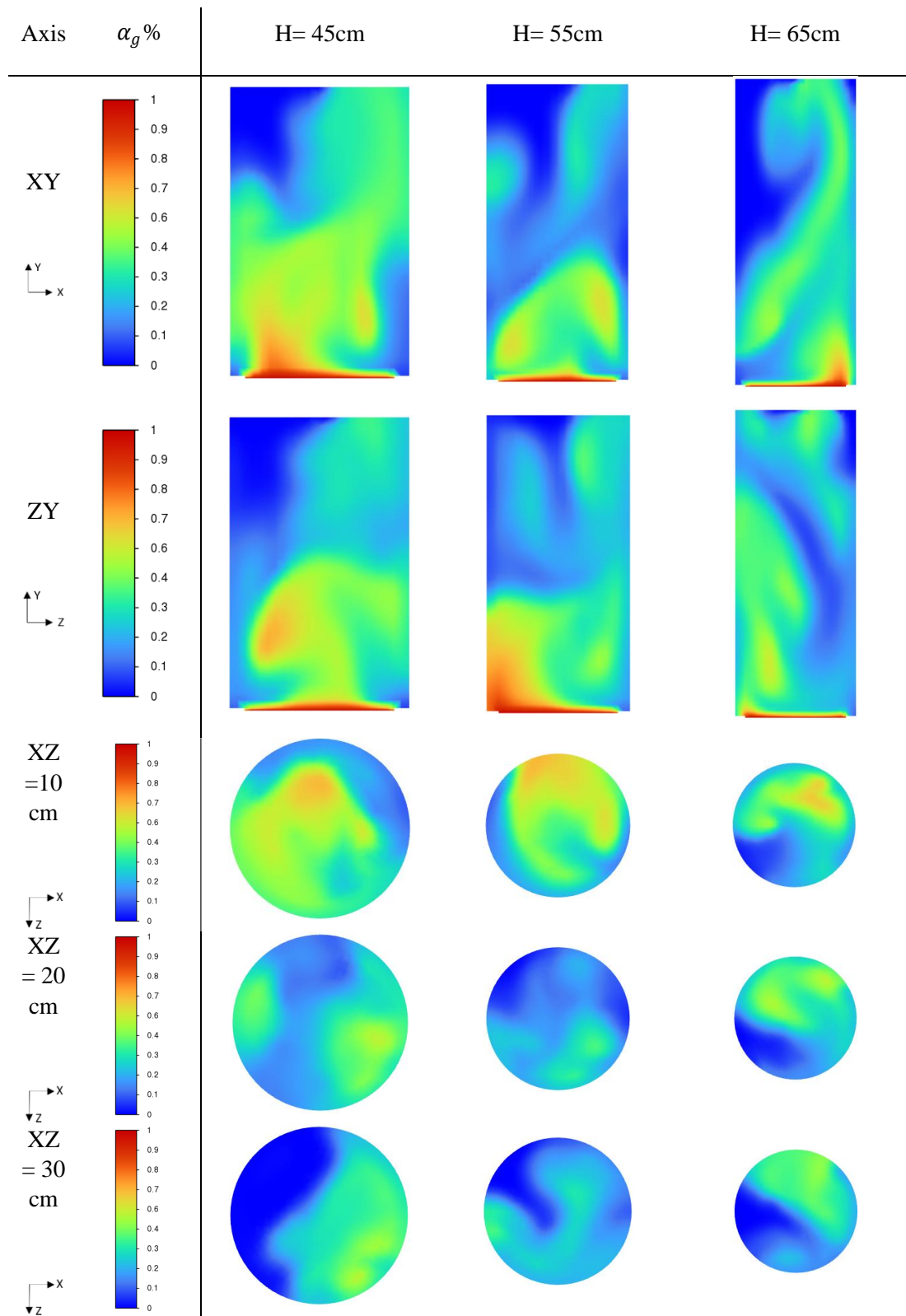


Figure. 4. 14 Water- Helium-Alumina Gas Holdup Contours for $U_{gs}=0.15\text{m/s}$ at $C_s=0\%$ for Different Static Liquid Heights.

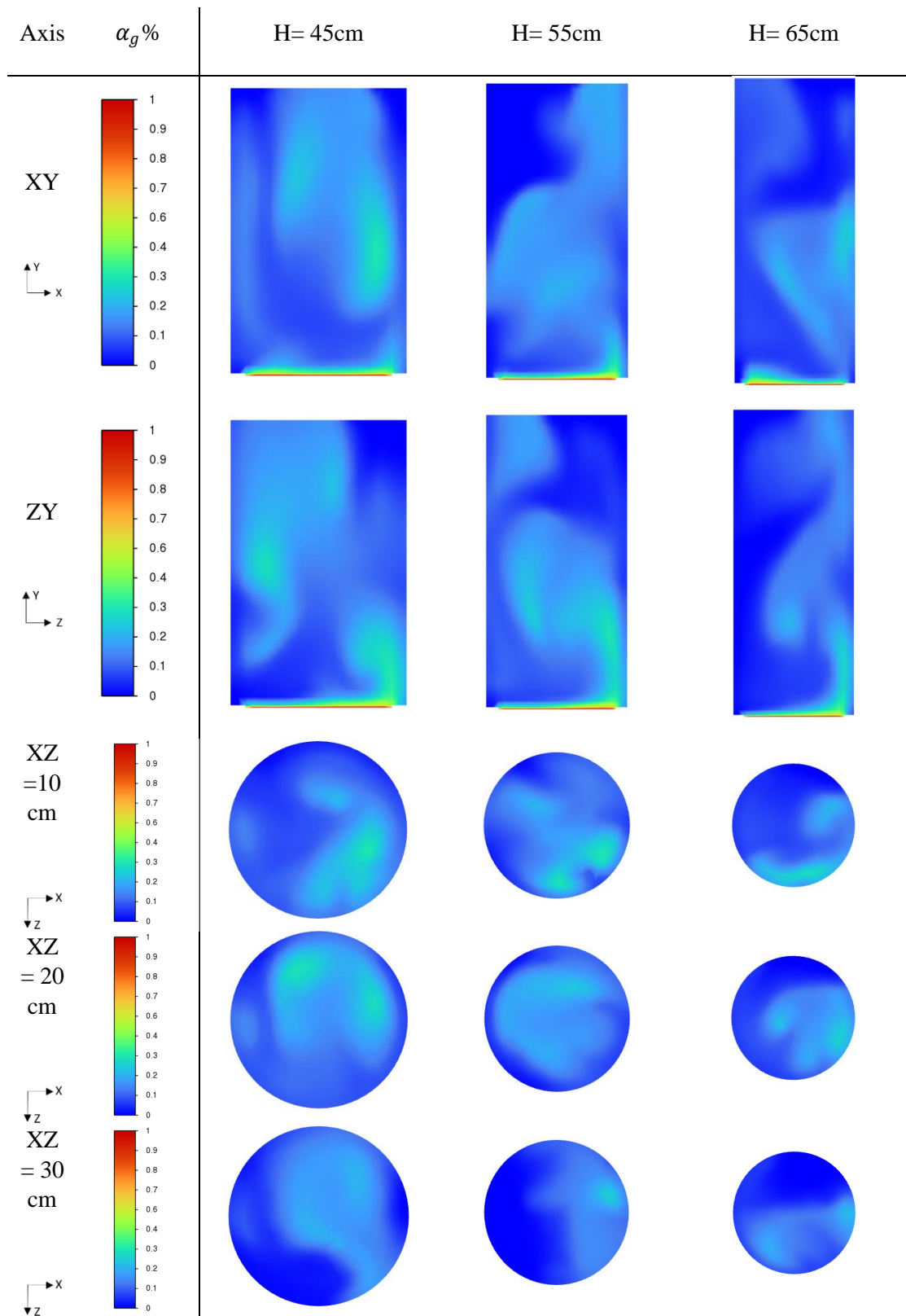


Figure. 4. 15 Water- Helium-Alumina Gas Holdup Contours for $U_{gs}=0.05\text{m/s}$ at $C_s=10\%$ for Different Static Liquid Heights.

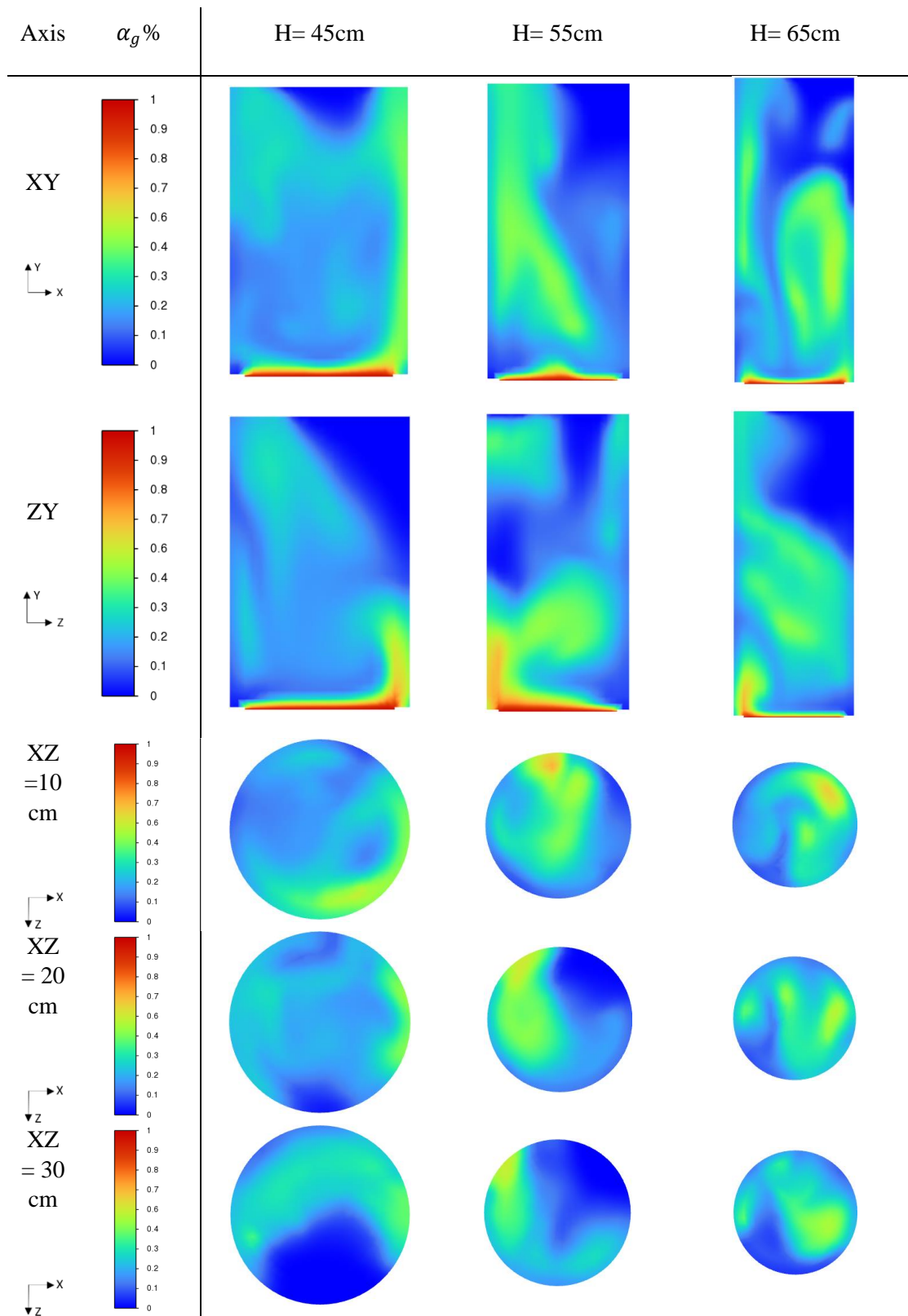
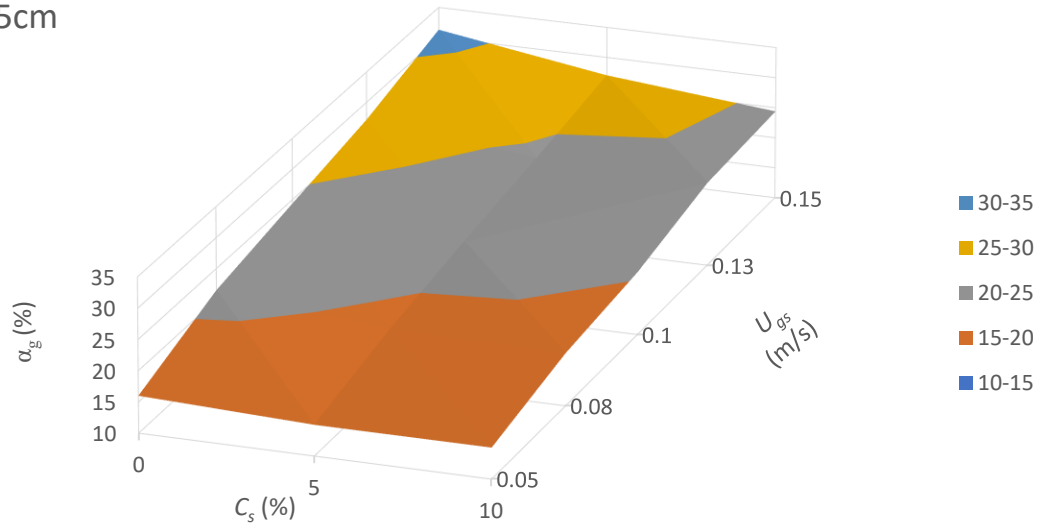


Figure. 4. 16 Water- Helium-Alumina Gas Holdup Contours for $U_{gs}=0.15\text{m/s}$ at $C_s=10\%$ for Different Static Liquid Heights.

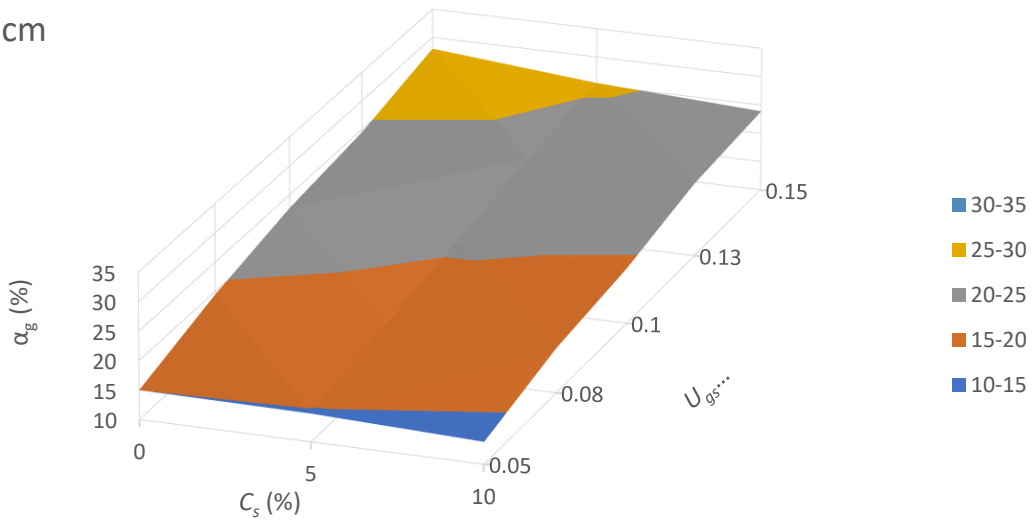
4.2.3 Effects of Solid Particle Concentration (C_s) on Gas Holdup (α_g)

Figure. 4.17 shows the three-dimensional curves of the gas holdup versus the C_s and U_{gs} for different Hs. Figure. 4.18 shows the three-dimensional curves for the gas holdup versus the C_s and the H for different U_{gs} . Figure. 4.19 and 4.20 depict the effects of varying the C_s on the α_g while varying the H and U_{gs} for a helium-water alumina system. Figures. 4.21- 4.24 show the contours of the cut section for the SBCR taken in the center of the XY, and ZY planes. Additional cut sections are taken at various heights on the ZX plane within the reactor at heights 10, 20 and 30 cm from the base of the reactor to allow for a more detailed contours of α_g . It is clear from the contours that the gas holdup is not symmetrical on the XY, ZY and the ZX planes demonstrating that the behavior of the gas holdup is strongly three dimensional. It is observed that as the C_s increases the α_g decreases. When $H=45\text{cm}$ at a superficial gas velocity of 0.05m/s and the concentration is increased from $C_s=0\%$ to $C_s=10\%$ the gas holdup decreases by a rate of around 6%. While for $H=55\text{cm}$ at a superficial gas velocity of 0.15m/s the gas holdup decreases by a rate of 14% when increasing the C_s from $C_s=0\%$ to $C_s=10\%$. This trend is observed because increasing the solid particle concentration increases the slurry viscosity. The increased viscosity leads to large gas bubbles being formed and reduces bubbles breakage rates caused by instabilities at the interface. The large bubbles will lower the gas holdup as they have a high-rise velocity [61].

(a) H=45cm



(b) H=55cm



(c) H=65cm

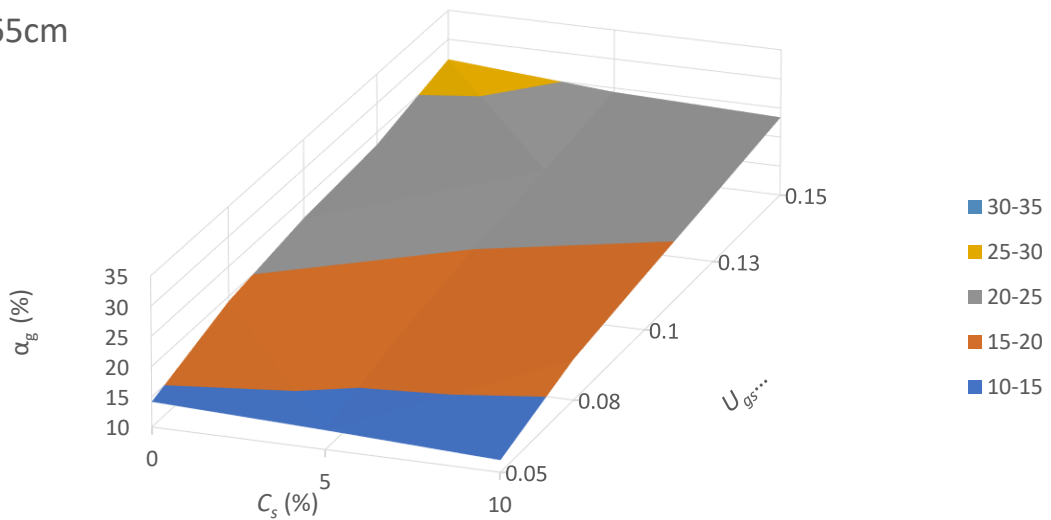
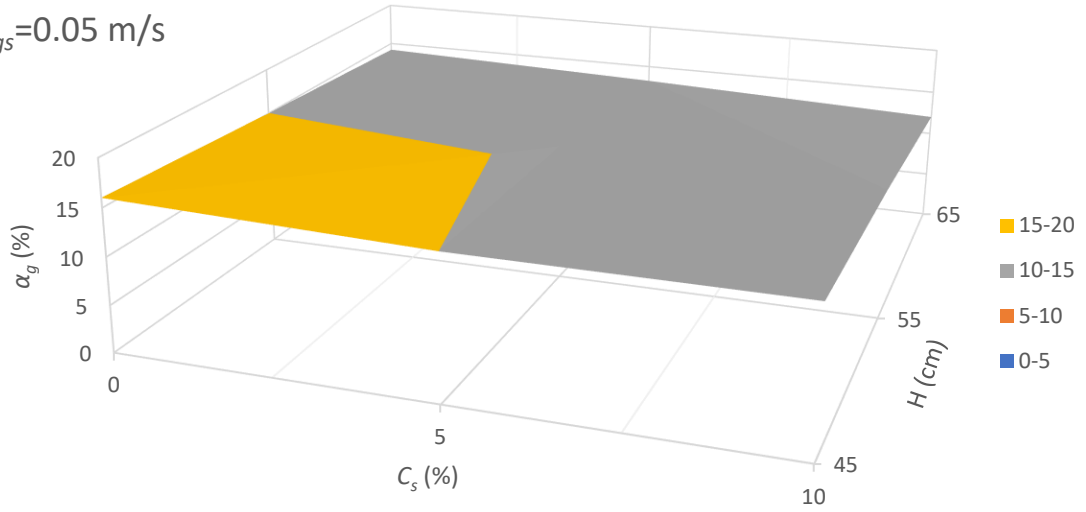
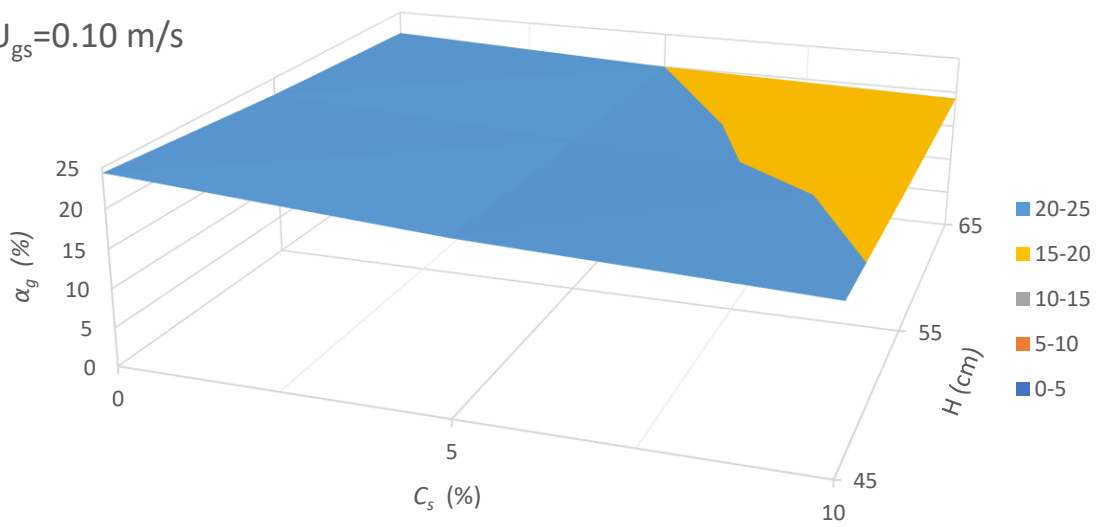


Figure. 4. 17 Average Gas Holdup Versus Solid Particle Concentration and Superficial Gas Velocity of Helium-Water-Alumina at (a) H=45 (b) H=55, (c) H=65cm.

(a) $U_{gs}=0.05$ m/s



(b) $U_{gs}=0.10$ m/s



(c) $U_{gs}=0.15$ m/s

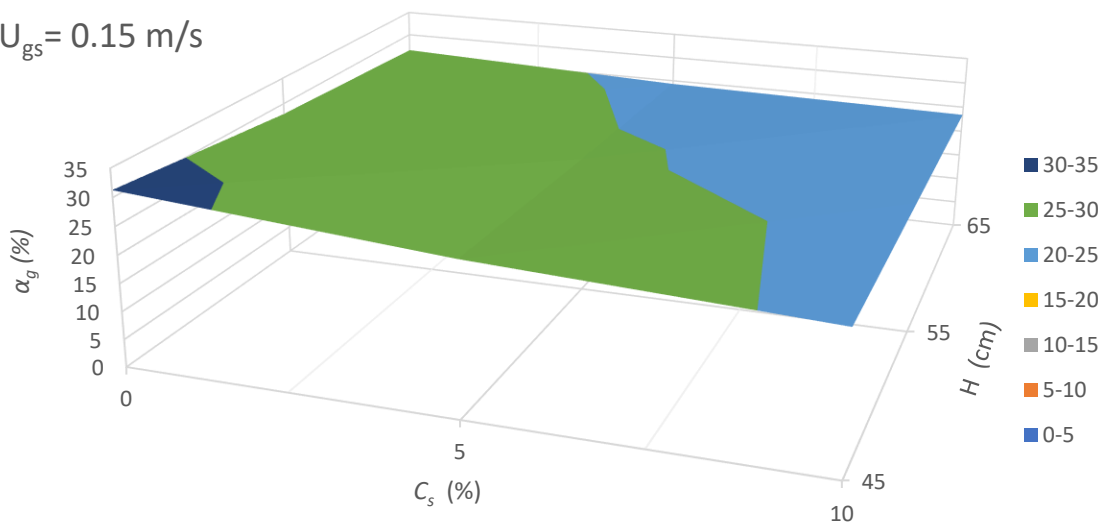


Figure. 4. 18 Average Gas Holdup Versus Solid Particle Concentration and Static Liquid Height of Helium-Water-Alumina at (a) $U_{gs}=0.05$ m/s (b) $U_{gs}=0.1$ m/s (c) $U_{gs}=0.15$ m/s.

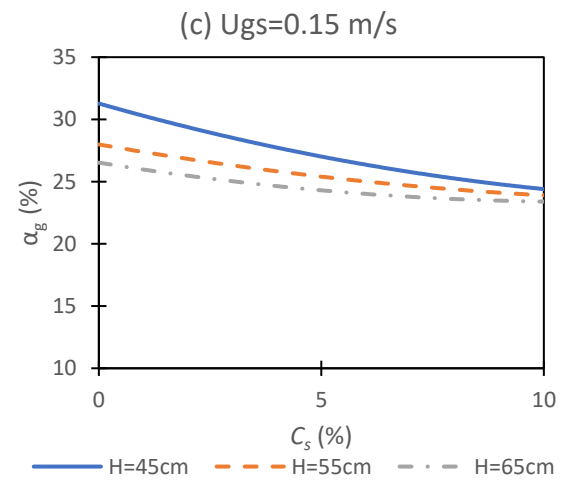
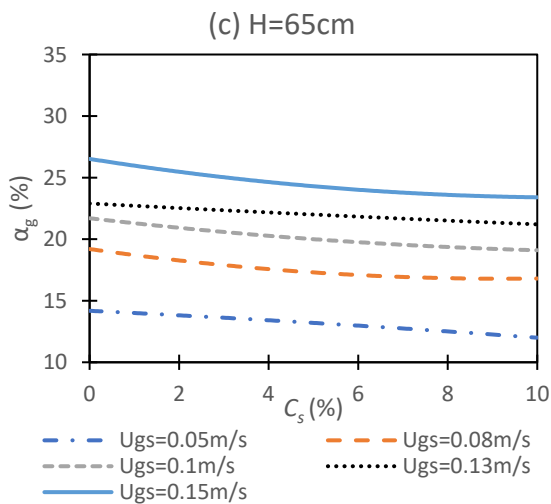
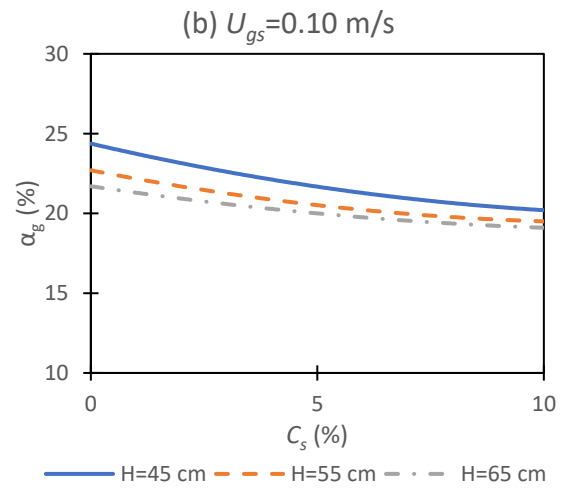
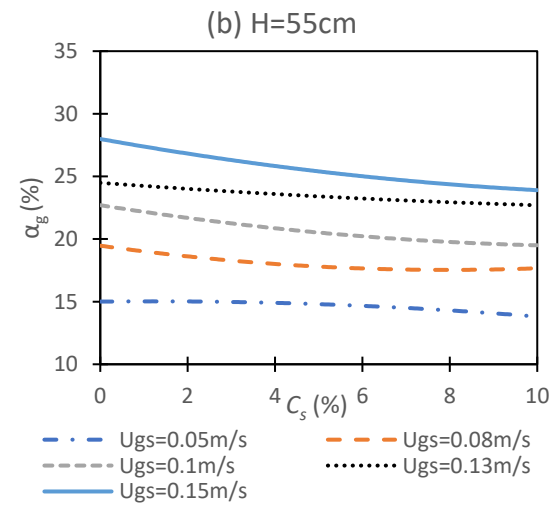
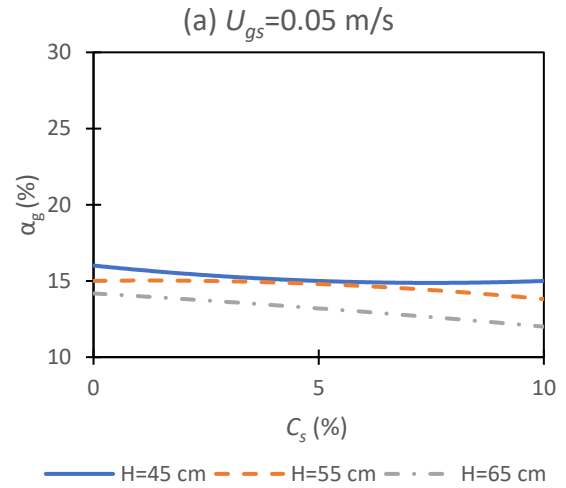
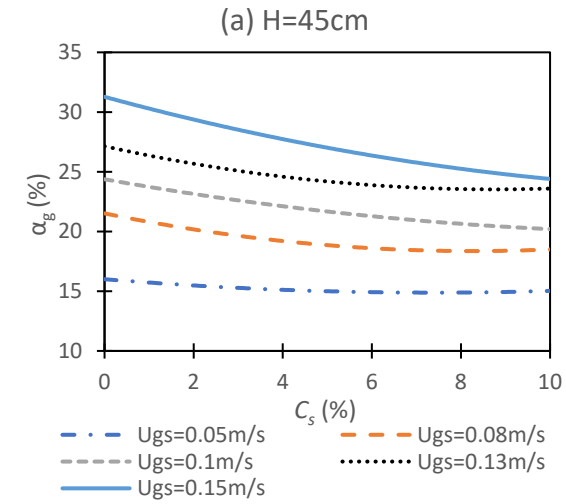


Figure. 4. 19 Average Gas holdup Versus Solid Particle Concentration of Helium-Water-Alumina System at Different Superficial Velocities for (a) H=45 (b) H=55 (c) H=65cm.

Figure. 4. 20 Average Gas holdup Versus Solid Particle Concentration of Helium-Water-Alumina System at Different Static Liquid Heights for (a) $U_{gs}=0.05$, (b) $U_{gs}=0.10$, (c) $U_{gs}=0.15$ m/s.

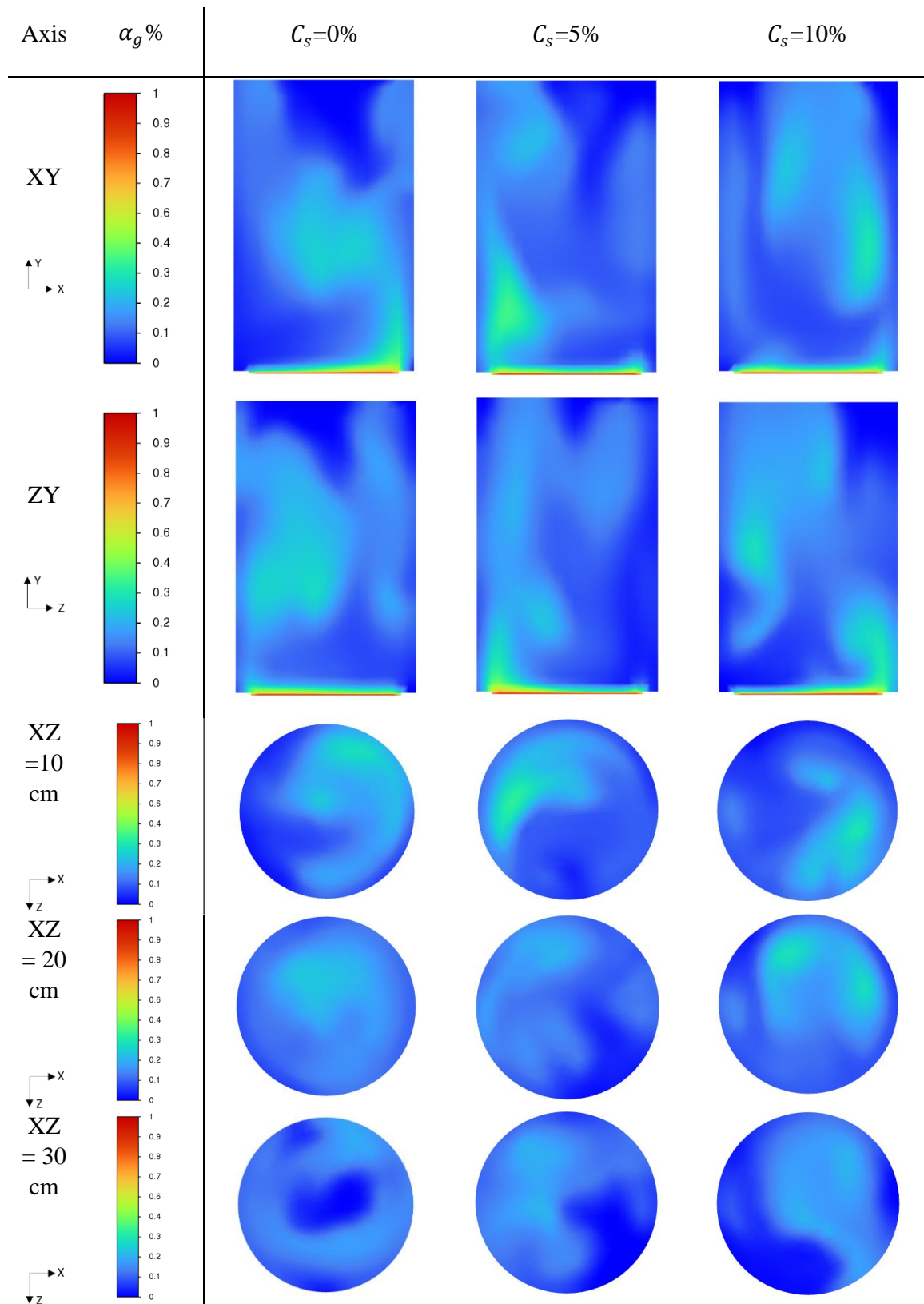


Figure. 4. 21 Water- Helium-Alumina Gas Holdup Contours for $U_{gs}=0.05\text{m/s}$ at $H=45\text{cm}$ for Different Solid Particle Concentrations.

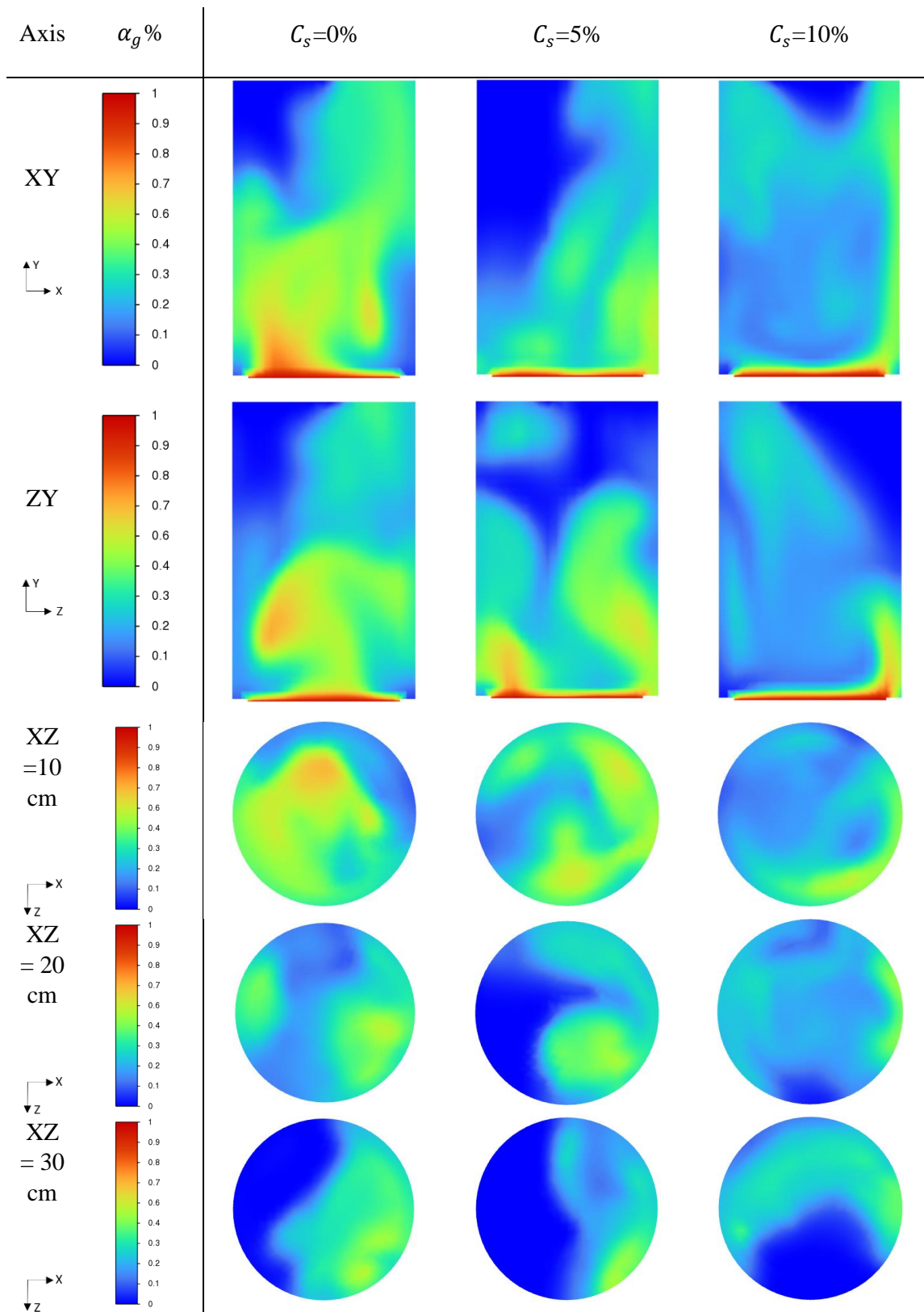


Figure. 4. 22 Water- Helium-Alumina Gas Holdup Contours for $U_{gs}=0.15\text{m/s}$ at $H=45\text{cm}$ for Different Solid Particle Concentrations.

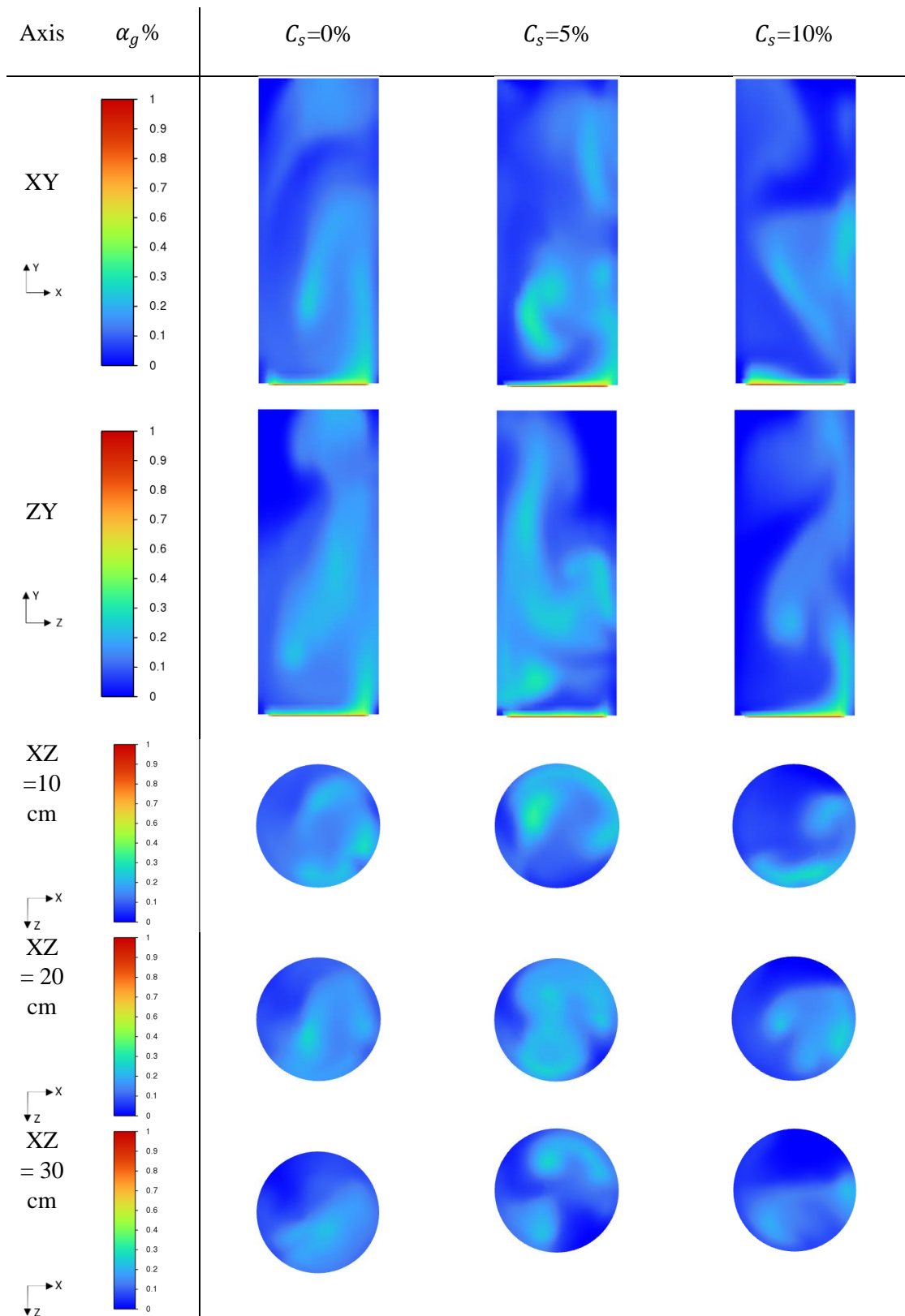


Figure. 4. 23 Water- Helium-Alumina Gas Holdup Contours for $U_{gs}=0.05\text{m/s}$ at $H=65\text{cm}$ for Different Solid Particle Concentrations.

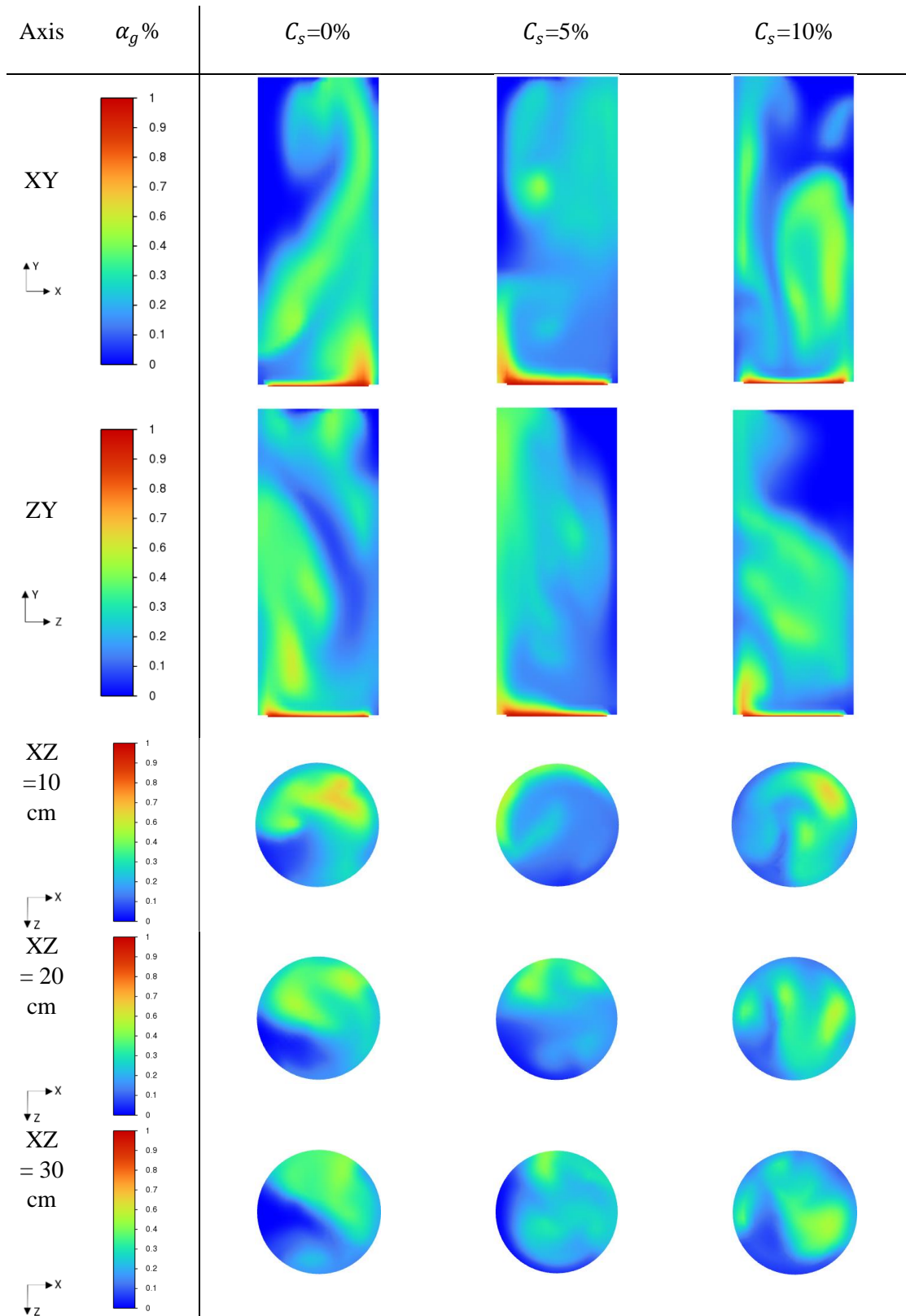


Figure. 4. 24 Water- Helium-Alumina Gas Holdup Contours for $U_{gs}=0.15\text{m/s}$ at $H=65\text{cm}$ for Different Solid Particle Concentrations.

4.3 Gas Holdup Results of the 3D-CFD Simulations of the Oxygen-Cupreous Chloride System

In this section the gas holdup of the Oxygen-Cupreous Chloride (O_2 -CuCl) system is simulated and the effects of varying superficial gas velocity, and static liquid height are studied. The system has the same dimensional setup of the Helium-Water system; however, the material properties are adjusted to match oxygen and Cupreous Chloride as mentioned in chapter 3. Additionally, the superficial gas velocity of the Oxygen-Cupreous Chloride system is adjusted to maintain the same Reynolds number of the Helium-Water system. The O_2 -CuCl system and the He- H_2O systems are comparable based on property comparison mentioned in chapter 3 conducted by Abdulrahman. A comparison was then conducted between the behavior of the Helium-Water system and the Oxygen-Cupreous Chloride system.

4.3.1 Effects of Superficial Gas Velocity on Gas Holdup

Figure 4.25 shows the three-dimensional curves of the gas holdup versus the U_{gs} and the H for $C_s=0\%$. Figure 4.26 depicts the effect of varying the U_{gs} (0.0283, 0.0567, 0.085 m/s) on the average gas holdup while varying the H (45, 55, 65cm) for C_s 0% for an O_2 - CuCl system. Figures. 4.27-4.29 show the contours of the cut sections of the SBCR taken in the center of the XY, and ZY planes. Additional cut sections are taken at various heights on the ZX plane within the reactor at heights 10, 20 and 30 cm from the base of the reactor to allow for a more detailed contours of α_g . It is clear from the contours that the gas holdup is not symmetrical on the XY, ZY and the ZX planes demonstrating that the behavior of the gas holdup is strongly three dimensional. From the figures, it can be observed that the physical behaviors of α_g with U_{gs} and H are the same for that of Helium-Water system, in which α_g increases by increasing U_{gs} and decreasing H . For $C_s=0\%$ and $H=45$ cm a 124% increase was observed in the gas holdup when increasing the superficial gas velocity from 0.0283m/s to 0.085m/s.

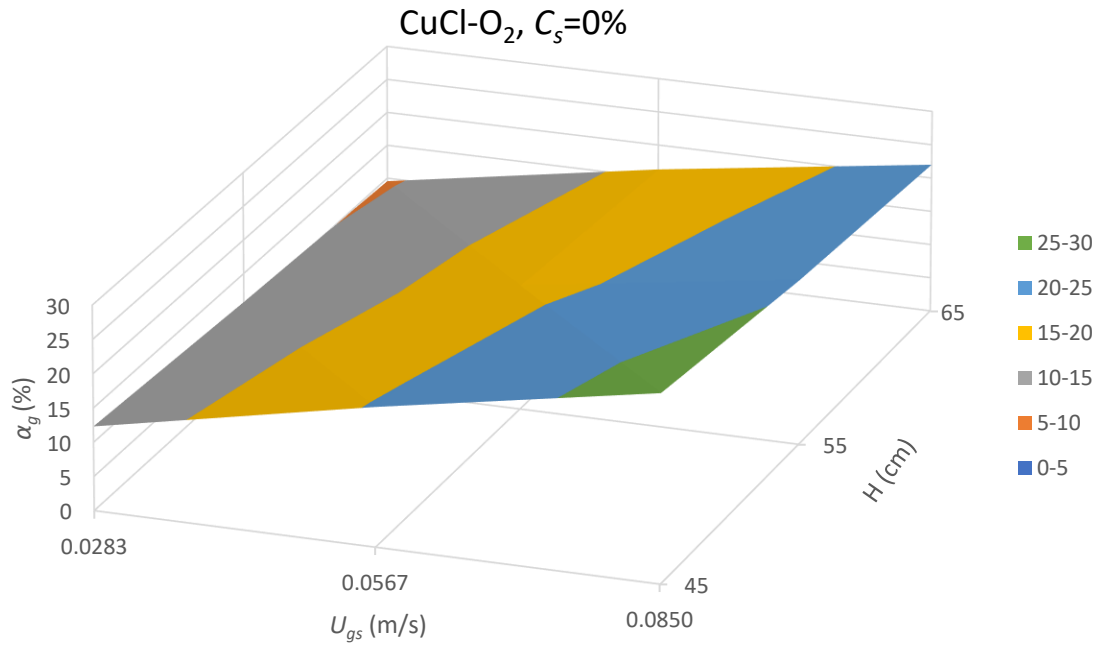


Figure. 4. 25 Average Gas Holdup Versus Superficial Gas Velocity Static Liquid Height of CuCl-O₂, C_s=0%.

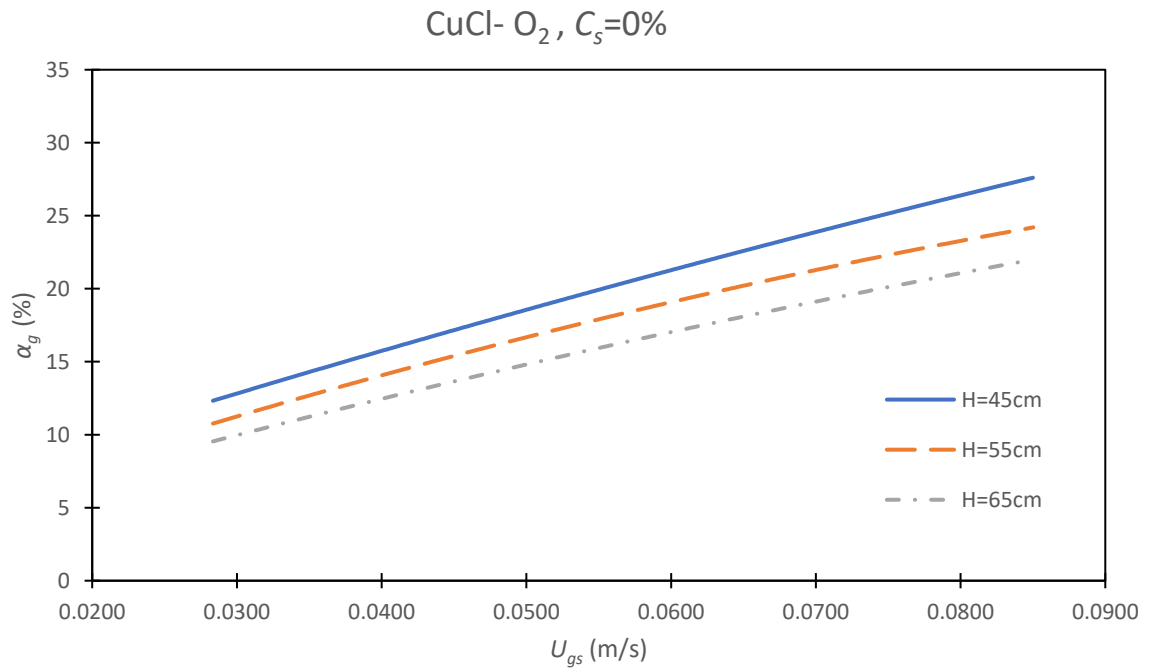


Figure. 4. 26 Average Gas Holdup Versus Superficial Gas Velocity of CuCl- O₂ for C_s=0%.

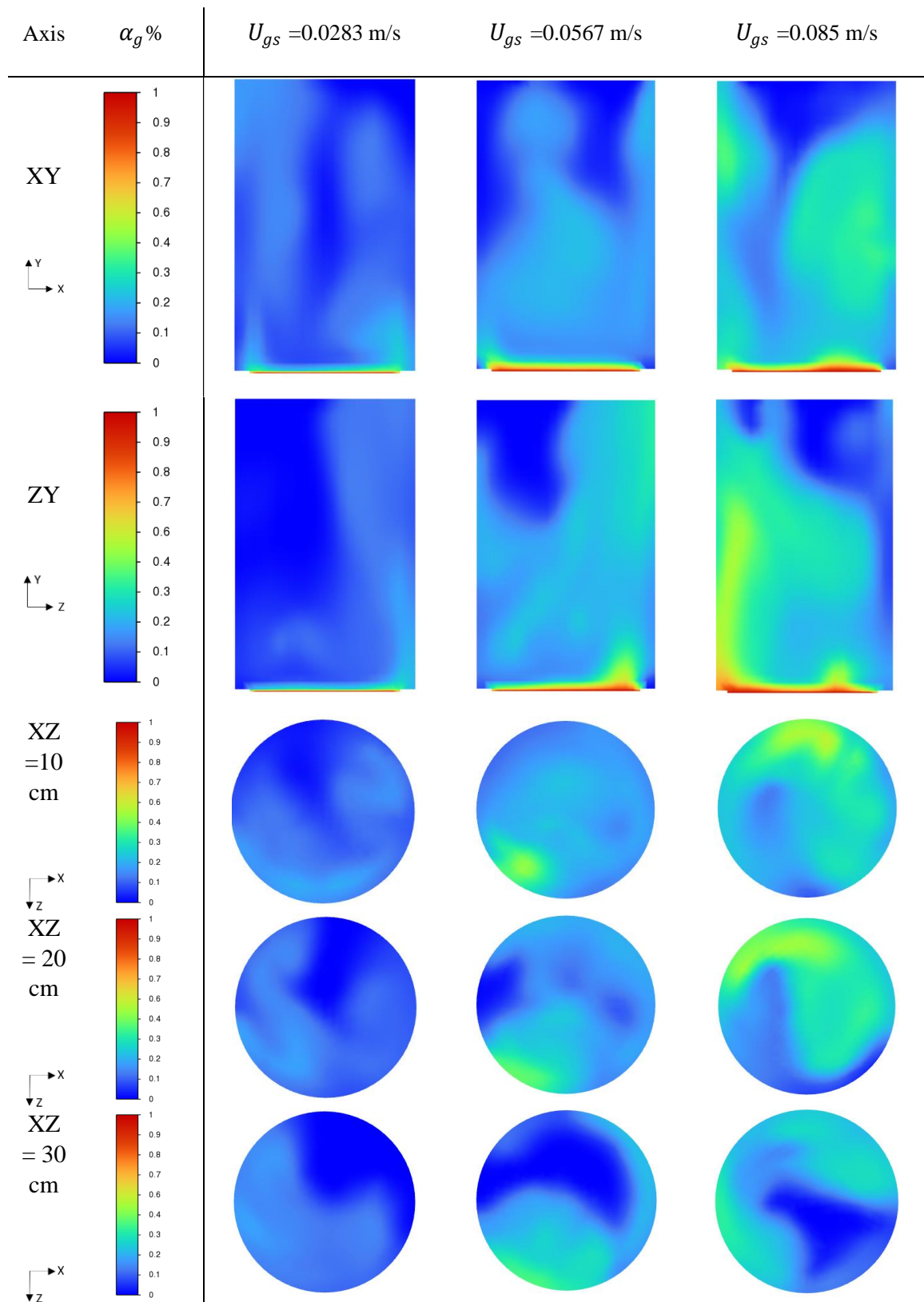


Figure. 4. 27 Oxygen-Cupreous Chloride Gas Holdup Contours for H=45cm, Cs=0%.

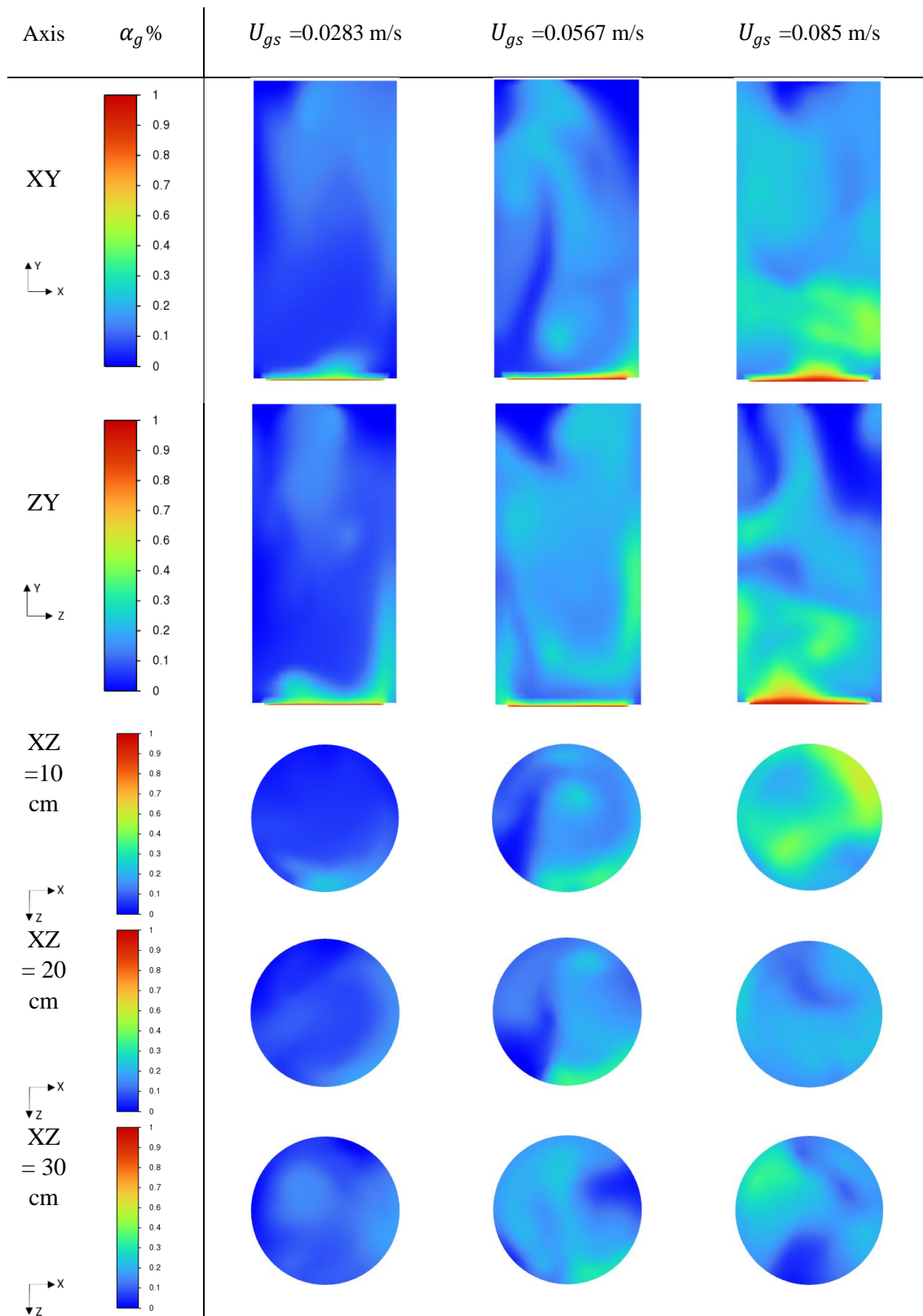


Figure. 4. 28 Oxygen-Cupreous Chloride Gas Holdup Contours for H=55cm, Cs=0%.

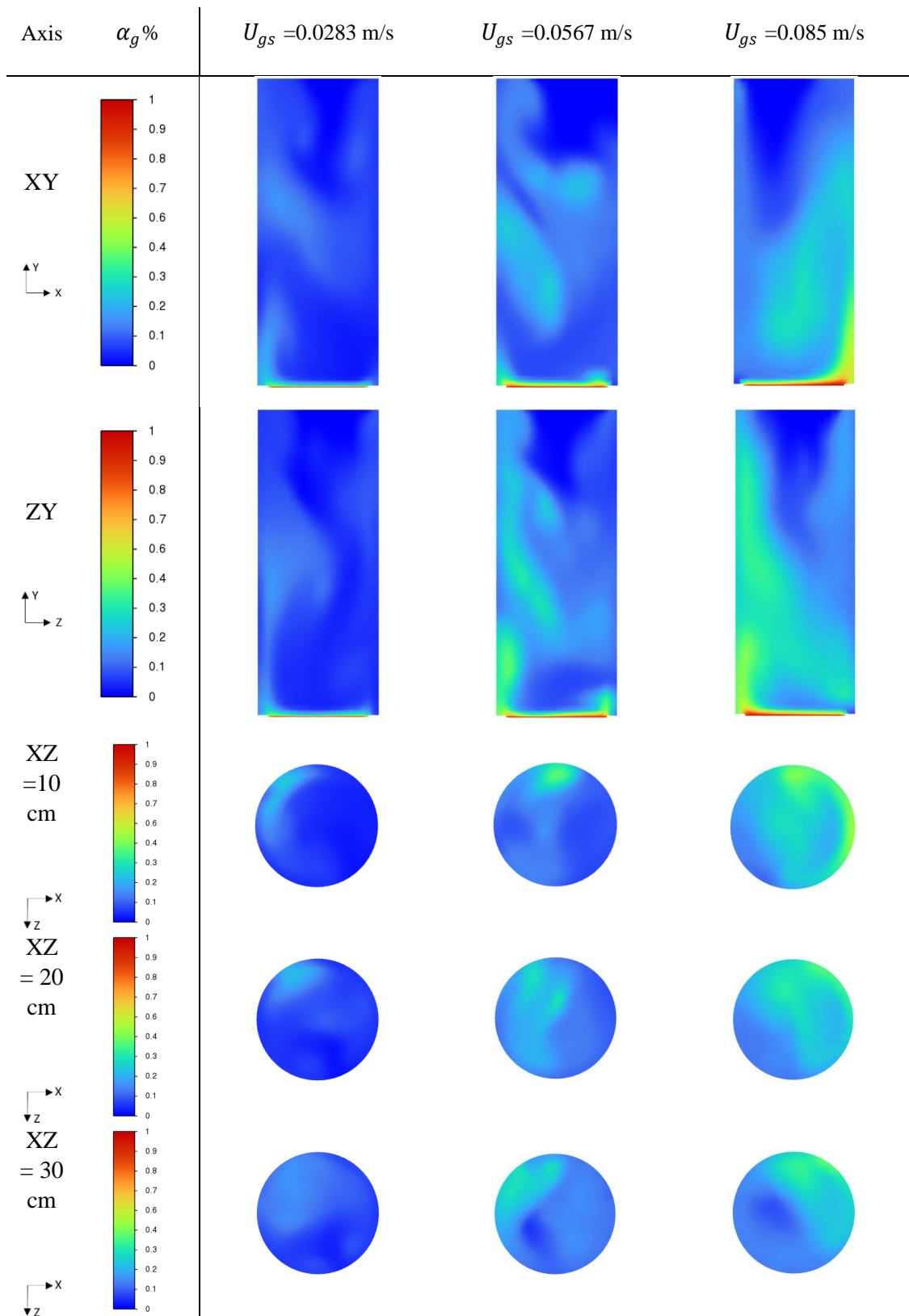


Figure. 4. 29 Oxygen-Cupreous Chloride Gas Holdup Contours for H=65cm, Cs=0%.

4.3.2. Effects of Static Liquid Height on Gas Holdup

Figure. 4.30 shows the three-dimensional curves of the gas holdup versus the H and U_{gs} for $C_s=0\%$. Figures. 4.31 depicts the effects of varying the H on the gas holdup while varying the U_{gs} for $C_s=0\%$ for an O₂-CuCl system. Figures. 4.32 -4.34 show the contours of the cut sections of the SBCR taken in the center of the XY, and ZY planes. Additional cut sections are taken at various heights on the ZX plane within the reactor at heights 10, 20 and 30 cm from the base of the reactor to allow for a more detailed contours of α_g . It is clear from the contours that the gas holdup is not symmetrical on the XY, ZY and the ZX planes demonstrating that the behavior of the gas holdup is strongly three dimensional. It is observed that as the H increases the α_g decreases. For $C_s=0\%$ at a superficial gas velocity of 0.085m/s it was observed that the gas holdup decreased by 20% when increasing H from 45cm to 65cm.

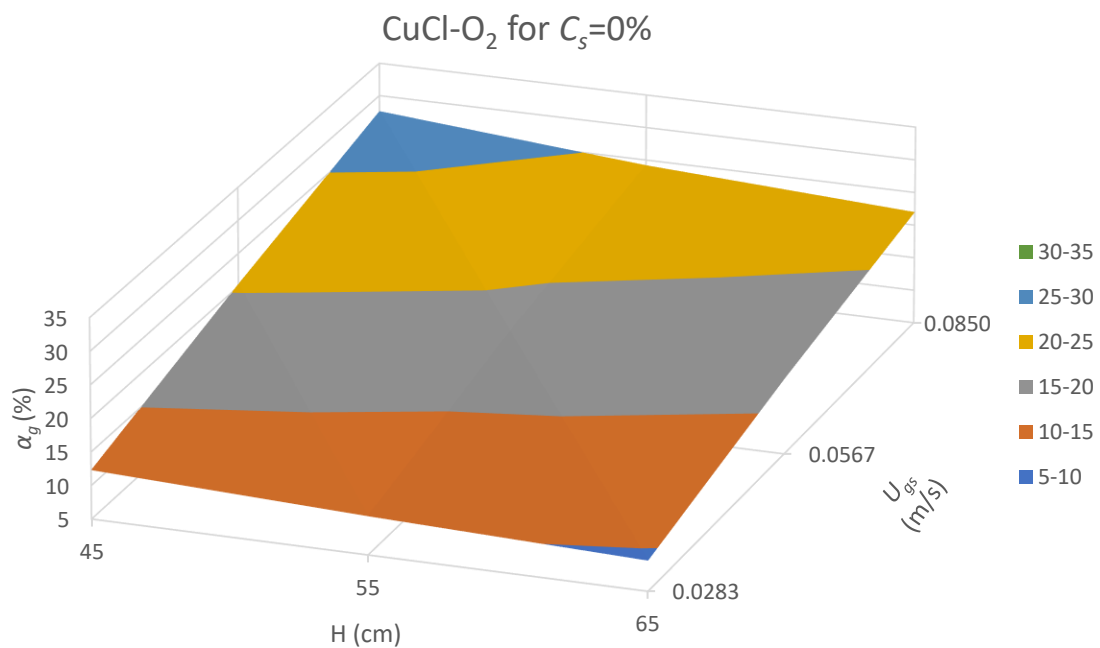


Figure. 4. 30 Average Gas Holdup (α_g) Versus Superficial Gas Velocity Static Liquid Height of CuCl-O₂ for $C_s=0\%$.

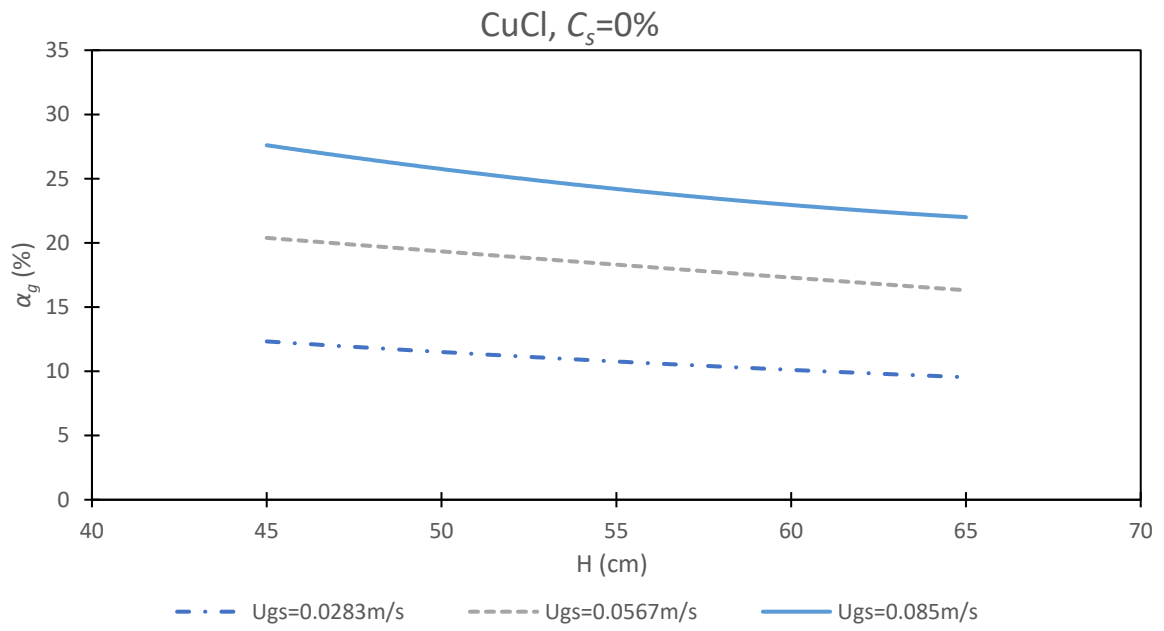


Figure. 4. 31 Average Gas Holdup Versus Static Liquid Height (H) of CuCl-O2 at Different Superficial Gas Velocities (U_{gs}) at $C_s=0\%$.

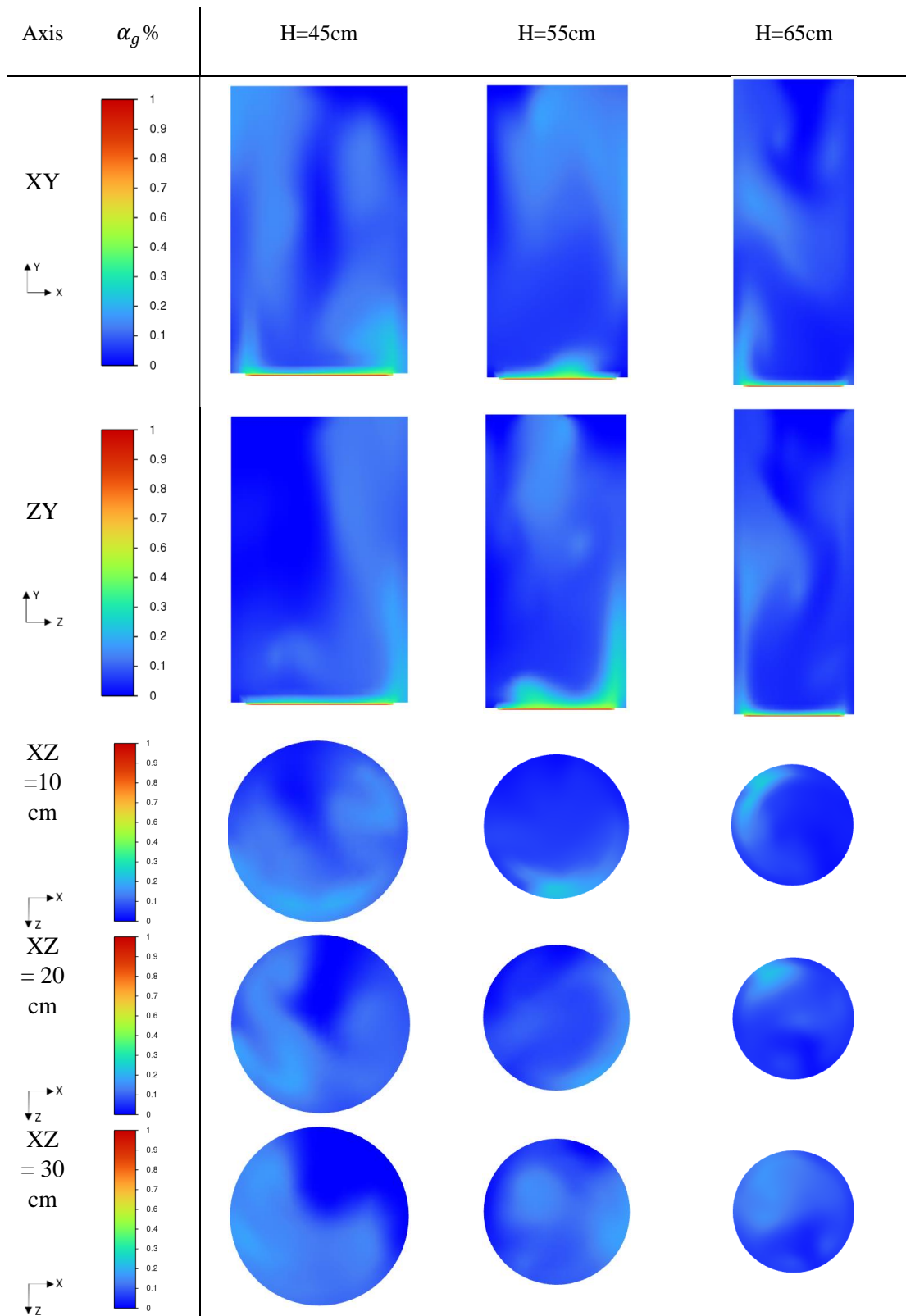


Figure. 4. 32 Oxygen-Cupreous Chloride Gas Holdup Contours for $U_{gs} = 0.0283$ m/s.

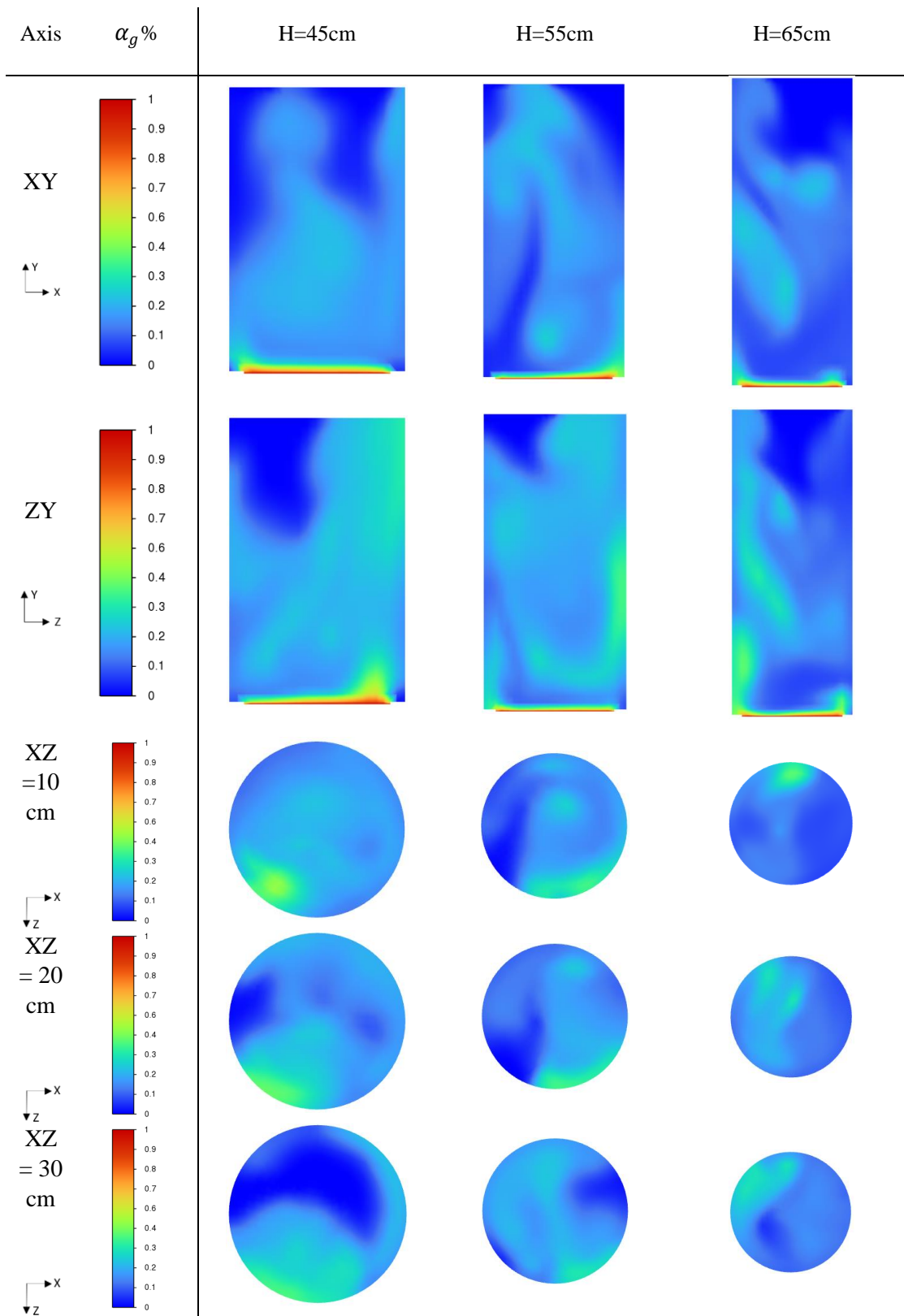


Figure. 4. 33 Oxygen-Cupreous Chloride Gas Holdup Contours for $U_{gs} = 0.0567$ m/s.

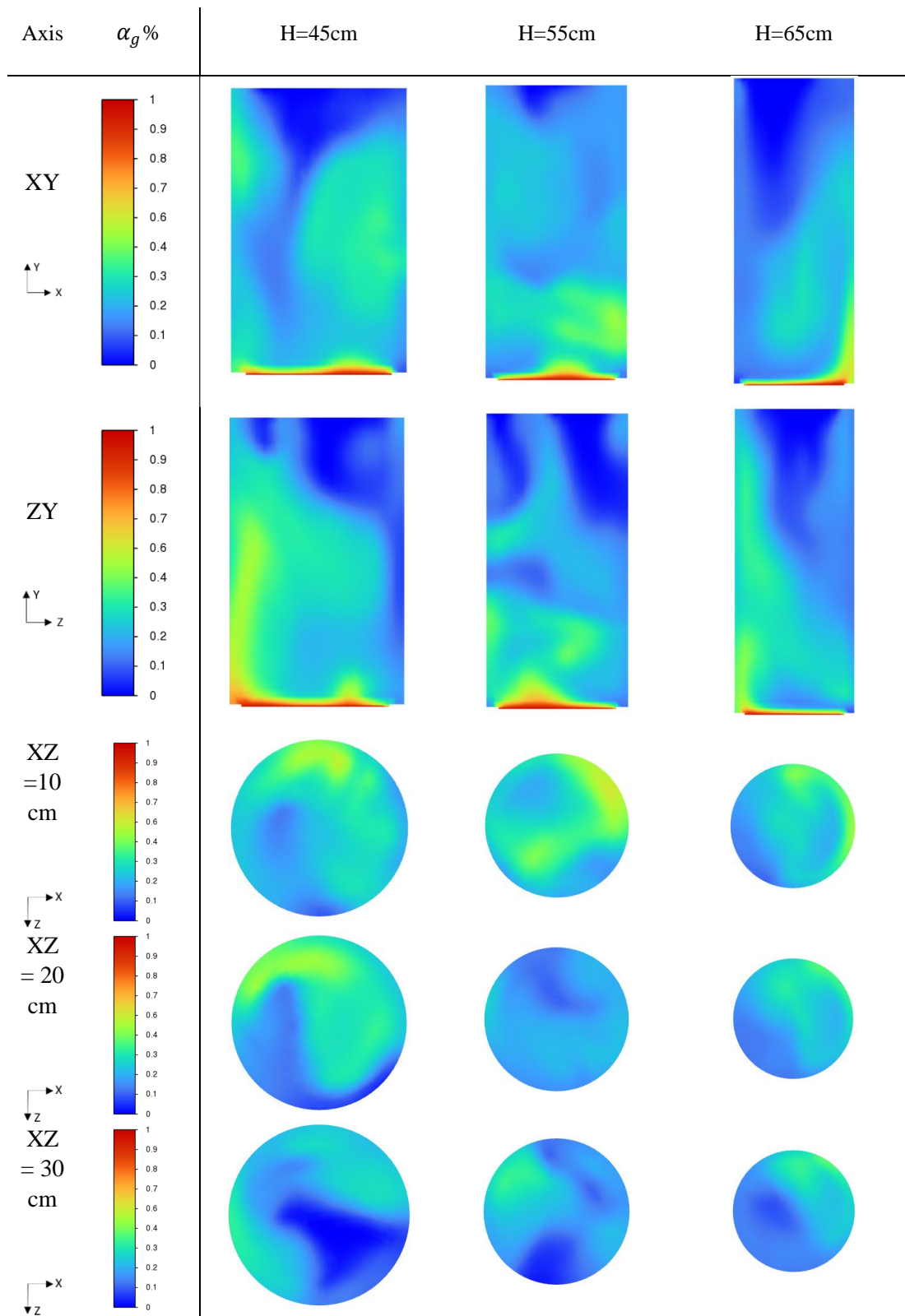


Figure. 4. 34 Oxygen-Cupreous Chloride Gas Holdup Contours for $U_{gs} = 0.085$ m/s.

4.3.3. Comparison of the 3D Water -Helium CFD system and the 3D Couperus Chloride-Oxygen CFD system

Figure. 4.35, Figure. 4.36 and Figure. 4.37 show the comparisons of the 3D-CFD simulations between Helium-Water (He-H₂O) and Oxygen-Couperus Chloride (O₂-CuCl) systems. A large percent error was noticed between the H₂O- He system and the CuCl-O₂ system with a percent error reaching up to 48.6% (Figure. 4.40) in which the CuCl-O₂ system gas holdup was underpredicted compared to that of helium-water system. The high percent error can be explained by the accumulation of percent errors from each of the hydrodynamic parameters as presented in Figure. 4.35 extracted from Abdulrahman's [4] study, and also due to the complexity of the multiphase system in 3D. The 3D CuCl-O₂ simulation was able to successfully simulate the trends and behavior within the SBCR.

Dimensionless Group	Actual Material	Experimental Materials	Error%
$\frac{\rho_g}{\rho_l}$	0.000121	0.000135	11.311
$\frac{\mu_g}{\mu_l}$	0.021756	0.023	6.908
$\frac{Re_l^2}{We_l}$	76473868 ($D_R=1m$)	76085070 ($D_R=1m$)	0.508

Figure. 4. 35 Dimensionless groups of actual and experimental material percent error [4].

Water-Helium		Cuprous Chloride-Oxygen		Percent Error
U_{gs} (m/s)	α_g (%)	U_{gs} (m/s)	α_g (%)	(%)
H=45 cm				
0.05	16.0	0.0283	12.3	29.9
0.1	24.4	0.0576	20.4	19.6

0.15	31.3	0.085	27.6	13.3
H=55 cm				
0.05	15.0	0.0283	10.8	39.4
0.1	22.7	0.0576	18.3	24.0
0.15	28.0	0.085	24.2	15.7
H=65 cm				
0.05	14.2	0.0283	9.5	48.6
0.1	21.7	0.0576	16.3	33.1
0.15	26.5	0.085	22.0	20.5

Figure. 4. 36 Comparison between the Water-Helium system and Cupreous Chloride- Oxygen superficial velocity and gas holdup with the calculated percent error.

From Figure. 4.37 and 4.38, it can be noticed that the behavior of the gas holdup with the superficial gas velocity and static liquid height is similar in both systems of H₂-H₂O and O₂-CuCl, where the gas holdup increases with increasing the superficial gas velocity and decreases with increasing the static liquid height. At lower velocities the gas holdup values were more closely clustered at different static liquid heights. However, as the superficial gas velocity increased the gas holdup values were more separated at different heights.

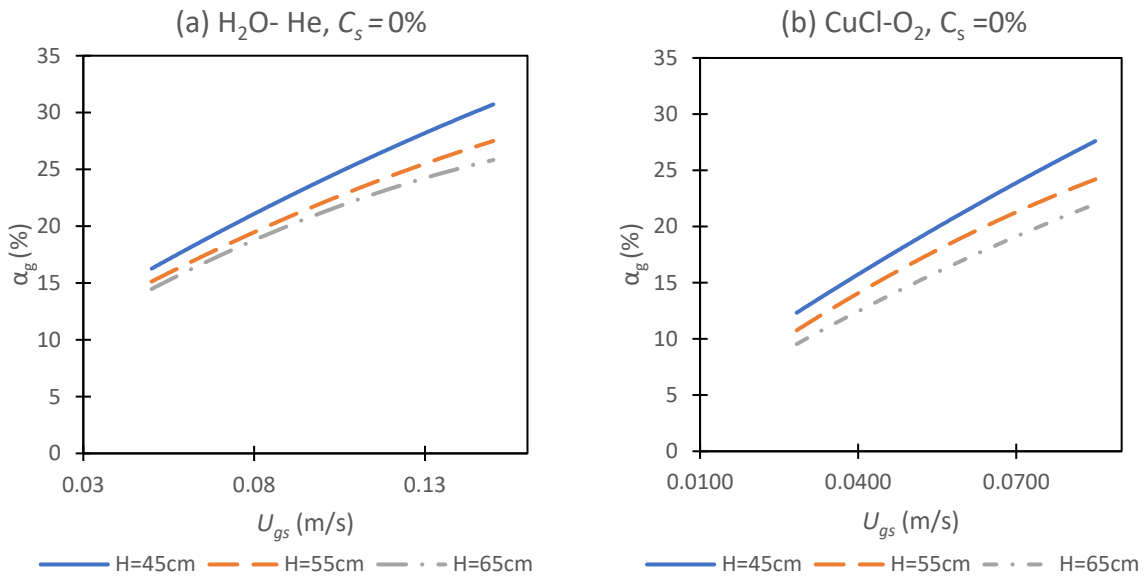


Figure. 4. 37 Comparison between the effects of static liquid heights on gas holdup versus different superficial gas velocities (a) Water-Helium data, (b) Cupreous chloride-oxygen data.

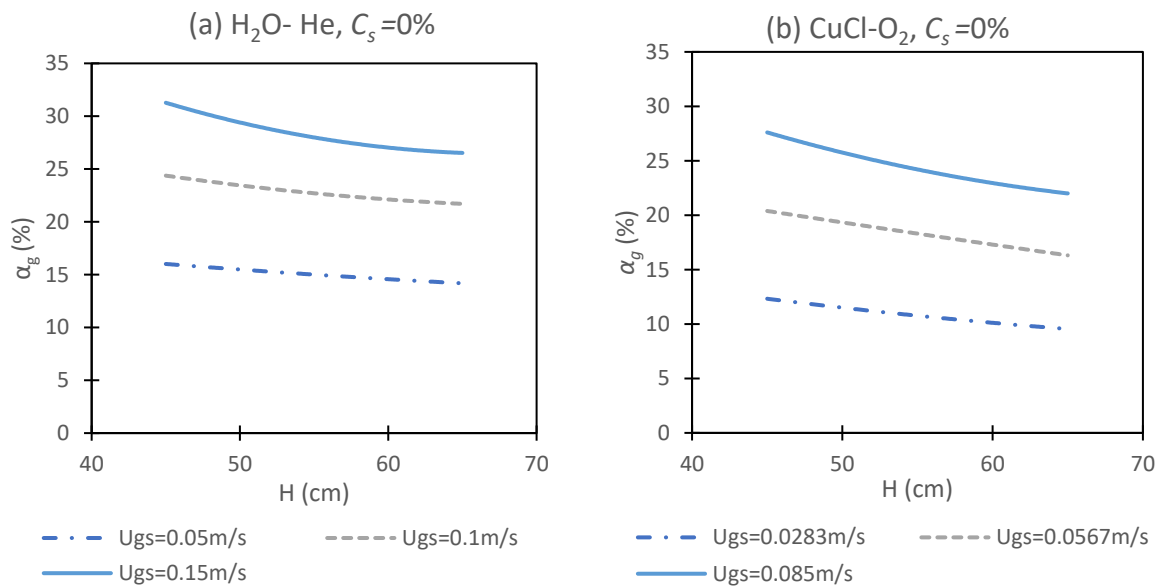


Figure. 4. 38 Comparison of Average Gas Holdup Versus Static Liquid Height for (a) Water-Helium system $C_s=0\%$ (b) Cupreous Chloride-Oxygen system $C_s=0\%$.

Chapter 5

Conclusion and Future Works

5.1 Conclusion

The objective of this thesis is to study the hydrodynamics of a direct contact heat transfer slurry bubble column reactor between Oxygen and molten Cupreous chloride. ANSYS Fluent software is utilized to conduct 3D-CFD simulations to validate the model for a Water- Helium-Alumina system at different superficial velocities, static liquid heights, and solid particle concentrations and study their effects on the gas holdup. The factors affecting the gas holdup are observed and the trends are recorded. It was observed that at most the percent error for the gas holdup between the 3D model and experimental data was 8.37% for a solid particle concentration of 10%. However, for lower solid particle concentrations such as 5% and 0% the percent error was lower with percent errors of 6.35% and 5.36% respectively. Furthermore, the model is used to simulate the hydrodynamics trends for a Cupreous Chloride – Oxygen system at different superficial gas velocities and static liquid heights. The Cupreous Chloride-Oxygen system's simulated results are compared to the simulated results of the Water-Helium system and the percent error was found to be at most 48.6% which is acceptable due to the complexity of the simulation and the accumulation of the percent errors from each of the hydrodynamic parameters.

The results from this thesis are intended to aid in the design and scale up of the oxygen production reactor in the thermochemical Cu-Cl cycle of hydrogen production using direct contact heat transfer method in a slurry bubble column reactor. Several key takeaways can

be concluded from the CFD simulations conducted for the Water- Helium-Alumina system and the Cupreous Chloride-Oxygen system, The conclusions include:

- 1) Gas holdup flow patterns in a 3D, CFD simulation, within a SBCR are non-symmetrical.
- 2) Gas holdup increases with increasing superficial gas velocities for different solid concentrations due to a larger number of bubbles being formed with increased gas velocity and due to a pressure drop in the bed of the reactor. The higher the gas flow rate the lower the hydrostatic pressure which decreases the bed pressure and increases the gas holdup. This was seen for the Helium-Water- Alumina system with a $C_s=0\%$ and $H=45\text{cm}$ when increasing the superficial gas velocity from 0.05m/s to 0.15m/s the gas holdup increased by 95%.
- 3) Gas holdup increases as the static liquid height decreases for different solid concentrations. This is due to the increase in hydrostatic pressure and pressure drop when the height of the reactor increases for certain superficial gas velocities. It was observed for the Helium-Water- Alumina system with a $C_s=0\%$ and a superficial gas velocity of 0.05m/s that increasing the H from 45cm to 65cm leads to a decrease in the gas holdup of 11%.
- 4) Gas holdup increases by decreasing the solid particle concentration for different static liquid heights. This occurs because increasing the solid particle concentration increases the slurry viscosity. The increased viscosity leads to large gas bubbles being formed and reduces bubbles breakage rates. The large bubbles will lower the gas holdup as they have a high-rise velocity. This was observed in the Helium-Water-Alumina system for $H=45\text{cm}$ and a superficial gas velocity of 0.05m/s when increasing the C_s from 0% to 10% the gas holdup decreased by 6%.
- 5) For the 3D-CFD results of Helium-Water-Alumina system, gas holdup is somewhat overpredicted the experimental results, opposed to 2D simulations which were underpredicted the experimental results.

- 6) The 3D simulations of the Helium-Water-Alumina system are more accurate than that of 2D-CFD simulations. The 3D simulation had a maximum percent error of 8.37% while the 2D simulations had at most a percent error of 28.5%.
- 7) The simulated 3D gas holdup results for lower solid particle concentrations in the water-helium-alumina system had lower percent errors.
- 8) The 3D simulated model of the Cupreous Chloride – Oxygen system was able to depict the hydrodynamic trends and behaviors which matched the hydrodynamic trends and behaviors of the Water- Helium system.
- 9) The 3D-CFD simulations are used to predict the gas holdup for Oxygen- Cupreous Chloride system and the results are compared to that of Helium-Water system. It is concluded that the 3D-CFD simulations could predict approximately the same percentage of error that was found from previous studies of material simulations that simulated the actual materials of the oxygen production reactor (Oxygen gas and Cupreous Chloride liquid) to Helium gas and Water liquid.
- 10) For both He-H₂O and O₂-CuCl systems, the gas holdup is more closely clustered at lower superficial gas velocities. As the superficial gas velocity increased the gas holdup values are more separated for both systems.

5.2 Recommendations for Future Research

This thesis presented valuable information in regards to the hydrodynamics of SBCR using water-helium-alumina and Cupreous chloride-oxygen. Further research can be conducted to advance the knowledge in this field. Recommendations for further research includes:

- Investigating the CFD simulation using the transient state to better understand the hydrodynamics of the system. This study was conducted using a steady state.

- Investigate the effects of different solid particle concentrations for Cupreous oxychloride within the Cupreous chloride-oxygen system.
- Creating a three-phase analysis of the CFD simulations for both the water-helium-alumina system and the cupreous chloride-oxygen-cupreous oxychloride systems to gain better insight into the hydrodynamics of the system and to reduce the percent error.
- Conducting experiments with the Cupreous chloride- oxygen- cupreous oxychloride at different superficial velocities, static liquid heights, and concentrations. Future CFD models can then be validated using the experimental data.
- Study in details the effects of different turbulence models on the CFD results.

References

1. Forsberg, Charles W. "Future Hydrogen Markets for Large-Scale Hydrogen Production Systems." *International Journal of Hydrogen Energy*, vol. 32, no. 4, 2007, pp. 431–439.
2. Lewis, Michele A., Manuela Serban, and John K. Basco. "Hydrogen production at 550 °C using a low temperature thermochemical cycle." *Proc. Nuclear Production of Hydrogen: Second Information Exchange Meeting*. 2003.
3. Serban, Manuela, Michele A. Lewis, and John K. Basco. *Kinetic study of the hydrogen and oxygen production reactions in the copper-chloride thermochemical cycle*. American Institute of Chemical Engineers, 2004.
4. Abdulrahman, Mohammed W. *Analysis of the thermal hydraulics of a multiphase oxygenproduction reactor in the Cu-Cl cycle*. Diss. University of Ontario Institute of Technology (Canada), 2016.
5. Ryskamp, John M., et al. *Design Features and Technology Uncertainties for the Next Generation Nuclear Plant*. No. INEEL/EXT-04-01816. Idaho National Lab.(INL), Idaho Falls, ID (United States), 2004.
6. Abdulrahman, Mohammed W. "Similitude for Thermal Scale-up of a Multiphase Thermolysis Reactor in the Cu-Cl Cycle of a Hydrogen Production." *International Journal of Energy and Power Engineering*, vol. 10.5, 2016, pp. 664-670.
7. Abdulrahman, Mohammed W. "Heat Transfer Analysis of a Multiphase Oxygen Reactor Heated by a Helical Tube in the Cu-Cl Cycle of a Hydrogen Production." *International Journal of Mechanical and Mechatronics Engineering*, vol. 10.6, 2016, pp. 1122-1127.
8. Abdulrahman, M. W., Wang, Z., Naterer, G. F., & Agelin-Chaab, M.

- “Thermohydraulics of a thermolysis reactor and heat exchangers in the Cu-Cl cycle of nuclear hydrogen production.” in *Proceedings of the 5th World Hydrogen Technologies Convention*, 2013.
9. Abdulrahman, Mohammed W. "Heat Transfer Analysis of the Spiral Baffled Jacketed Multiphase Oxygen Reactor in the Hydrogen Production Cu-Cl Cycle." In *Proceedings of the 9th International Conference on Fluid Flow, Heat and Mass Transfer (FFHMT'22)*, 2022.
 10. Abdulrahman, Mohammed W. "Review of the Thermal Hydraulics of Multi-Phase Oxygen Production Reactor in the Cu-Cl Cycle of Hydrogen Production." In *Proceedings of the 9th International Conference on Fluid Flow, Heat and Mass Transfer (FFHMT'22)*, 2022.
 11. Shaikh, Ashfaq. *Bubble and slurry bubble column reactors: mixing, flow regime transition and scaleup*. Vol. 68. No. 09. 2007.
 12. Nigam, Krishna D. P. *Three-Phase Sparged Reactors*. Edited by Adrian Schumpe, Taylor & Francis, 1996.
 13. Fan, L.-S., et al. “Some Aspects of High-Pressure Phenomena of Bubbles in Liquids and Liquid–Solid Suspensions.” *Chemical Engineering Science*, vol. 54, no. 21, 1999, pp. 4681–4709.
 14. Deckwer, W.-D., and A. Schumpe. “Improved Tools for Bubble Column Reactor Design and Scale-Up.” *Chemical Engineering Science*, vol. 48, no. 5, 1993, pp. 889–911.
 15. Lin, Tsao-Jen, and Shih-Ping Wang. “Effects of Macroscopic Hydrodynamics on Heat Transfer in Bubble Columns.” *Chemical Engineering Science*, vol. 56, no. 3, 2001, pp. 1143–1149.

16. Ravi, M.R.” Application of Computational Fluid Dynamics to Thermal Power Plants.” *Department of Mechanical Engineering, IIT Delhi*.
17. Abdulrahman, Mohammed W., and Nibras Nassar. "Eulerian Approach to CFD Analysis of a Bubble Column Reactor–A." In *Proceedings of the 8th World Congress on Mechanical, Chemical, and Material Engineering (MCM'22)*, 2022.
18. Litwin, Robert Z., and Stanley M. Pinkowski. "Solar power for thermochemical production of hydrogen." U.S. Patent No. 7,726,127. 1 Jun. 2010.
19. Marin, G.D., et al. “Byproducts and Reaction Pathways for Integration of the Cu–Cl Cycle of Hydrogen Production.” *International Journal of Hydrogen Energy*, vol. 36, no. 21, 2011, pp. 13414–13424.
20. Marin, Gabriel D. *Kinetics and transport phenomena in the chemical decomposition of copper oxychloride in the thermochemical Cu-Cl Cycle*. Diss. 2012.
21. Li, Le, et al. “CFD-PBM Investigation of the Hydrodynamics in a Slurry Bubble Column Reactor with a Circular Gas Distributor and Heat Exchanger Tube.” *Chemical Engineering Science: X*, vol. 9, 2021, p. 100087.
22. Matiazzo, T., et al. “Investigation of Breakup and Coalescence Models for Churn-Turbulent Gas-Liquid Bubble Columns.” *Journal of Applied Fluid Mechanics*, vol. 13, no. 2, 2020, pp. 737–751.
23. Ertekin, Ege, et al. “Validation Studies to Assist in the Development of Scale and System Independent CFD Models for Industrial Bubble Columns.” *Chemical Engineering Research and Design*, vol. 171, 2021, pp. 1–12.
24. Fletcher, David F., et al. “CFD Simulation of Industrial Bubble Columns: Numerical Challenges and Model Validation Successes.” *Applied Mathematical Modelling*, vol. 44, 2017, pp. 25–42.

25. Yan, Peng, et al. "CFD Simulation of Hydrodynamics in a High-Pressure Bubble Column Using Three Optimized Drag Models of Bubble Swarm." *Chemical Engineering Science*, vol. 199, 2019, pp. 137–155.
26. Sarhan, A.R., et al. "CFD Modeling of Bubble Column: Influence of Physico-Chemical Properties of the Gas/Liquid Phases Properties on Bubble Formation." *Separation and Purification Technology*, vol. 201, 2018, pp. 130–138.
27. Abdulrahman, M. W. "Experimental studies of gas holdup in a slurry bubble column at high gas temperature of a helium– water– alumina system." *Chemical Engineering Research and Design* vol. 109, 2016, pp. 486-494.
28. Abdulrahman, M. W. "Experimental studies of the transition velocity in a slurry bubble column at high gas temperature of a helium–water–alumina system." *Experimental Thermal and Fluid Science*, vol. 74, 2016, pp. 404-410.
29. Abdulrahman, M. W. "Experimental studies of direct contact heat transfer in a slurry bubble column at high gas temperature of a helium–water–alumina system." *Applied Thermal Engineering*, vol. 91, 2015, pp. 515-524.
30. Abdulrahman, Mohammed Wassef. "Direct contact heat transfer in the thermolysis reactor of hydrogen production Cu—Cl cycle." U.S. Patent No. 10,059,586. 28 Aug. 2018.
31. Adam, Salman, and Kalthoum Tuwaechi. "Hydraulic Simulation of Bubble Flow in Bubble Column Reactor." *Journal of Complex Flow* vol.1, no.2, Dec. 2019.
32. Li, Zhaoqi, et al. "Experimental and Numerical Investigations of Scale-up Effects on the Hydrodynamics of Slurry Bubble Columns." *Chinese Journal of Chemical Engineering*, vol. 24, no. 8, 2016, pp. 963–971.

33. Pourtousi, M., et al. "Effect of Bubble Diameter Size on Prediction of Flow Pattern in Euler–Euler Simulation of Homogeneous Bubble Column Regime." *Measurement*, vol. 76, 2015, pp. 255–270.
34. Li, Weiling, and Wenqi Zhong. "CFD Simulation of Hydrodynamics of Gas–Liquid–Solid Three-Phase Bubble Column." *Powder Technology*, vol. 286, 2015, pp. 766–788.
35. Abdulrahman, Mohammed W. "Effect of Solid Particles on Gas Holdup in a Slurry Bubble Column." In *Proceedings of the 6th World Congress on Mechanical, Chemical, and Material Engineering*, 2020.
36. Zhou, Rongtao, et al. "A Conceptual Model for Analyzing Particle Effects on Gas-Liquid Flows in Slurry Bubble Columns." *Powder Technology*, vol. 365, 2020, pp. 28–38.
37. Abdulrahman, Mohammed W. "CFD Simulations of Gas Holdup in a Bubble Column at High Gas Temperature of a Helium-Water System." In *Proceedings of the 7th World Congress on Mechanical, Chemical, and Material Engineering (MCM'20)*, 2020
38. Chen, Jiaqi, and Caleb S. Brooks. "Experiments and CFD Simulation of Mass Transfer and Hydrodynamics in a Cylindrical Bubble Column." *Chemical Engineering Science*, vol. 234, 2021, p. 116435.
39. Sarhan, A.R., et al. "CFD Model Simulation of Bubble Surface Area Flux in Flotation Column Reactor in Presence of Minerals." *International Journal of Mining Science and Technology*, vol. 28, no. 6, 2018, pp. 999–1007.
40. Wodołażski, Artur. "CFD Hydrodynamics Analysis of Syngas Flow in Slurry Bubble Column." *Journal of Oil, Gas and Petrochemical Technology*, vol. 3, no.1, 2016, pp. 83-96.

41. Abdulrahman, Mohammed W. "CFD Analysis of Temperature Distributions in a Slurry Bubble Column with Direct Contact Heat Transfer." In *Proceedings of the 3rd International Conference on Fluid Flow, Heat and Mass Transfer (FFHMT'16)*. 2016.
42. Abdulrahman, Mohammed W. "Temperature profiles of a direct contact heat transfer in a slurry bubble column." *Chemical Engineering Research and Design*, vol. 182, 2022, pp. 183-193.
43. Abdulrahman, M.W. "CFD Simulations of Direct Contact Volumetric Heat Transfer Coefficient in a Slurry Bubble Column at a High Gas Temperature of a Helium–Water–Alumina System." *Applied Thermal Engineering*, vol. 99, 2016, pp. 224–234.
44. Pu, Wenhao, et al. "Simulation on Direct Contact Heat Transfer in Gas-Molten Salt Bubble Column for High Temperature Solar Thermal Storage." *International Communications in Heat and Mass Transfer*, vol. 104, 2019, pp. 51–59.
45. Zhang, Xi-Bao, and Zheng-Hong Luo. "Local Gas–Liquid Slip Velocity Distribution in Bubble Columns and Its Relationship with Heat Transfer." *AIChE Journal*, vol. 67, no. 1, 2020.
46. Geng, Shujun, et al. "Process Intensification in Pneumatically Agitated Slurry Reactors." *Engineering*, vol. 7, no. 3, 2021, pp. 304–325.
47. Suzzi, Daniele, et al. "Validation of Euler-Euler and Euler-Lagrange Approaches in the Simulation of Bubble Columns." *Chemical Engineering Transactions*, vol. 17, 2009, pp. 585-590.
48. ANSYS Inc. "ANSYS FLUENT Theory Guide." ANSYS FLUENT Theory Guide, Version 14.5, 2012.
49. Abdulrahman, Mohammed Wassef. "Material substitution of cuprous chloride molten salt and oxygen gas in the thermolysis reactor of hydrogen production Cu—Cl cycle." U.S. Patent No. 10,526,201. 7 Jan. 2020.

50. Abdulrahman, Mohammed W. "Simulation of Materials Used in the Multiphase Oxygen Reactor of Hydrogen Production Cu-Cl Cycle." *Proceedings of the 6th International Conference of Fluid Flow, Heat and Mass Transfer (FFHMT'19)*. 2019.
51. Sokolichin, A., et al. "Simulation of Buoyancy Driven Bubbly Flow: Established Simplifications and Open Questions." *AIChE Journal*, vol. 50, no. 1, 2004, pp. 24–45.
52. Lemmon, E. W., and R. T Jacobsen. "Viscosity and Thermal Conductivity Equations for Nitrogen, Oxygen, Argon, and Air." *International Journal of Thermophysics*, vol. 25, no. 1, 2004, pp. 21–69.
53. Borgnakke, Claus, and Richard E. Sonntag. "Fundamentals of thermodynamics: Part 1." 2009.
54. Petersen, Helge. *The properties of helium: density, specific heats, viscosity, and thermal conductivity at pressures from 1 to 100 bar and from room temperature to about 1800 K*. Copenhagen: Jul. Gjellerup, 1970.
55. Zamfirescu, C., et al. "Thermophysical Properties of Copper Compounds in Copper–Chlorine Thermochemical Water Splitting Cycles." *International Journal of Hydrogen Energy*, vol. 35, no. 10, 2010, pp. 4839–4852.
56. Auerkari, Pertti. *Mechanical and physical properties of engineering alumina ceramics*. Vol. 23. Espoo: Technical Research Centre of Finland, 1996.
57. Boomsma, K., and D. Poulikakos. "On the Effective Thermal Conductivity of a Three-Dimensionally Structured Fluid-Saturated Metal Foam." *International Journal of Heat and Mass Transfer*, vol. 44, no. 4, 2001, pp. 827–836.
58. Guth, E., and H. Simha. 'Viscosity of Suspensions and Solutions: III Viscosity of Sphere Suspensions'. *Kolloid-Z*, vol. 74, 1936, pp. 266–275.
59. Sokolichin, A., and G. Eigenberger. "Applicability of the Standard $k-\epsilon$ Turbulence Model to the Dynamic Simulation of Bubble Columns: Part I. Detailed Numerical

Simulations.” *Chemical Engineering Science*, vol. 54, no. 13-14, 1999, pp. 2273–2284.

60. Behkish, Arsam. *Hydrodynamic and mass transfer parameters in large-scale slurry bubble column reactors*. Diss. University of Pittsburgh, 2005.
61. Krishna, R., and S.T. Sie. “Design and Scale-up of the Fischer–Tropsch Bubble Column Slurry Reactor.” *Fuel Processing Technology*, vol. 64, no. 1-3, 2000, pp. 73–105.